FUNCTIONALIZATION OF STABLE METAL–ORGANIC FRAMEWORKS AND THEIR APPLICATIONS

A Dissertation

by

JIHYE PARK

Submitted to the Office of Graduate and Professional Studies of
Texas A&M University
in partial fulfillment of the requirements for the degree of

DOCTOR OF PHILOSOPHY

Chair of Committee,	Hongcai Zhou
Committee Members,	Perla B. Balbuena
	Christian B. Hilty
	Karen L. Wooley
Head of Department,	Simon W. North

August 2016

Major Subject: Chemistry

ABSTRACT

Metal–organic frameworks (MOFs) are newly emerging inorganic–organic hybrid porous materials with diverse crystalline structures, high surface areas, and tunable pores. This dissertation primarily focuses on design and synthesis of MOFs as well as the development of synthetic methodologies to target stable MOFs with desired functionalities.

In the second section, a linker exchange strategy was developed as a route to functionalize a mesoporous MOF, PCN-333, through thermodynamic control. This strategy allowed a facile incorporation of a variety of functional groups into the mesoporous MOF without compromising integrity of the parent MOF.

In the third section, a dual-exchange method was studied using a sequential linker exchange and metal metathesis on PCN-333(Fe) to achieve a chemically robust mesoporous Cr-MOF with desired functional group. Dual exchange showed the potential of this method to be a general approach to highly stable Cr-MOFs with desired functional groups upon selection of appropriate MOF template.

In the fourth section, a new Zn-MOF, SO-PCN, was designed and synthesized as a host of two dye linkers. SO-PCN showed energy transfer between the 2D porphyrinic photosensitizer layer and the photochromic switch pillar in the framework. Using photochromic reaction of the linker in SO-PCN, a reversible control of singlet oxygen generation was demonstrated. The catalytic activity of SO-PCN was also studied for photooxidation of 1,5-dihydroxynaphthalene.

In the fifth section, a new synthetic strategy to incorporate multiple functional molecules within the MOF nanoparticles was demonstrated for control of $^1O_2$ generation for PDT. This strategy was developed to improve several inherent limitations from SO-PCN in the previous section. First, a Zr-MOF nanoplatform showed much improved stability in aqueous media, compatible under physiological conditions. This strategy allows for tuning of the ratios between the photosensitizer and the switch molecule within the Zr-MOF nanoparticles, thus enabling maximization of the $^1O_2$ generation controllability. As a result, MOF nanoparticle formulation showed an enhanced PDT efficacy with superior $^1O_2$ control compared to that of homogeneous molecular analogues.

In the sixth section, size-controlled synthesis of Zr-based porphyrinic MOF nanoparticles was studied through a bottom-up approach. The study provided mechanistic insights about the size control of the porphyrinic Zr-MOF nanoparticles. Size-dependent cellular uptake and ensuing PDT efficacy were also investigated to optimize the size of the MOF nanoparticles for PDT. Additionally, folic acid modification on the Zr_6 node in the MOF showed further enhanced PDT efficacy via active targeting, demonstrating multifunctional MOF nanoplatform.

In summary, methodologies to allow functionalization of highly stable MOFs have been designed and studied. Conceptual utilizations of MOF nanoparticles for biomedical applications have also been demonstrated with stable MOF nanoparticles, showing the advantages of the MOF formulation. The findings in this dissertation provide design principle and possible options for preparing targeted MOFs as required in desired applications.

DEDICATION

To my parents and brother for their love and support

ACKNOWLEDGMENTS

I, first and foremost, would like to express my sincere gratitude to my advisor Dr. Joe Zhou for his patience, inspiration, and faith in me that I didn't even see in myself. His guidance just perfectly worked for me and pushed me to my full potential. I could not have imagined having a better advisor and mentor. I am very grateful to him for providing me with the best scientific and mental support. I have a wonderful committee as well which is very supportive of my research and academic career. I would like to thank Dr. Karen Wooley, Dr. Christian Hilty, and Dr. Perla Balbuena for their helpful comments and thoughtful input throughout the PhD program. My thanks also go to my colleagues, faculty, and staff in the chemistry department for making my time at Texas A&M a great experience! Special thanks go to Sandy Horton, Dr. Joanna Pellois, Dr. Simon North, Dr. Tamara Powers, and Carrie Frederiksen for their help keeping me on the right track during the course of the program.

I would also like to thank my undergraduate research advisor, Dr. Youngmi Kim, for enlightening me during my research experience. I realize my PhD research was largely inspired by questions I had in my undergraduate research. I am so grateful for the opportunity to work in her lab. Thanks also go to our external collaborators at Stockholm University, the Chinese Academy of Sciences, and Fudan University. Their expertise certainly improved the quality of my research. I would also like to extend my gratitude to the funding agencies supporting my PhD research including U.S. Department of Energy

(DE-SC0001015) and Welch Foundation (A-1725). The use of Texas A&M University Laboratory for Synthetic-Biologic Interactions is acknowledged.

I thank all the past and present Zhou group members for their willingness to help and their participation in inspiring discussions. Special thanks go to Dawei, Zac, Zhangwen, Madi, Kevin, Stephen, Mat, and Heather. I am particularly grateful to Dawei for helping me take big steps into the real MOF world. Without his help and our discussions, I could never be where I am now. I will miss all the joyous moments of our new discoveries! Also, Zac deserves a special acknowledgment. Zac has been my wonderful friend inside and outside of the group. I am so grateful for our friendship and for him taking me out from the lab for fun hangouts with Ashley, as well as feeding me well.

Outside lab, I am so much blessed to have amazing friends in College Station. They have made me never regret my decision to come to Texas for PhD study. First, I must thank Mary Harrell, my sister of the states! From day one in graduate school, we have been together going through all the hurdles. I was very fortunate to meet her as she understands me so well without needing a word. I am thankful to the Harrell family as well for their love and care. I will never forget the most surprising birthday party that I had in TN with Harrells. Also, I am very thankful to Simcha Felder, a thoughtful and loving friend. Simcha has never refused to help whenever I asked favors, advice, or encouragement. We three, Team Jihye, has successfully survived and they could never know how grateful I am for coloring my monotonous yellow Texas canvas vividly.

I also would like to thank my Korean friends. I thank the family of Hye Lim Han and Dr. Gyu Seong Heo for making my life in College Station so cared for and joyful. My classmates and the class a year below me, Shinhye, Yaewon, Jihyun, and Jongbok, definitely deserve thanks. They are such nice people with warm hearts and helped me a lot along the way. Also, I thank my old friends in Korea or other places whom I cannot even dare try to list here because there are just too many. I will be forever thankful for our friendship! My time in College Station was also enriched by the friendship of my Starbucks barista friends, which have never been expected from getting the daily dose of caffeine (1.16 mmol). Without their constant caffeine support, I would not have been able to make this journey in four years.

Last but not least, my parents, brother, and grandmother deserve the greatest thanks for their unconditional love, endless patience, and constant encouragement for me. My parents have always been very supportive of my decision and have never wanted me to settle. I heartily love my mom, Hyang-Sook Song, my best friend whom I am forever in debt to, and my dad, Seung-Ho Park, who loves his daughter more than anyone else. Also, I have been so much cared by my aunts and uncles since I was young, especially by Hyangsun Song. I am very happy to have such close relatives and am thankful for their love and support as well.

I am truly a lucky person to make this acknowledgment and I will keep moving forward to repay the love and support I have received as much as possible.

NOMENCLATURE

2D	two-dimensional
3D	three-dimensional
BET	Brunauer-Emmett-Teller
DEF	*N*,*N*-Diethyl Formamide
DMF	*N*,*N*-Dimethyl Formamide
DMSO	Dimethyl Sulfoxide
EDS	Energy-dispersive X-ray Spectroscopy
FW	Formula Weight
MOF	Metal–Organic Framework
NMR	Nuclear Magnetic Resonance
PCN	Porous Coordination Network
PDT	Photodynamic Therapy
PSM	Postsynthetic Modification
PXRD	Powder X-Ray Diffraction
SEM	Scanning Electron Microscopy
TEM	Transmission Electron Microscopy
TGA	Thermogravimetric Analysis
XPS	X-ray Photoelectron Spectroscopy

TABLE OF CONTENTS

Page

LIST OF FIGURES

Page

Page

Page

Page

LIST OF TABLES

1. INTRODUCTION

As a new class of inorganic–organic hybrid materials, metal–organic frameworks (MOFs) have been rigorously explored as advanced porous materials.[1] The limitless combination of organic and inorganic building blocks in MOFs allow diverse 3D crystalline structures with high internal surface area and well-defined molecular level of functionality with remarkable accessibility, thus making MOFs viable for various applications, which might have not been readily achievable from other conventional porous materials, including activated carbons, mesoporous silica, and zeolites.[2-4] With these features, recently MOFs have become a useful tool for deciphering fundamental questions in chemistry, including a mechanistic study of a controversial intermediate with crystallographic analysis, a well-defined energy transfer platform, and gas storage and separation.[5-7]

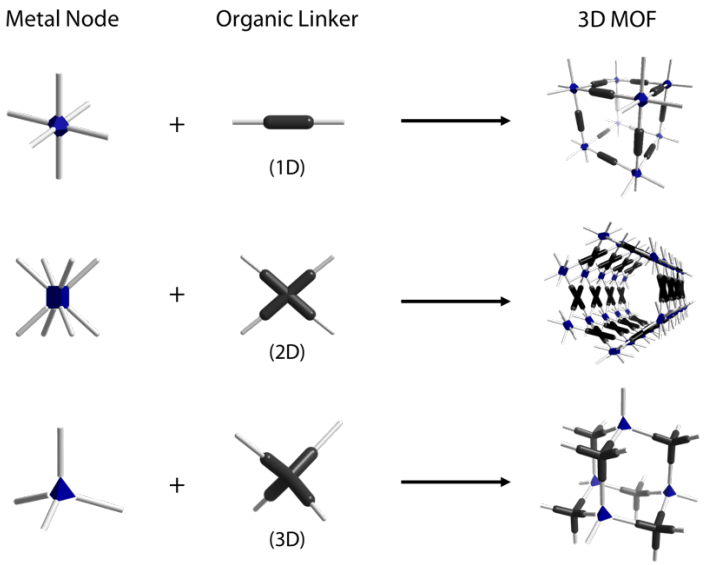

Figure 1.1 Topological illustration of representative 3D MOFs.

Unlike other conventional porous materials constructed from extremely robust covalent bonds or ionic bonds, however, prototypical MOFs suffered from weak chemical stability due to the relatively labile coordination bond and void space in the framework. Particularly, in the early stage of MOF development, the combination of hard base, carboxylate containing linkers (L) and soft acid metal species [M(II); M = Zn, Cu] has been extensively adopted, which results in labile M-L bonds according to hard soft acid and base (HSAB) theory.[8,9] Consequently, most MOFs tend to undergo decomposition when applied in harsh chemical environments. Such instability has been the most challenging problem for early MOFs to be practically utilized. To maximize the utility of MOFs in various applications, therefore, their chemical stability has to be a prime consideration to guarantee their advantageous features to be fully utilized. To improve chemical stability of the MOFs, there are two major strategies commonly adopted: (1) using the combination of high valent metal species [e.g., Al(III), Fe(III), Cr(III), Zr(IV)] and carboxylate linkers, giving rise to robust M-L bonds from stronger electrostatic interaction; (2) a combination between soft acid metal species [e.g., Cu(II), Ni (II)] and soft base containing linkers, including imidazolate, pyrazolate, or thiolate, leading to stronger orbital interactions.[10,11] As a result of robust M-L bonds in the framework, these MOFs exhibit extraordinary stability against attacks from reactive chemical species.

Although the stability of MOFs was improved by involving robust M-L bonds, synthesizing these MOFs is very difficult because more stable M-L bonds are less reversible during the growth of MOFs, inhibiting crystallization.[12] Aside from such synthetic difficulty to get stable MOFs, when functionalization is concerned for specific

use, obtaining highly crystalline products of stable MOFs out of the functionalized linkers from direct synthesis becomes extremely challenging for the following reasons. First, the preinstalled functionality on the linker is likely to undergo decomposition or side reactions under the harsh synthetic conditions of stable MOFs (e.g., high temperature and acidic environment).[10] In addition, the functionalization prior to MOF synthesis could alter the molecular geometry of the linker, leading to undesired products. Therefore, development of synthetic strategies to obtain a stable MOF platform with both desired functionalities and wanted structure is of great importance in terms of exploring a broad applicability of MOFs.

Aside from the predesigned functions on the building blocks in the framework, the morphology and size of the MOFs could also play a critical role in many aspects of practical applications. In this regard, controllability of MOF nanoparticles can further lead to a fine-tuning of their properties with synthetic tunability to establish multiple functionalities into one platform. Therefore, the control of size and morphology of targeting MOFs is highly desired to optimize the performance of MOFs for target applications.[13]

While an extensive research effort has been made to discover new MOF structures, MOFs as a class of nanomaterials with such controllability have been significantly understudied, though the understanding of crystal growth could provide us insights to take the advantage of controllability of MOFs. Because MOF growth can be greatly simplified as traditional coordination chemistry using a ligand substitution process, studies of MOF growth could provide important insights about their controlled growth both in morphology

(phase selectivity) and size. Together with the findings in chemical stabilization and functionalization of stable MOFs, understanding of MOF nanocrystal growth control could thus prove a powerful tool for optimization of materials and further grant this class of materials to be promising in desired applications.

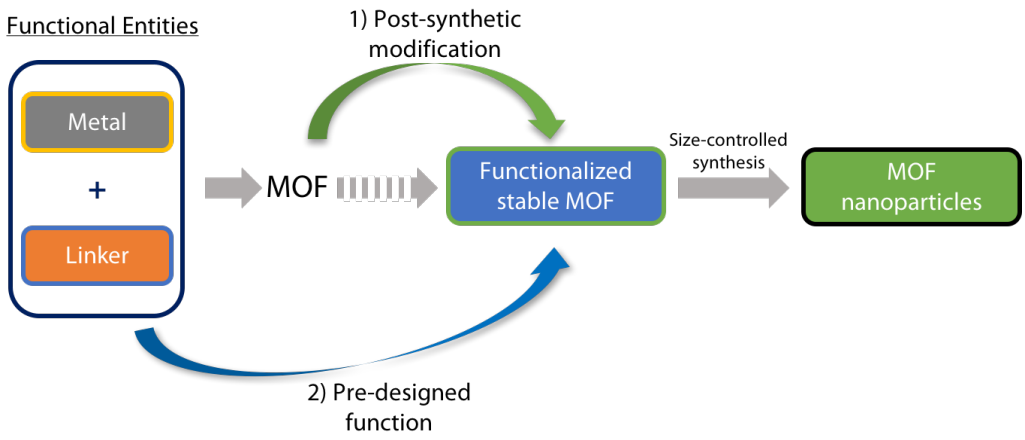

Figure 1.2 Routes to functionalized stable MOF nanoplatform.

In this dissertation, synthetic methodologies to tackle the challenges mentioned above in targeting specific MOFs have been developed. Starting from questioning MOF growth process, the understanding of MOF growth via thermodynamics and kinetics analysis in MOF systems is discussed. Two approaches to achieve highly stable MOFs with desired functionality were developed via postsynthetic dual exchange and *in situ* incorporation of multiple functionalities. Through combination of the presented synthetic strategies, fine-tuning of the MOF products, including their size, morphology, and tunable function-density of the multiple functional species in the MOF, has been realized. As a

result, judiciously designed MOFs were successfully demonstrated for biomedical applications (i.e., photodynamic therapy) where stability, functionality, and controllability allowed for screening of the best performing materials.

2. STRUCTURE-ASSISTED FUNCTIONAL ANCHOR IMPLANTATION IN ROBUST METAL–ORGANIC FRAMEWORKS WITH ULTRALARGE PORES*

2.1 Introduction

Ordered mesoporous materials have been extensively studied because of their potential toward practical applications including heterogeneous supports for catalysis, separation, enzyme immobilization, drug delivery, and sensing taking advantage of their high surface areas and large pores.[3,14-17] In particular, for large guest molecules such as organometallic species, nanoparticles, and enzymes the mesoporosity is of great importance.[18,19] Traditional mesoporous materials including mesoporous silica, mesoporous carbon, and metal oxides have paved the ways for such applications, but there are major limitations to these materials such as lack of structural diversity (e.g., pore geometry) and versatile functionality. Moreover, to effectively prevent leaching of the immobilized species, postsynthetic modification of functional groups to covalently anchor the guest species is highly desired. However, it has been challenging due to the lack of easily modifiable sites in these traditional mesoporous materials.[20-22]

In the last two decades, metal–organic frameworks (MOFs) have emerged as a class of promising organic–inorganic hybrid materials that are composed of metal ions/clusters and bridging organic linkers.[1] Due to their tunable structures derived from a judicious selection of inorganic building blocks and the molecular-level design of organic linkers, MOFs can provide tailor-made structures for desired applications compared with

---

*Reproduced with permission from Park, J.; Feng, D.; Zhou, H.-C., *J. Am. Chem. Soc.* **2015,** *137*, 1663–1672. Copyright 2015 American Chemical Society.

conventional mesoporous materials.[23-25] Apart from the structural diversity of MOFs, their three-dimensional (3D) cavities can facilitate the accessibility of the guest molecules. Therefore, mesoporous MOFs with predesigned covalent anchors (pendant functional groups) can serve as ideal platforms to immobilize functional species.

However, most MOF materials reported to date are mainly restricted to a microporous regime.[26-35] Even for mesoporous MOFs, the accommodation of large molecules into the pores such as bulky catalysts or enzymes is challenging because such large entities will take up a substantial volume of the pore.[10,36] As a result, efficient diffusion is slowed, and the accessibility of incoming species will be reduced substantially. In addition, introduction of covalent anchors could further reduce the original pore size, leaving even less space to immobilize large species. Most importantly, an excellent stability of the framework is a prerequisite to guarantee the framework intactness, especially with inclusion of immobilized guests working in harsh conditions. However, most reported mesoporous MOFs show relatively weak chemical stability.[37-39] Therefore, stable MOFs with ultralarge pores and functional groups are highly desired.

Herein we report a facile route to functionalize PCN-333(M) (M = Fe and Sc), a robust MOF isoreticular to MIL-100 with ultralarge pores (~5.5 nm), via postsynthetic ligand exchange that is assisted by structural integrity of PCN-333. A wide range of functional groups were introduced into the PCN-333(M) while maintaining the porosity and crystallinity of the parent framework. Furthermore, several experiments were performed to illustrate a better understanding of the ligand exchange process in PCN-333(Fe). Ultimately, introduction of a secondary functional group into functionalized

PCN-333 was successfully demonstrated through click chemistry. These findings will allow for functionalized PCN-333(M) to be used as a useful scaffold for a variety of promising applications by taking advantage of facile functionalization, framework robustness, and ultralarge pores which allow for more possible chemistry within the MOF.

2.2 Experimental section

Materials

All starting materials and solvents were used as received without further purification from commercial suppliers. (Alfa Aesar, Sigma-Aldrich, TCI America, Cambridge Isotope, Oakwood Products) Silica gel (40–42 μm) was purchased from Silicycle Inc. The abbreviation for some solvents and reagents were listed here: 1,2-Dimethoxyethane (DME), CH_2Cl_2 (DCM), *N*,*N*-dimethylformamide (DMF), *N*,*N*-diethylformamide (DEF), dimethylsulfoxide (DMSO), and tetrahydrofuran (THF).

Instrumentation

Synthetic manipulations that required an inert atmosphere (where noted) were carried out under nitrogen using standard Schlenk techniques. Nuclear magnetic resonance (NMR) spectra were recorded on Mercury 300 spectrometer and Varian Inova 500 spectrometer. The chemical shifts are given in units of δ (ppm) relative to tetramethylsilane (TMS) where δ (TMS) = 0, or referenced to the residual solvent resonances. Splitting patterns are denoted as s (singlet), d (doublet), t (triplet), q (quartet), m (multiplet), and br (broad). Powder X-ray diffraction (PXRD) was carried out on a Bruker D8-Focus Bragg-Brentano X-ray powder Diffractometer equipped with a Cu sealed tube (λ = 1.54178) at 40 kV and 40 mA. Thermogravimetric analyses (TGA) were

conducted on a Shimadzu TGA-50 thermogravimetric analyzer from room temperature to 600 °C at a ramp rate of 2 °C/min in a flowing nitrogen atmosphere. Fourier transform infrared (IR) measurements were performed on a Shimadzu IR Affinity-1 spectrometer. Fluorescence spectra were recorded on PTI QuantaMaster series spectrofluorometer. N_2 adsorption-desorption isotherms at 77 K were measured by using a Micrometritics ASAP 2420 system. A high-purity grade (99.999%) of gases was used throughout the adsorption experiments. Prior to adsorption measurement, the sample was activated by solvent exchange (in several cycles using fresh acetone), followed by degassing at elevated temperature (150 °C) for 5 h.

Synthesis

General procedure of hydrolysis: To a round bottomed flask, methyl ester compound (~500 mg) was dissolved in a mixture of THF and MeOH (100 mL, v/v = 1:1), and 50 mL 2 M KOH solution was added. The mixture was stirred and refluxed overnight at 40 °C. The organic phase was evaporated under reduced pressure. The resulting aqueous phase was diluted to ca. 100 mL and acidified with 6 M HCl. Resulting precipitates were collected, washed thoroughly with water, and dried to afford corresponding acid products.

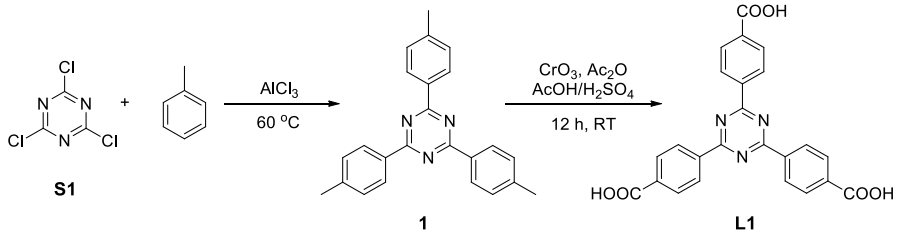

Scheme 2.1 Synthetic scheme of **L1**.

2,4,6-tri-p-tolyl-1,3,5-triazine (1). To a three neck flask, $AlCl_3$ (20 g) was dissolved in dry toluene and heated to 60 °C. $C_3N_3Cl_3$ (**S1**, 8.3 g) was then added portionwise for an hour and the mixture was stirred overnight. Then resulting red sticky oil was poured into a large amount of ice water to quench the catalyst and extracted with $CHCl_3$. After removing solvent, a crude product was precipitated out from methanol to yield a needle-like solid. Resulting solid was recrystallized from hot toluene to afford a white needle-like crystalline solid (10 g, 63%). ^{1}H NMR (300 MHz, $CDCl_3$): δ = 8.64 (d, 6 H), 7.35 (d, 6 H), 2.46 (s, 9 H).

4,4′,4″-s-triazine-2,4,6-triyl-tribenzoic acid (L1). To a 500 mL three-necked flask **1** (2.78 g) was dissolved in acetic acid (70 mL) and then 4.4 mL of H_2SO_4 was added. A solution of chromium oxide (7.2 g) in acetic anhydride (4.8 mL) was carefully added into the reaction flask with an ice bath. The resulting dark-green slurry was stirred overnight. The reaction mixture was poured into 250 mL cold water, stirred 1 h to well mixed, and filtered. The solids were washed with water to remove chromium acid. Dissolve the white solid in 200 mL 2 M NaOH solution. After the unreacted starting material was removed by filtration, the solution was acidified with 6 M HCl solution to give white crude product (until pH < 3). Resulting crude product was then filtered and dried. Recrystallization from DMF afforded pure product as a white solid (3.0 g, 86%). ^{1}H NMR (500 MHz, DMSO-d_6): δ = 13.35 (s, 3 H), 8.85 (d, 6 H), 8.20 (d, 6 H).

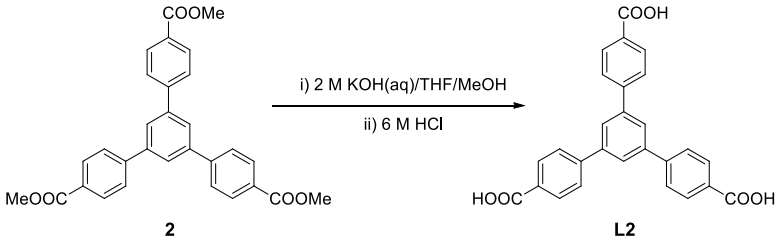

Scheme 2.2 Synthetic scheme of **L2**.

L2 was synthesized according to the literature procedure.[1] ^{1}H NMR (500 MHz, DMSO-d_6): δ = 8.09 (d, 6H), 8.06 (d, 6H), 8.04 (s, 3H).

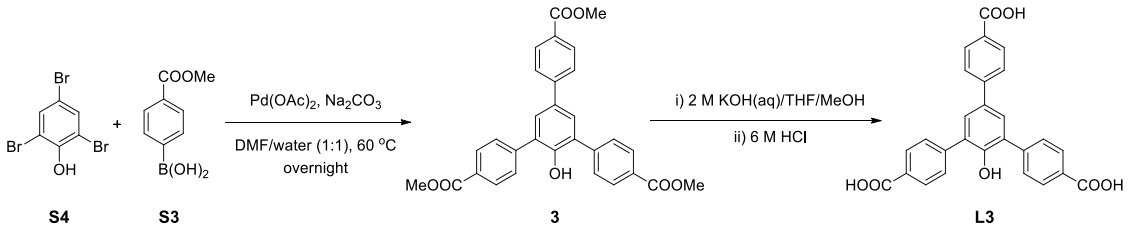

Scheme 2.3 Synthetic scheme of **L3**.

Dimethyl 2'-hydroxy-5'-(4-(methoxycarbonyl)phenyl)-[1,1':3',1''-terphenyl]-4,4''-dicarboxylate (3). A mixture of 2,4,6-tribromophenol (**S4**, 3 g, 9.06 mmol), (4-(methoxycarbonyl)phenyl)boronic acid (**S3**, 14.6 g, 91.1 mmol), Na_2CO_3 (6.7 g, 63.2 mmol), $Pd(OAc)_2$ (200 mg, 5 mol%) were dissolved in distilled water (100 mL) and degassed DMF (100 mL), and heated to 60 °C overnight under nitrogen atmosphere. Afterwards, the reaction mixture was poured into water, and pH value was adjusted to ~ 5. The resulting crude was filtered and washed with water. The crude product was purified by flash column chromatography on silica gel using progressively more polar to 1:1 mixture of hexanes: EtOAc as the mobile phase to afford **3** as a pale pink solid (3.6 g,

80%). ^{1}H NMR (300 MHz, $CDCl_3$): δ = 8.17 (d, 4H), 8.10 (d, 2H), 7.68 (m, 6H), 7.59 (s, 2H), 3.95 (s, 9H).

5'-(4-carboxyphenyl)-2'-hydroxy-[1,1':3',1''-terphenyl]-4,4''-dicarboxylic acid (L3). Compound **3** (500 mg) was hydrolyzed by following the *general procedure* described above to afford **L3** a light-brown solid (410 mg, 90%). ^{1}H NMR (500 MHz, DMSO-d_6): δ = 12.95 (s, 3H), 8.02 (d, 4H), 7.97 (d, 2H), 7.87 (d, 2H), 7.77 (d, 4H), 7.65 (s, 2H).

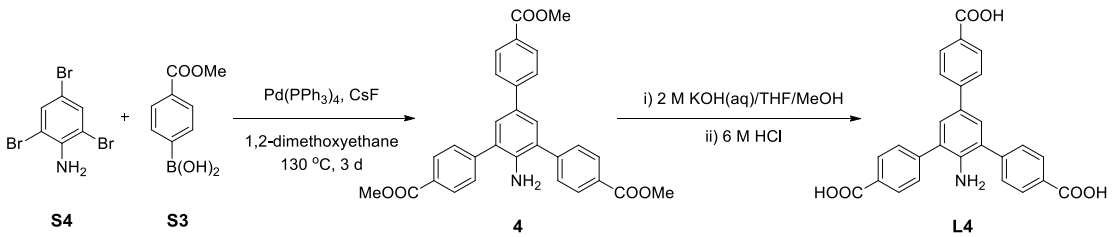

Scheme 2.4 Synthetic scheme of **L4**.

Dimethyl 2'-amino-5'-(4-(methoxycarbonyl)phenyl)-[1,1':3',1''-terphenyl]-4,4''-dicarboxylate (4). A mixture of 2,4,6-tribromoaniline (**S4**, 3.3 g, 10.0 mmol), 4-(methoxycarbonyl)phenyl)boronic acid (**S3**, 7.2 g, 40.0 mmol), CsF (6.0 g, 40.0 mmol), $Pd(PPh_3)_4$ (578 mg, 5 mol%) were dissolved in degassed 1,2-dimethoxyethane (300 mL), and heated to 130 °C to reflux overnight for 3 d under nitrogen atmosphere. Afterward, the solvent was dried under reduced pressure. The residue was washed with distilled H_2O and then extracted with CH_2Cl_2 followed by drying with anhydrous $MgSO_4$. After the solvent was removed, the crude product was purified by flash column chromatography on a silica gel (hexanes: EtOAc = 5: 1) to afford **4** as a light brown solid (4.16 g, 84%). ^{1}H

NMR (300 MHz, $CDCl_3$): δ = 8.18 (d, 4H), 8.08 (d, 2H), 7.66 (m, 6H), 7.45 (s, 2H), 3.96 (s, 9H).

2'-amino-5'-(4-carboxyphenyl)-[1,1':3',1''-terphenyl]-4,4''-dicarboxylic acid (L4). Compound **4** (500 mg) was hydrolyzed by following the *general procedure* described above to afford **L4** as a light-brown solid (435 mg, 95%). ^{1}H NMR (300 MHz, DMSO-d_6): δ = 8.10 (d, 4H), 7.98 (d, 2H), 7.85 (d, 2H), 7.74 (d, 4H), 7.52 (s, 2H), 4.74 (s, 2H).

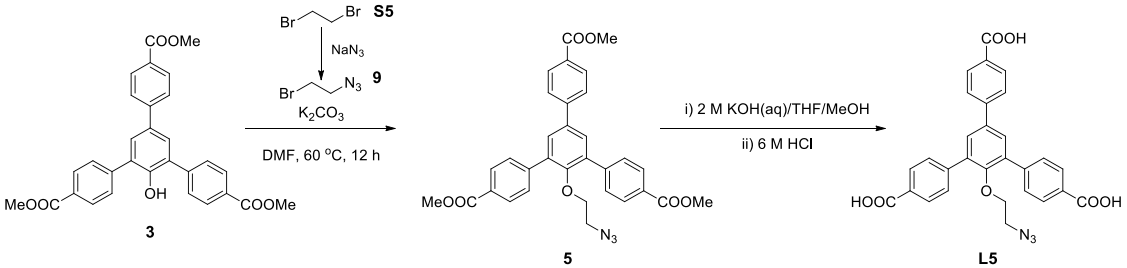

Scheme 2.5 Synthetic scheme of **L5**.

Azido-2-bromoethane (9). To dibromoethane (**S5**, 5 g, 27 mmol) dissolved in DMF (18 mL) sodium azide (1. 04 g, 16 mmol) was added portion-wise for 4 h. The reaction was then diluted with ether and the organic layer was washed with water. The organic layer was dried with $MgSO_4$ and concentrated under vacuum to afford **9** as a pale yellow oil (2.95 g, 73%). ^{1}H NMR (300 MHz, $CDCl_3$) δ = 3.72-3.62 (m, 2H), 3.48 (t, 2H).

Dimethyl 2'-(2-azidoethoxy)-5'-(4-(methoxycarbonyl)phenyl)-[1,1':3',1''-terphenyl]-4,4''-dicarboxylate (5). To a solution of compound **3** (500 mg, 1.07 mmol) and K_2CO_3 (442.6 mg, 3.195 mmol) in DMF (8 mL) was added compound **9** (800 mg, 5.35 mmol). The mixture was stirred at 60 °C 12 hours, and water was added. Afterwards, the crude product was extracted with dichloromethane and dried under reduced pressure.

The crude product was purified by flash column chromatography (hexanes: EtOAc = 6:1) to afford **5** as a pale yellow oil (574 mg, 95%). ^{1}H NMR (500 MHz, DMSO-d_6): δ = 8.08 (dd, 4H), 8.04 (d, 2H), 8.00 (d, 2H), 7.88 (dd, 4H), 7.83 (s, 2H), 3.96 (s, 9H), 3.13 (t, 2H), 3.05 (t, 2H).

2'-(2-azidoethoxy)-5'-(4-carboxyphenyl)-[1,1':3',1''-terphenyl]-4,4''-dicarboxylic acid (L5). Compound **5** (380 mg) was hydrolyzed by following the *general procedure* described above to afford **L5** as an ivory solid (350 mg, 99%). ^{1}H NMR (500 MHz, DMSO-d_6): δ = 13.04 (br, 3H), 8.05 (dd, 4H), 8.01 (d, 2H), 7.95 (d, 2H), 7.84 (dd, 4H), 7.79 (s, 2H), 3.52 (t, 1H), 3.32 (t, 1H), 3.13 (t, 1H), 3.05 (t, 1H).

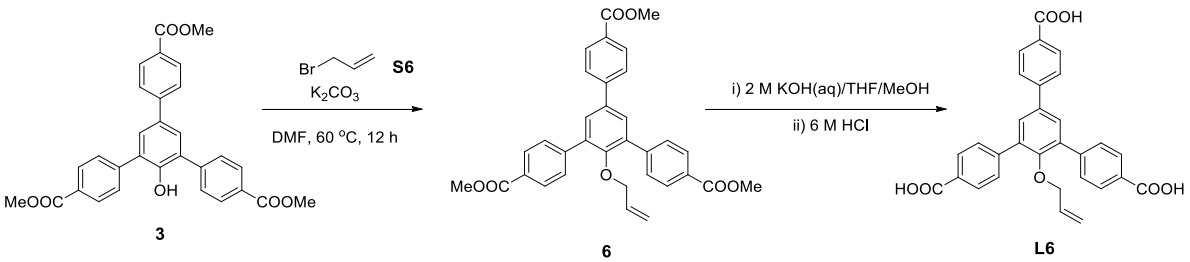

Scheme 2.6 Synthetic scheme of **L6**.

Dimethyl 2'-(allyloxy)-5'-(4-(methoxycarbonyl)phenyl)-[1,1':3',1''-terphenyl]-4,4''-dicarboxylate (6). To a solution of compound **3** (600 mg, 1.208 mmol) and K_2CO_3 (501 mg, 3.63 mmol) in DMF (8 mL) was added **S6** (365.4 mg, 3.02 mmol). The mixture was stirred at 65 °C 12 hours, and water was added. Afterwards, the crude product was extracted with dichloromethane and dried under reduced pressure. Resulting crude product was purified by flash column chromatography (hexanes: EtOAc = 6.5:1) to afford **7** as a white oil (520 mg, 80%). ^{1}H NMR (500 MHz, $CDCl_3$): δ = 8.11 (dd, 6H),

7.74 (d, 4H), 7.70 (d, 2H), 7.62 (d, 2H), 5.39 (qd, 1H), 4.89 (d, 1H), 4.84 (d, 1H), 3.96 (s, 9H), 3.74 (d, 2H).

2'-(allyloxy)-5'-(4-carboxyphenyl)-[1,1':3',1''-terphenyl]-4,4''-dicarboxylic acid (L6). Compound **6** (500 mg) was hydrolyzed by following the *general procedure* described above to afford **L6** a light-yellow solid (460 mg, 100%). ^{1}H NMR (500 MHz, DMSO-d_6): δ = 13.03 (br, 3H), 8.04 (d, 4H), 8.00 (dd, 2H), 7.95 (d, 2H), 7.83 (d, 4H), 7.78 (s, 2H), 5.40 (qd, 1H), 4.90 (d, 2H), 3.75 (d, 2H).

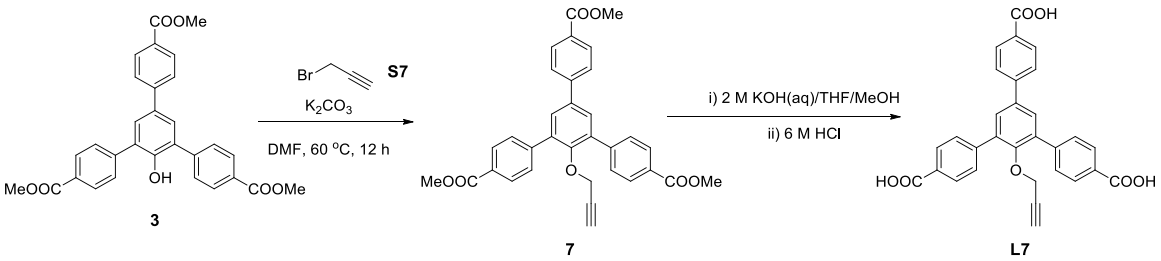

Scheme 2.7 Synthetic scheme of **L7**.

Dimethyl 5'-(4-(methoxycarbonyl)phenyl)-2'-(prop-2-yn-1-yloxy)-[1,1':3',1''-terphenyl]-4,4''-dicarboxylate (7). To a solution of compound **3** (500 mg, 1.07 mmol) and K_2CO_3 (414.6 mg, 3.21 mmol) in DMF (8 mL) was added **S7** (238 mg, 2.14 mmol). The mixture was stirred at 60 °C 12 hours, and water was added. Afterwards, the crude product was extracted with dichloromethane and dried under reduced pressure. Resulting crude product was purified by flash column chromatography (hexanes: EtOAc = 6:1) to afford **7** as a pale yellow oil (519 mg, 96%). ^{1}H NMR (300 MHz, DMSO-d_6): δ = 8.17-8.05 (m, 6H), 7.76 (d, 4H), 7.68 (d, 2H), 7.63 (d, 2H), 3.96 (s, 9H), 3.93 (s, 2H), 2.13 (s, 1H).

5'-(4-carboxyphenyl)-2'-(prop-2-yn-1-yloxy)-[1,1':3',1''-terphenyl]-4,4''-dicarboxylic acid (L7). Compound **7** (510 mg) was hydrolyzed by following the *general procedure* described above to afford **L7** a light-yellow solid (465 mg, 99%). ^{1}H NMR (500 MHz, DMSO-d_6): δ = 8.01 (m, 4H), 7.97 (d, 2H), 7.86 (d, 2H), 7.75 (d, 4H), 7.72 (s, 2H), 3.95 (d, 2H), 3.24 (t, 1H).

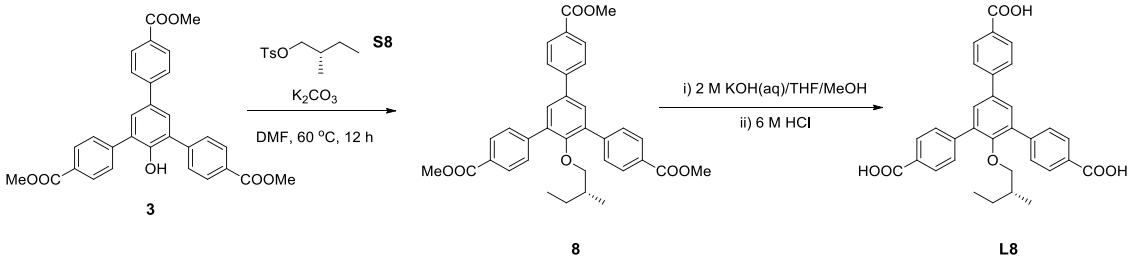

Scheme 2.8 Synthetic scheme of **L8**.

(R)-dimethyl 5'-(4-(methoxycarbonyl)phenyl)-2'-(2-methylbutoxy)-[1,1':3',1''-terphenyl]-4,4''-dicarboxylate (8). To a solution of compound **3** (2.0 g, 4.28 mmol) and K_2CO_3 (0.7 g) in DMF (30 mL) was added **S8** (1.2 g). The resulting mixture was heated to 60 °C for 12h. The crude mixture was extracted with dichloromethane, washed thoroughly with water, and dried to afford **8** as an ivory powder (2.1 g, 93%). ^{1}H NMR ($CDCl_3$) δ = 8.11 (m, 6H), 7.72 (m, 6H), 7.61 (s, 2H), 3.95 (m, 9H), 3.05 (m, 2H), 1.24 (m, 1H), 1.01 (m, 1H), 0.78 (m, 1H), 0.49 (m, 6H).

(R)-5'-(4-carboxyphenyl)-2'-(2-methylbutoxy)-[1,1':3',1''-terphenyl]-4,4''-dicarboxylic acid (L8). Compound **8** (500 mg) was hydrolyzed by following the *general procedure* described above to afford **L8** a white solid (400 mg, 86%). ^{1}H NMR (500 MHz,

DMSO-d_6) = 13.01 (br, 3H), 8.02 (m, 6H), 7.94 (d, 2H), 7.81 (d, 4H), 7.78 (s, 2H), 3.05-2.98 (ddd, 2H), 0.95 (m, 1H), 0.76 (m, 2H) ,0.46 (d, 3H) ,0.37 (t, 3H).

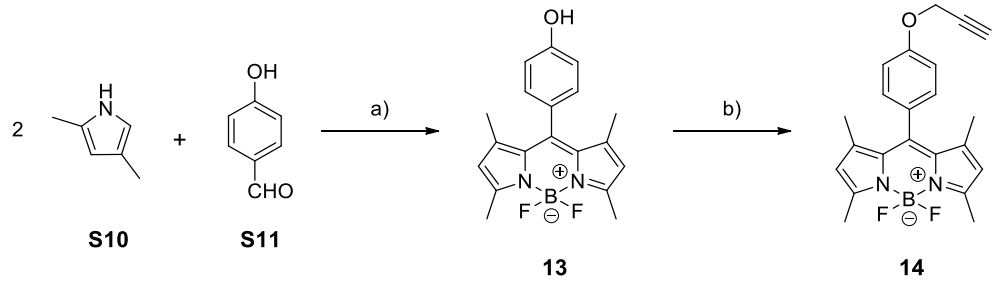

Scheme 2.9 Synthetic scheme of **14**. Reagents and conditions a) i) TFA, THF, 12 h, r.t., ii) DDQ, CH_2Cl_2, 5 h, r.t., iii) TEA, $BF_3{\cdot}OEt_2$, 12 h, r.t., 49%; b) propargyl bromide, K_2CO_3, acetone, 12 h, reflux.

5,5-difluoro-10-(4-hydroxyphenyl)-1,3,7,9-tetramethyl-5H-dipyrrolo[1,2-c:2',1'-f][1,3,2]diazaborinin-4-ium-5-uide (13). To a solution of **S11** (1 g, 8.19 mmol) and 2,4-dimethylpyrrole (1.85 mL, 18.02 mmol) in THF (150 mL) was added several drops of trifluoroacetic acid under a nitrogen atmosphere. The mixture was stirred at ambient temperature for 6 h, and the solution of 2,3-dichloride-5,6-dicyano-p-benzoquinone (2.05 g, 9.01 mmol) in THF (100 mL) was added. The resulting mixture was stirred continuously for another 5 h. After the addition of triethylamine (25 mL) and $BF_3{\cdot}OEt_2$ (31 mL) dropwise to the reaction mixture with an ice-water bath, the mixture was kept stirring at ambient temperature overnight, then filtered through Celite. The crude compound was washed with CH_2Cl_2 and the combined filtrate was evaporated to dryness. The residue was re-dissolved in CH_2Cl_2 and the solution was washed with 15% aqueous $NaHCO_3$ solution followed by water. The organic portion was dried over anhydrous $MgSO_4$, then evaporated. The crude product was purified by column chromatography on

silica gel using progressively more polar 50:1 to 9:1 (hexanes: EtOAc) as a mobile phase to afford **13** as an orange solid (1.2 g, 43%). ^{1}H NMR (500 MHz, $CDCl_3$): δ = 7.15 (d, 2H), 6.97 (d, 2H), 5.99 (s, 2H), 4.95 (br, 1H), 2.56 (s, 6H), 1.45 (s, 6H).

5,5-difluoro-1,3,7,9-tetramethyl-10-(4-(prop-2-yn-1-yloxy)phenyl)-5H-dipyrrolo[1,2-c:2',1'-f][1,3,2]diazaborinin-4-ium-5-uide (14). To a solution of compound **13** (300 mg, 0.882 mmol), K_2CO_3 (609.5 mg, 4.41 mmol) in dried acetone (100 mL) was added propargyl bromide (524 mg, 4.41 mmol). The mixture was heated to 55 °C and stirred for 12 h. Resulting mixture was evaporated to dryness and purified by column chromatography on silica gel using progressively more polar 50:1 to 15:1 (hexanes: EtOAc) as an eluent to afford **14** as a deep pink solid (175 mg, 53%). ^{1}H NMR (500 MHz, $CDCl_3$): δ = 7.20 (d, 2H), 7.09 (d, 2H), 5.98 (s, 2H), 4.76 (d, 2H), 2.55 (s, 6H), 2.17 (s, 1H), 1.42 (s, 6H).

Synthesis of PCN-333(Fe). H_3TATB (60 mg), anhydrous $FeCl_3$ (60 mg), and trifluoroacetic acid (0.6 mL) were dissolved in 10 mL of DEF. The mixture was heated in 150 °C oven for 12 h until a brown precipitate formed. The resulting brown precipitate was centrifuged and washed with fresh DMF several times. Yield (based on ligand) = ~ 85%.

Synthesis of PCN-333(Sc). H_3TATB (80 mg) and anhydrous $ScCl_3{\cdot}6H_2O$ (200 mg) were dissolved in 10 mL of DMF. The mixture was heated in 150 °C oven for 2 h until a white precipitate formed. The resulting white precipitate was centrifuged and washed with fresh DMF several times. Yield (based on ligand) = ~ 85%.

Direct synthesis of PCN-260. BTB (10 mg), $FeCl_3$ or $Fe_2CoO(CH_3COO)_6$ (10 mg), and acetic acid (0.25 mL) in 2 mL of NMP were ultrasonically dissolved in a Pyrex vial. The mixture was heated in 150 °C oven for 24 h. After cooling down to room temperature, dark brown crystals were harvested by filtration.

Direct synthesis of PCN-262. OH-BTB (10 mg), $FeCl_3$ or $Fe_2NiO(CH_3COO)_6$ (10 mg), and acetic acid (0.20 mL) in 2 mL of DMF were ultrasonically dissolved in a Pyrex vial. The mixture was heated in 150 °C oven for 15 h. After cooling down to room temperature, dark brown crystals were harvested by filtration.

General procedure for ligand exchange of PCN-333(Fe)

First, synthesized PCN-333(Fe) (ca. 50 mg) was thoroughly washed with hot DMF, and the isolated sample was then incubated with a stock solution of BTB or BTB derivatives (50–55 mg in DMF) at different temperatures (rt, 85 °C, 100 °C). Upon completion of ligand substitution, the supernatant was removed to examine whether there was TATB that came from the parent MOF after the exchange of ligand. The aliquot of supernatant was filtered through a syringe filter to exclude the possibility of exchanged PCN-333(Fe) crystals remaining, and ligands were recovered by acidification with few drops of 1 M HCl, followed by washing with water. The resulting precipitates were dried and analyzed by ^{1}H NMR spectroscopy.

MOF digestion

Approximately 15 mg of each ligand exchanged PCN-333(Fe) sample was digested with 37% HCl, refluxed overnight, and washed with water until a neutral pH was

reached. DMSO-d_6 (0.6 mL) was added to dissolve the ligands. The ^{1}H NMR spectrum (500 MHz) of exchanged PCN-333(Fe) was collected at room temperature (~21 °C).

Click reaction

Compound **14** (5 mg) was added to a mixture of azide-BTB exchanged PCN-333(Sc) (10 mg) and CuI (0.5 mg) in THF (1.0 mL) in a 4 mL vial. The reaction mixture was stirred at 60 °C for 20 h. The resulting precipitate was collected by centrifugation, washed thoroughly with DMF followed by acetone, and dried to afford a light brown solid in quantitative yield.

2.3 Results and discussion

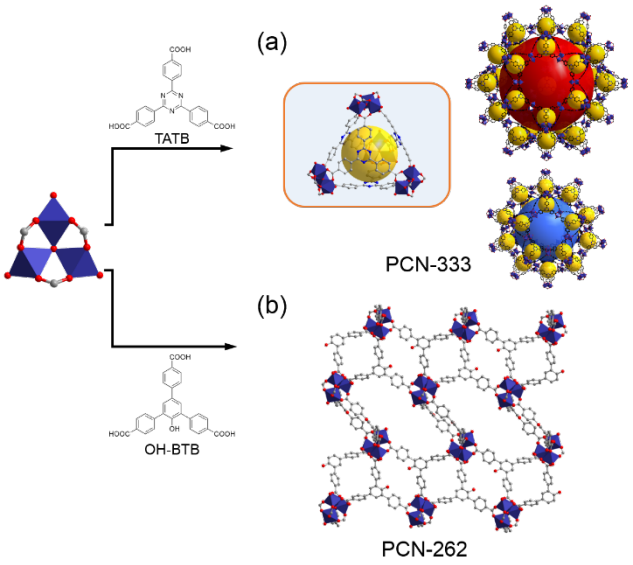

Figure 2.1 Structure of PCN-333 with three different cages. (a) Structure of PCN-333 with three different cages. (b) Structure of PCN-262, direct synthesis product from OH-BTB.

Direct synthesis of isoreticular structure of functionalized PCN-333(Fe)

Most recently, our group reported a mesoporous MOF, PCN-333, which consists of a trimeric metal cluster and tritopic linker, 4,4′,4″-s-triazine-2,4,6-triyl-tribenzoic acid (TATB).[40] PCN-333 [$M_3O(OH)(TATB)_2$] (M = Fe, Al, Sc) exhibits the largest cage of 5.5 nm among all reported MOFs (Figure 2.1). Meanwhile, the trivalent metal nodes endow PCN-333 with excellent chemical stability allowing for its utilization under harsh conditions. Therefore, decoration of PCN-333 with covalent anchors would provide a great platform to immobilize versatile functional species, especially those in the nanoscale, which cannot be successfully accomplished by other MOFs.

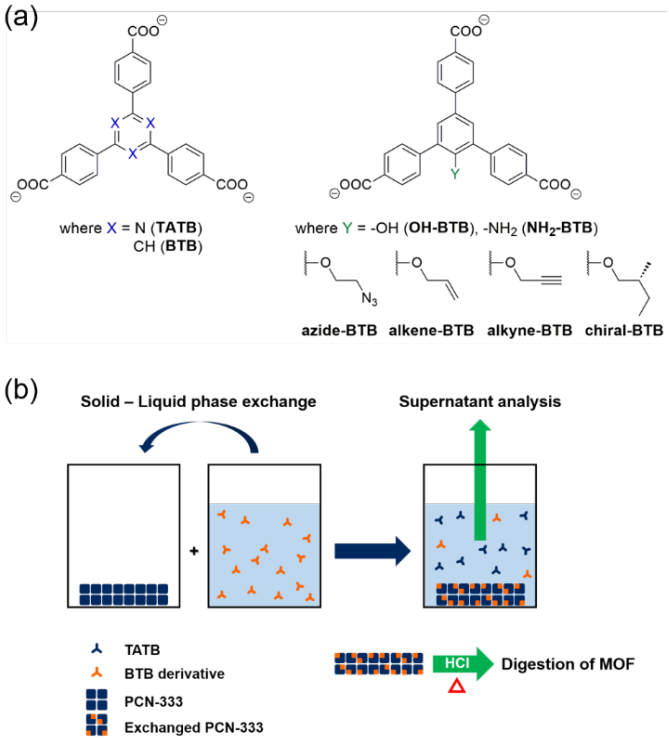

Scheme 2.10 (a) Library of ligands involved in exchange in PCN-333. (b) Schematic illustration of solid-liquid phase ligand exchange.

Having examined the PCN-333 structure, we chose 1,3,5-benzenetribenzoic acid (BTB) to exchange TATB due to the structural resemblance including molecular size and connectivity. As a result of the 2-position on the central benzene ring of BTB allowing for chemical derivatization (Scheme 2.10a), the functionalized BTB derivative was expected to introduce various covalent anchors into the mesoporous PCN-333. A series of ligands bearing different functional groups were synthesized. The covalent anchor was designed to occupy only a small portion of the pores while leaving most space available for the immobilization of large guest species. Therefore, we intuitively attempted a direct synthesis of functionalized PCN-333 from preinstalled functional groups on the BTB derivatives. Direct synthesis was performed by using the kinetically tuned dimensional augmentation (KTDA) method with preformed cluster $Fe_3(O)(CH_3COO)_6$ as a starting material to obtain isoreticular structures of PCN-333 with BTB and OH-BTB.[41] Although large single crystals of Fe-MOFs, PCN-260, and PCN-262 were harvested, respectively, single crystal X-ray diffraction revealed different structures even in the presence of the same inorganic building block, $Fe_3(O)(COO)_6$, as in PCN-333 (Figure 2.1b).

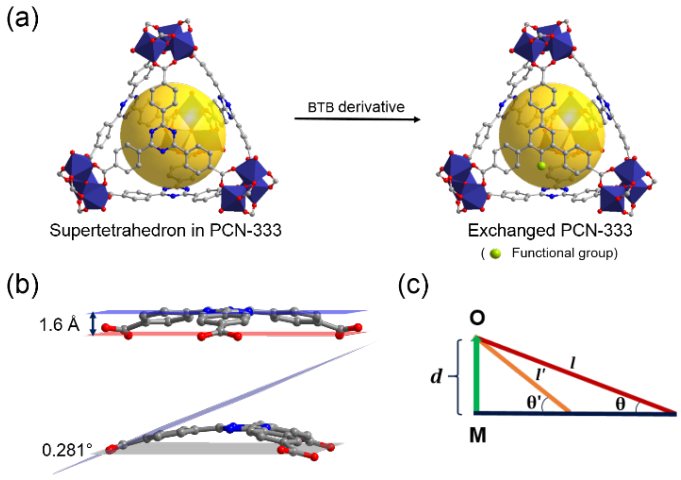

Figure 2.2 Scheme of ligand exchange in (a) supertetrahedron in PCN-333. (b) One face of supertetrahedron in PCN-333 showing the distance (top) and the angle (bottom) in the bent geometry. (c) Schematic illustration of M-O dissociation.

As shown in Figure 2.2a, the structure of PCN-333 is built from a supertetrahedron unit, of which each face is a TATB linker. Although TATB does not adopt perfect D_{3h} symmetry in the framework, six oxygen atoms on TATB reside in the same plane which gives rise to a stable tetrahedral cage in C_{3v} symmetry from bent geometry (Figure 2.2b). However, coplanar D_{3h} symmetry of BTB is highly energetically unfavored due to the repulsion between H atoms on the central benzene ring and the three peripheral benzene rings. With BTB derivatives, the attached functional groups on the central benzene ring would cause additional steric hindrance resulting in even higher energy of the coplanar geometry. Considering *in situ* MOF synthesis, when possible inorganic nodes have a negligible energy difference, a major product is dominated by energy demands of linkers. Because free rotation of single bonds in the BTB derivative allows the linker to stay in a lower energy conformation in solution, TATB and BTB derivatives could lead to different structures with the same inorganic node, $Fe_3(O)$, where preferential conformation

of linkers dominates the final products. Although the isostructure of PCN-333 constructed with BTB has been reported,[35] the functionalized isoreticular structure of PCN-333 cannot be achieved through the direct synthetic approach.

Structure-assisted ligand exchange process

Due to ligand conformation dominating the framework growth process in direct synthesis leading to an unwanted structure, we turned to the postsynthetic ligand exchange method.[42-64] Postsynthetic ligand exchange (PSE) and solvent-assisted linker exchange (SALE) have appeared as powerful routes to modify a parent MOF in which the ligand exchange occurs in relatively stable MOFs with a functionalized incoming ligand. For instance, Cohen and co-workers studied ligand exchange in UiO-66(Zr), and several MIL series with bromo and amino analogues of the original ligands.[49,54,64] The Hupp group also demonstrated solvent-assisted linker exchange in a ZIF series.[45,46] Also, using stepwise ligand exchange strategy, establishment of extended isoreticular structures has been studied.[43,53,55] To establish a versatile platform having large pores and chemical stability via postsynthetic ligand exchange in PCN-333(Fe), we started from BTB, the simplest form bearing a resemblance to TATB, as the exchanging ligand. With thoroughly washed PCN-333(Fe), ligand exchange was performed via a biphasic (solid–liquid) manner as illustrated in Scheme 1b. To exclude a dissolution–recrystallization pathway, the exchange reaction was performed under lower temperature than that of the MOF synthetic condition.

Despite many noticeable examples that have shown postsynthetic ligand exchange in stable MOFs, there has not yet been a successful example demonstrating ligand

exchange in extremely stable mesoporous MOFs, such as MIL-100 and MIL-101, although both MOFs have been widely employed in many applications. Surprisingly, a successful ligand exchange was achieved in PCN-333(Fe) by using BTB as the incoming ligand. In general, most ligand substitution reactions in octahedral complexes undergo a dissociative pathway. The rate-determining step in the dissociative pathway is known to be a breaking of metal–ligand (M–L) bond.[65,66] Similarly, the ligand exchange process in MOF can be generalized to the principle in coordination chemistry that the M–L bond should be dissociated to exchange ligands. MIL-101 and MIL-100 have been reported as extremely robust frameworks, suggesting strong coordination (M–L bond) in these two MOFs which in turn leads to an extremely slow bond dissociation rate for the ligand exchange. One reason that could account for this is the strong electrostatic interaction between carboxylates and the high Z/r valued trivalent metal ions used in these MOFs. To achieve an effective ligand exchange, therefore, longer reaction time and/or higher temperature might be expected in these frameworks.

However, the exchanging environment provides not only extra carboxylates (from incoming ligands) but also solvent molecules as competing reagents, both of which could destruct the framework by forming fractions or amorphous products. Therefore, in the extremely robust MIL-101 and MIL-100, the frameworks could be severely damaged before an apparent exchange happens. On the contrary, PCN-333(Fe), an isoreticular structure of MIL-100, showed successful ligand exchange. As the bond nature is identical in both frameworks, the elongation of the linker could explain the exchange event. Unlike common coordination complexes, each linker in MOFs binds to multiple metal nodes.

Considering that a complete ligand exchange of a linker includes breaking of all coordinated carboxylates, the case where only one of them is dissociated while the others remain bound onto the framework prevents total dissociation. Consequently, the structural restraint from multiple coordination sites impedes complete ligand dissociation, which eventually slows the ligand exchange in the framework. In addition, when the connectivity of the linker is higher, it takes more steps for the complete ligand dissociation, resulting in a more difficult exchange process. Furthermore, for similar linkers of differing length, the extent of such restraint varies. For instance, assuming *d* in Figure 2.2b (describing only one binding site) stands for a distance allowing for efficient dissociation–association of the ligand exchange. When the dissociation is happening (moving distance to *d*), longer linker *l* takes a smaller angle θ compared to that of shorter linker *l*′, which would result in less strain to the remaining coordination sites on the linker. If *l* gets infinitely longer, then the structural restraint from each coordination site becomes negligible, and the dissociation process in the MOF would be similar to the case of a small coordination complex in a homogeneous system. Therefore, ligand exchange can happen more easily in isoreticular structures constructed with longer linkers.

In the supertetrahedron of PCN-333, $Fe_3(O)$ clusters act as vertexes. The dihedral angle between the carboxylate plane and the $Fe_3(O)$ plane is inherently determined by the octahedral coordination environment of each Fe atom. However, it is not precisely compatible to be directly connected in the triangular face of a perfect tetrahedron (0.281°) as shown in Figure 2.2b. Thus, TATB must adopt a bent geometry to hold three $Fe_3(O)$ clusters in the supertetrahedron unit. This generates a distance of about 1.6 Å between the

center of TATB and the ideal triangular plane formed by six oxygen atoms in the tetrahedron, which suggests TATB would bear high energy (Figure 2.2b). Although bond dissociation happens between the carboxylate and Fe, such an energetically unfavorable conformation would still facilitate the dissociation in order to lower the energy of the linker. In the meantime, TATB is almost twice as large as benzene-1,3,5-tricarboxylic acid (BTC), which makes all cages in PCN-333 much larger than that in MIL-100, and thereby such extra space allows for faster diffusion of both incoming and dissociating ligands to further promote the ligand exchange process in PCN-333. All structural features of PCN-333 including the greatly bent conformation of TATB, less mutual restriction between each coordinating site because of its larger size (compared to MIL-100), and extremely large pores assist the ligand exchange in spite of the strong M–L bond, all combined make this system the first example of successful ligand exchange in highly robust mesoporous MOF with tritopic linkers.

Optimization of ligand exchange in PCN-333(Fe) with BTB

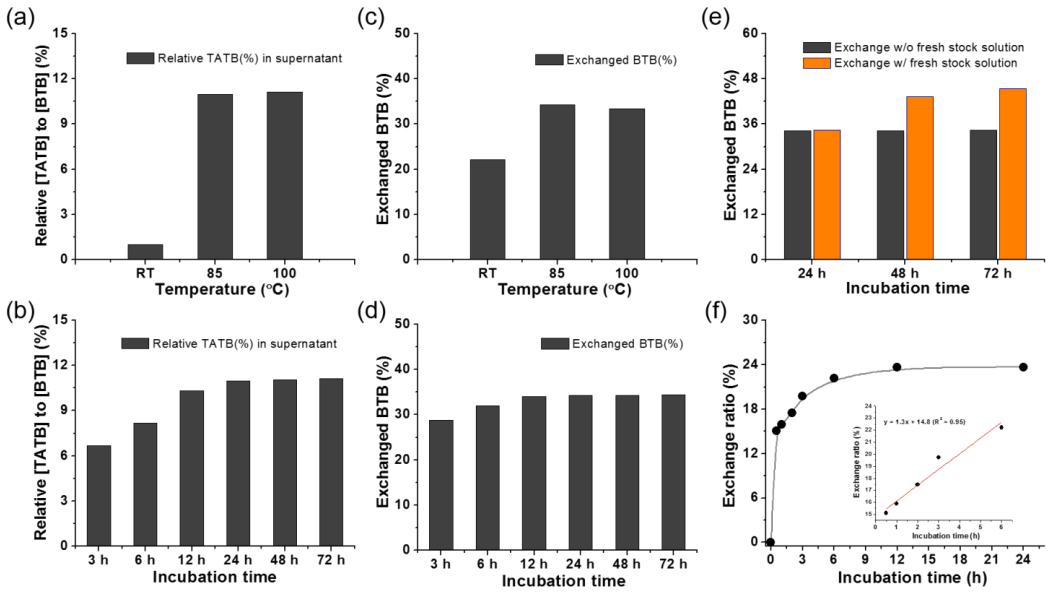

Figure 2.3 NMR studies of ligand exchange. (a) Relative TATB (%) in supernatant at different temperatures (incubation time = 24 h). (b) Time-dependent relative TATB (%) in supernatant (incubation temperature = 85 °C). (c) Ratio of exchanged BTB (%) in PCN-333(Fe) incubated at different temperatures (incubation time = 24 h). (d) Ratio of exchanged BTB (%) in PCN-333(Fe) at different incubation times (incubation temperature = 85 °C). (e) Comparison of BTB exchange ratio (%) in PCN-333(Fe) upon provision of fresh stock solution. (f) BTB exchange ratio (%) in PCN-333(Sc) as a function of incubation time.

Systematic studies to further investigate the ligand exchange process in PCN-333(Fe) were performed. First, PCN-333(Fe) was incubated for 24 h in BTB stock solution at different temperatures [room temperature (rt), 85 °C, 100 °C]. Upon completion of ligand exchange, the relative composition of the ligands (BTB was used excess amount) was analyzed by ^{1}H NMR of the resulting supernatant. The ligand exchange reaction at room temperature showed the lowest content of TATB (~1%) while both higher temperatures (85 °C, 100 °C) yielded higher contents of TATB (~11% for both) coming

out from the parent MOF, which indicates the ligand exchange was facilitated at higher temperatures (Figure 2.3a). Next, the ligand exchange process was investigated for different incubation times. The supernatants of BTB exchanged PCN-333(Fe) samples were taken after different incubation times at 85 °C. The ^{1}H NMR spectroscopy showed the supernatant incubated for 3 h was composed of ~7% of TATB relative to BTB and the ratios of TATB gradually increased as incubation time increased up to 24 h. However, the exchange ratios were saturated at a longer period of exchange process (72 h), and almost the same concentrations of TATB were obtained (~11%) (Figure 2.3b).

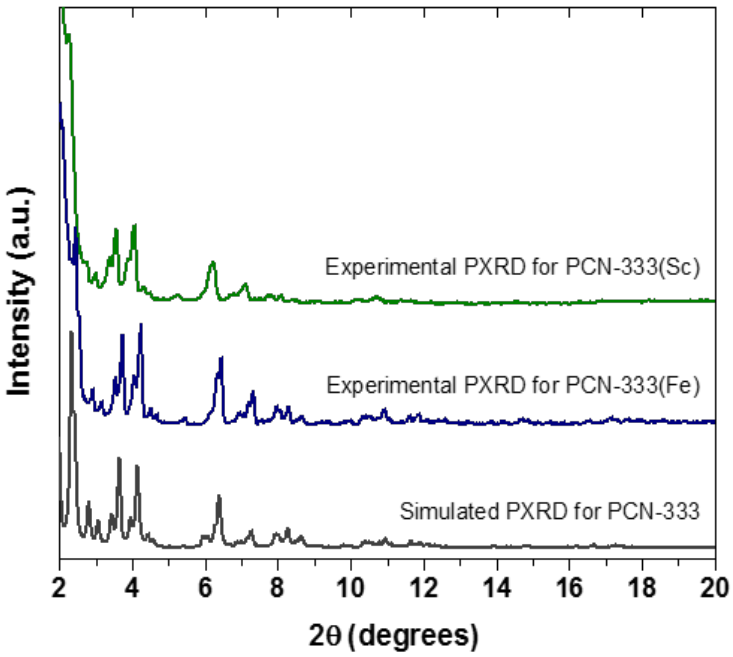

Figure 2.4 PXRD patterns of synthesized materials.

As supernatant analyses merely indicate the exchange event indirectly, ^{1}H NMR spectroscopy of digested MOFs was performed to determine the absolute composition of

exchanged PCN-333(Fe). Due to the high chemical stability of exchanged PCN-333(Fe), the samples were treated with concentrated HCl (37%) and refluxed for 12 h to be digested. The digested sample that was incubated at room temperature showed 22% exchange of BTB. Consistent with the previous observations from the supernatant, the samples exchanged at 85 and 100 °C showed higher extent of exchange, 34% and 33%, respectively (Figure 2.3c). The effect of incubation time was also examined on the digested samples. The exchange ratios gradually increased from 29% (3 h exchanged sample) to ~34% (12–72 h exchanged samples) (Figure 2.3d). Similar to the results from supernatant studies, the composition of BTB did not increase with extension of incubation time longer than 24 h. Ligand exchange in PCN-333(Fe) showed a faster rate of exchange in that approximately 30% exchange could be achieved within 3 h under mild conditions. Also, these findings clearly showed promise that the degree of exchange can be modulated by controlling temperature and exchange time. Powder X-ray diffraction of these samples indicates that the structural integrity of parent PCN-333(Fe) was well-retained after the ligand exchange (Figure 2.6a).

After discovering the previous result, we further sought to find whether the exchange ratio could become higher or whether there would be a maximum extent of exchange within a capacity allowing the retention of framework. To drive the equilibrium of the system forward, the supernatant was exchanged with fresh BTB stock solution every 24 h. Ligand exchange was performed by following the routine procedure at 85 °C. A higher BTB exchange ratio (~45%) was achieved when the fresh stock solution was provided after 24 h during 48 h of exchange. However, there was no significant increase

when fresh BTB solution was subsequently provided each day for longer periods of time (Figure 2.3e).

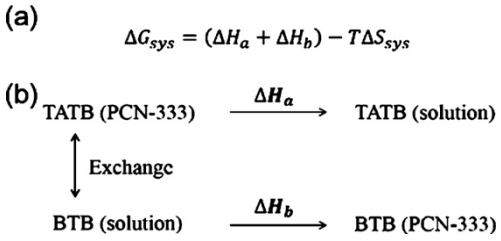

Figure 2.5 Entropy and enthalpy changes of the system during ligand exchange. (a) Gibbs free energy change of the system for ligand exchange in PCN-333. (b) Enthalpy change of the system during ligand exchange.

Thermodynamics behind ligand exchange in PCN-333

Having observed that the exchange ratio stopped increasing after a certain point despite successive provision of fresh incoming ligands while maintaining crystallinity of PCN-333(Fe), we further sought to understand the process in our system. At the very beginning of the ligand exchange process, the drastic entropy increase (ΔS_{sys}) results in a negative ΔG_{sys}, which spontaneously drives the exchange reaction forward. When the concentration of TATB in solution increases up to a certain point, ΔS_{sys} would be insufficient to maintain the negative value of ΔG_{sys}, and eventually, an equilibrium is established where $\Delta G_{sys} = 0$. Such rationale is consistent with the experimental results that the maximum exchange ratio was observed for each batch of BTB exchanged sample.

Thus, the exchange of fresh BTB stock solution reinitiated the high entropy increasing process. To some extent, a new equilibrium was established, but over time the exchange ceased again. Ideally, the ligand exchange process could keep going close to full

exchange (~100%) upon successive provision of fresh incoming ligands. In the case of PCN-333, however, the exchange process was terminated when the system reached a certain exchange ratio regardless of whether refilling of fresh BTB solution occurred (Figure 2.3e). This may imply the total enthalpy change ($\Delta H_a + \Delta H_b$) is no longer the same value as in the circumstance of low BTB exchange ratio in PCN-333. In other words, ΔH_b becomes an even larger positive value whereas ΔH_a remains the same, which leaves the framework in high energy when more BTB molecules are inserted after the maximum tolerance that PCN-333 can bear until its destruction. As a result, the ligand exchange can hardly be driven further by the entropy change (ΔS_{sys}) due to the huge enthalpy increase ($\Delta H_a + \Delta H_b$) and the saturation point appears. Theoretically, raising the temperature (increasing $T\Delta S_{sys}$ value) could overcome such enthalpy increase ($\Delta H_a + \Delta H_b$) to further drive the ligand exchange process. However, the increased temperature could also destroy the framework as previously discussed. Thus, a balance must be struck by controlling temperature to affect optimum ligand exchange process while maintaining framework integrity.

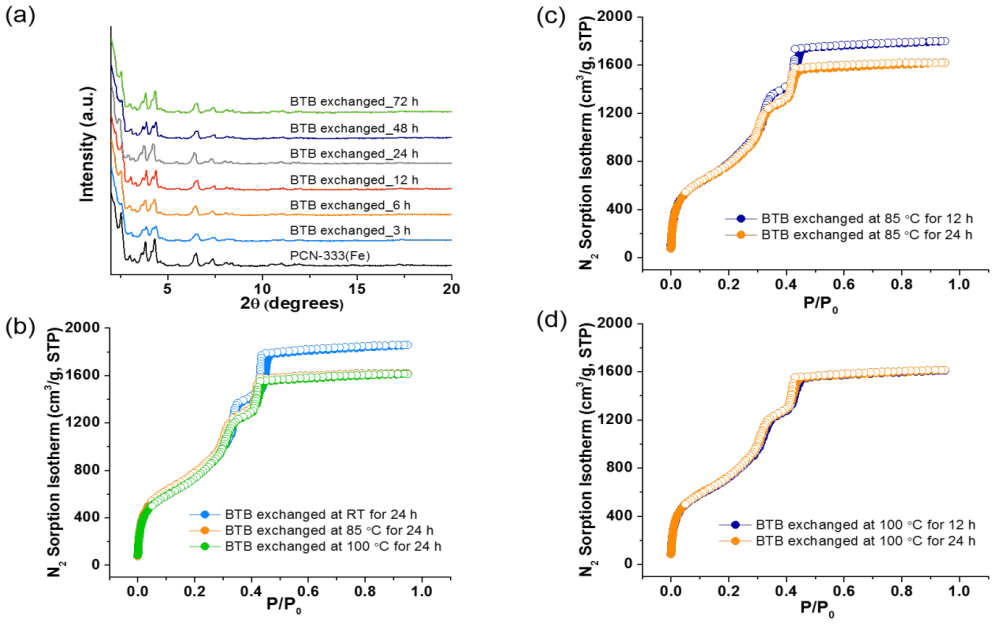

Figure 2.6. Characterization of BTB exchanged PCN-333(Fe). (a) PXRD patterns of BTB exchanged PCN-333(Fe) for different incubation times. Ligand exchange was performed at 85 °C. (b) N_2 sorption isotherms of BTB-exchanged PCN-333(Fe) performed at different temperatures. (c) N_2 sorption isotherms of BTB-exchanged PCN-333(Fe) for different incubation times at 85 °C. (d) N_2 sorption isotherms of BTB exchanged PCN-333(Fe) for different incubation times at 100 °C.

To examine whether an *exchange saturation point* (maximum exchange ratio) lies on the thermodynamic equilibrium, we further carried out a reverse ligand exchange reaction using extra TATB to replace the inserted BTB in the exchanged PCN-333. When TATB from the solution replaces the inserted BTB in the framework, the enthalpy change will be inversed to a negative value, $-(\Delta H_a + \Delta H_b)$. Because the entropy change maintains a similar trend (a positive value), the overall change in Gibbs free energy will become negative to spontaneously drive the exchange process (reverse reaction). As expected, after soaking BTB-exchanged PCN-333(Fe) into TATB solution for 12 h at 85 °C, the composition of BTB in the reversibly exchanged PCN-333(Fe) decreased from ~35% to

less than 6% with well-retained crystallinity, validating the explanation for the presence of the *exchange saturation point* in the system.

As previously discussed, framework destruction is inevitable during the ligand exchange process due to the competing association–dissociation at the M–L bond from extra ligands in the solution and some solvent dissociatives such as formate. When the exchange is extremely slow, the framework can be destroyed before evident exchange happens, which would result in unsuccessful exchange as in the case of MIL-101 and MIL-100. In order for successful ligand exchange in the robust MOF, optimization becomes important to balance the exchange ratio and framework intactness. To optimize such a balance of the exchange ratio, porosity and crystallinity of exchanged PCN-333(Fe), the nitrogen sorption measurement and PXRD were employed. As shown in Figure 5b, when the exchange reaction was conducted for 24 h at different temperatures, the lower temperature (rt) gave the better porosity than that of higher temperatures (85 °C, 100 °C). Although a slight decrease in porosity (~13%; relative to the parent MOF) was observed for the samples treated at higher temperatures, they still exhibited high porosity. We then examined whether the incubation time affects the porosity as well. For the exchanged PCN-333(Fe) incubated at 85 °C, shorter reaction time (12 h) rendered better porosity than that of longer exchange time (24 h) (Figure 2.6c).

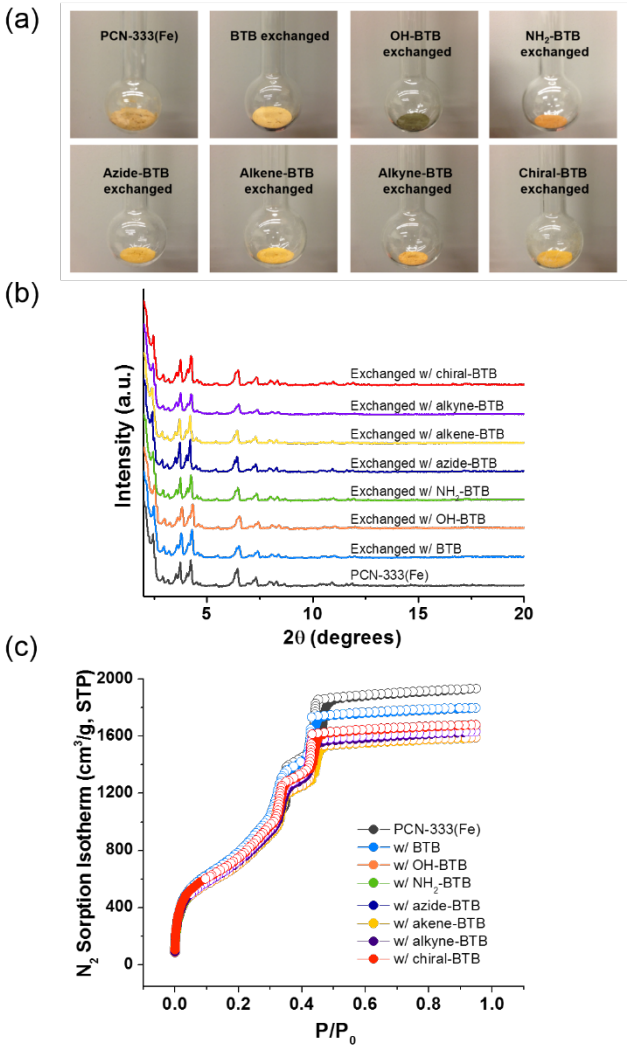

Figure 2.7 (a) Photographs of PCN-333(Fe) samples after ligand exchange with different BTB derivatives (after activation). (b) PXRD patterns of exchanged PCN-333(Fe) with different BTB derivatives. (c) Nitrogen sorption isotherms of PCN-333(Fe) exchanged with different BTB derivatives. Incubation temperature = 85 °C. Incubation time = 12 h.

Ligand exchange with various functional groups

One of the most valuable advantages of MOFs over other conventional porous materials is synthetic versatility from the design of diverse ligands. Utilizing the powerful tool of organic chemistry, we sought to expand our library of ligands to accommodate

various functional groups in PCN-333(Fe) through the structure-assisted ligand exchange process. Most incoming BTB derivatives with various substituents at the 2-position of the central benzene ring (Scheme 2.10a) were synthesized from OH-BTB via a simple nucleophilic substitution reaction with excellent quantitative yields.

Table 2.1 Summary of N_2 sorption isotherm measurement.

Ligand	Exchange ratio (%)[a]	N_2 uptake (cm^3/g, STP)[b]	BET surface area (m^2/g)
BTB	35.0	1797	3903
OH-BTB	27.5	1657	3595
NH_2-BTB	18.0	1632	3448
azide-BTB	31.0	1676	3559
alkene-BTB	26.5	1587	3391
alkyne-BTB	39.4	1631	3463
chiral-BTB	27.3	1679	3624

[a]Ligand exchange was performed at 85 °C for 12 h. [b]N_2 sorption was measured at 77 K.

Ligand exchange of BTB derivatives in PCN-333(Fe) was performed by adopting the optimized condition from BTB exchange studies (85 °C, 12 h). A 12 h period of incubation time was chosen as a shorter reaction time and gave better porosity with compatible extent of exchange. Photographs of the exchanged samples are shown in Figure 2.7a. Notably, distinctive color changes were observed for the samples exchanged with OH-BTB (olive) and NH_2-BTB (dark brown), which clearly indicate the incorporation of different ligands. To determine the exchange ratio for each ligand, ^1H NMR spectra of the digested samples were taken. The exchange ratio for each ligand is summarized in Table 2.1. Presumably due to different enthalpy changes (ΔH_b) of each ligand before and after ligand exchange resulting from their different solubility as well as

steric and/or electronic effects, each ligand showed different extent of exchange ranging from 18.0% to 39.4% under identical conditions. Nevertheless, all of the functionalized BTB ligands were successfully exchanged into PCN-333(Fe) with significant exchange ratios. Figure 2.7b shows well-maintained crystallinity of exchanged samples regardless of the functional groups (Figure 2.7b).

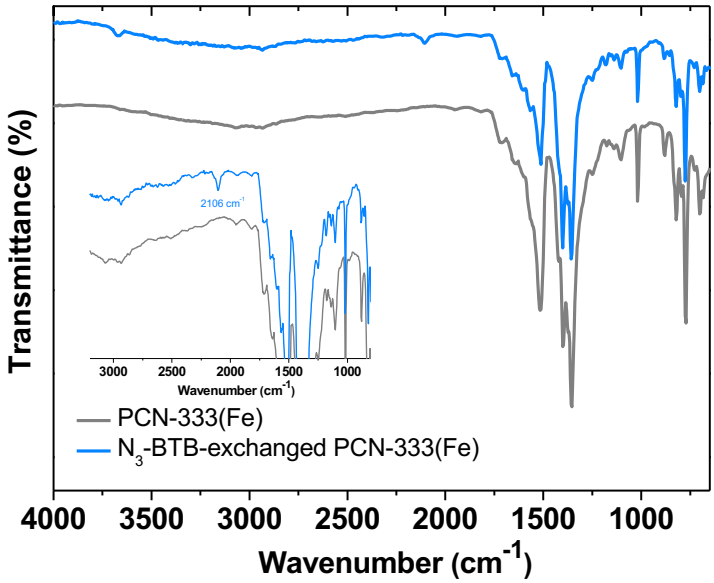

Figure 2.8 IR spectra of azide-BTB exchanged PCN-333(Fe). Inset: magnification of characteristic azide group stretching band at ~ 2100 cm^{-1}.

Particularly, infrared (IR) spectroscopy of the azide-BTB exchanged PCN-333(Fe) shows a characteristic stretching band at 2106 cm^{-1}, which is indicative of the presence of an azide group (Figure 2.8). The porosity of each exchanged PCN-333(Fe) sample was then evaluated by N_2 adsorption measurements at 77 K. As expected, the total uptake of each sample slightly decreased after the exchange with a functionalized ligand (Figure 2.7c). However, it is worth noting that the decrease in total pore volume of

exchanged PCN-333(Fe) compared to that of the parent material was not critical (approximately decreasing in a range from 7% to 18%, Table 2.1). To the best of our knowledge, our materials exhibit one of the highest N_2 uptakes among all reported mesoporous MOFs with functionalized covalent anchors.[39,55] Slight shifts to the lower pressures in steps of the N_2 adsorption isotherm, in comparison to that of the parent material at approximately 0.32 P/P_0 and 0.44 P/P_0, were observed suggesting changes in pore size due to the incorporation of ligands with substituents. DFT pore size distribution analysis showed that the smallest pore, which corresponds to the supertetrahedron unit, was affected the most by appended functional groups on the BTB derivatives compared to that of parent MOF. For example, the pore size distribution of the PCN-333(Fe) exchanged with azide-, alkene-, alkyne-, and chiral-BTB that contains larger functional groups showed a sharper shift in distribution toward the smaller pores than that of BTB, OH-BTB, or NH_2-BTB exchanged PCN-333(Fe). In comparison, the middle-sized cages and the largest cages are less affected. Assuming the inserted BTB derivatives are well-distributed, the exchange extent exceeding 25% would suggest at least one face of the supertetrahedron is replaced. While the additional functional groups reduce the available space inside of the smallest cage, the middle-sized and especially the largest cages are much less affected due to their inherent ultralarge pores. Therefore, characteristics of mesoporous PCN-333 should be mostly preserved after the implantation of the functional anchors.

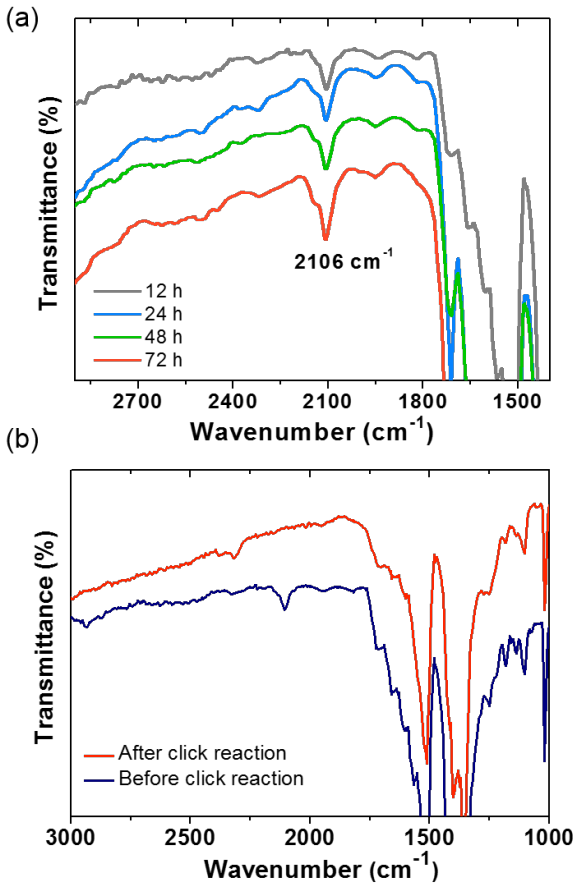

Figure 2.9 Click reaction of azide-BTB exchanged PCN-333(Fe). (a) IR spectra of azide-BTB exchanged PCN-333(Fe) having different ratios of azide-BTB. (b) Comparison of IR spectra of before/after click reaction with azide-BTB exchanged PCN-333(Fe).

Introduction of secondary functionality

After successful implantation of covalent anchors into PCN-333, further examinations were performed on azide-functionalized PCN-333(M) (M = Fe, Sc) to demonstrate introduction of secondary functionality via click chemistry.[39,44,67] As previously found, before reaching the exchange saturation point providing fresh stock solution of the incoming ligand increased the exchange ratio.

Taking this into account, the characteristic peak of the azide group at 2106 cm^{-1} was monitored by infrared spectroscopy upon increasing the azide group ratio. As fresh stock solution was continuously provided, a more prominent azide stretching band at 2106 cm^{-1} was observed in the exchanged sample which indicates the incorporation of more azide-BTB ligands in PCN-333(Fe) (Figure 2.9a). Knowing this, a click reaction between the azide-functionalized PCN-333(Fe) and methyl propiolate was performed in the presence of CuI in DMF (65 °C, 20 h). The disappearance of this azide IR peak at 2106 cm^{-1} shown in Figure 2.9b suggests a successful anchorage of methyl propiolate as well as completion of the click reaction. The PXRD pattern of the clicked sample also confirmed well-maintained crystallinity owing to the robustness of PCN-333(Fe) (Figure 2.10).

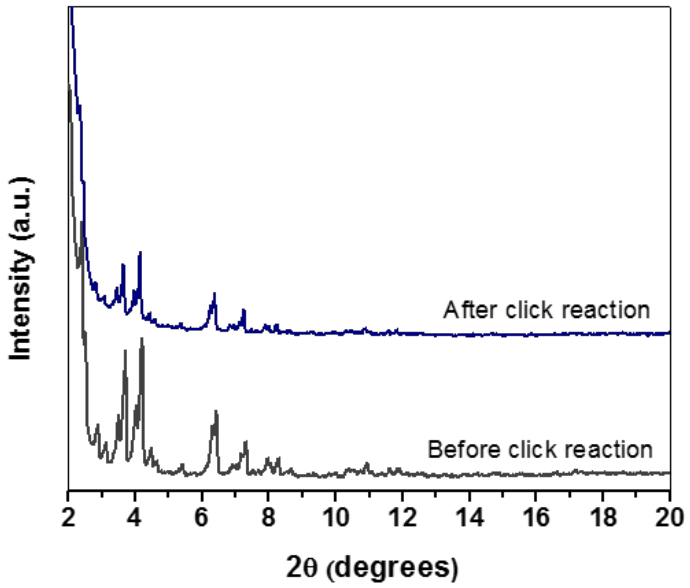

Figure 2.10 Comparison of PXRD patterns of before/after click reaction of methyl propiolate and azide-BTB exchanged PCN-333(Fe).

To investigate the potential utility of functionalized PCN-333, we further sought to expand our experimental design by introducing 4,4-difluoro-4-bora-3*a*,4*a*-diaza-*s*-indaene (BODIPY), a well-known fluorophore due to its excellent photochemical stability, tunable photophysical properties, and high quantum yield. Fluorescence measurements involve high sensitivity and rapid implementation, and thus fluorophores such as BODIPY derivatives can be widely employed in the MOF field. However, the incorporation of fluorophores in MOF as ligands would take substantial synthetic efforts while the anchorage of such compounds to a functionalized MOF through a postsynthetic approach is more practical.[44,68,69] To illustrate our concept, terminal alkyne functionalized BODIPY (**14**) was synthesized to perform a click reaction with azide-functionalized PCN-333(Fe). Although the IR spectrum suggests a successful click reaction on PCN-333(Fe), attempts to observe fluorescence from BODIPY-clicked PCN-333(Fe) were not successful due to the presence of Fe(III) which can quench the emission of BODIPY (Figure 2.11). To avoid the interference from the Fe(III) node, we chose colorless PCN-333(Sc) to show the click reaction more clearly.

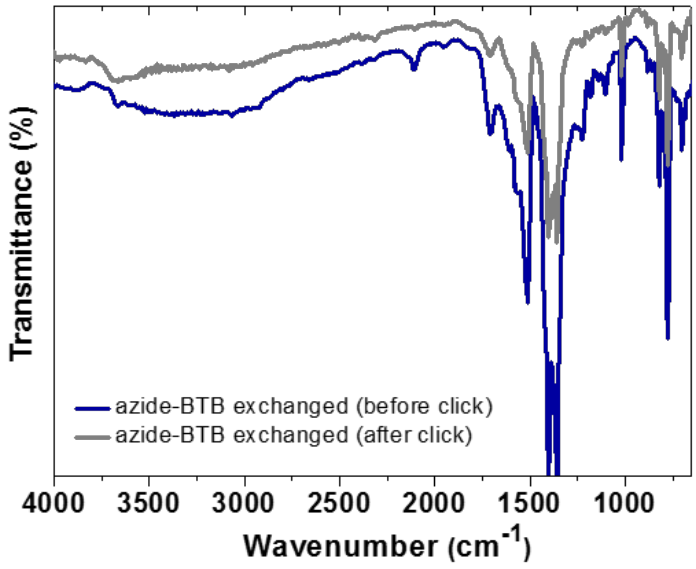

Figure 2.11 IR spectra of before/after click reaction of **14** and azide-BTB exchanged PCN-333(Fe)

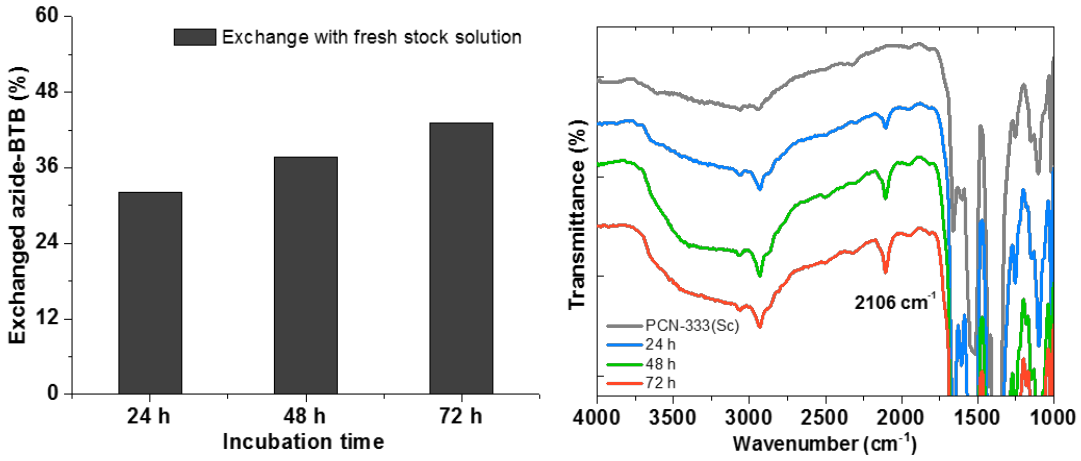

Figure 2.12 (left) Azide-BTB exchange ratio (%) in PCN-333(Sc) for different incubation times. (right) IR spectra of azide-BTB exchanged PCN-333(Sc) that having different ratios of azide-BTB.

The exchanged samples with different ratios of the azide group were prepared by changing the stock solution as previously found. The extent of azide-BTB exchange was determined by ^{1}H NMR spectroscopy upon digestion of samples (Figure 2.12). Considering carboxylates bind less strongly to Sc(III) than Fe(III), ligand exchange in PCN-333(Sc) should occur more easily. As observed in the exchanging process, ligand exchange in PCN-333(Sc) reached an equilibrium quickly because of the easier M–L bond dissociation (Figure 2.3f). However, the thermodynamic equilibrium of the exchange process was almost independent from M–L bond nature as we analyzed and a slightly lower extent of the exchange saturation point was observed in BTB exchange. Nonetheless, azide-functionalized BTB showed a comparable exchanged ratio in PCN-333(Sc) as in PCN-333(Fe).

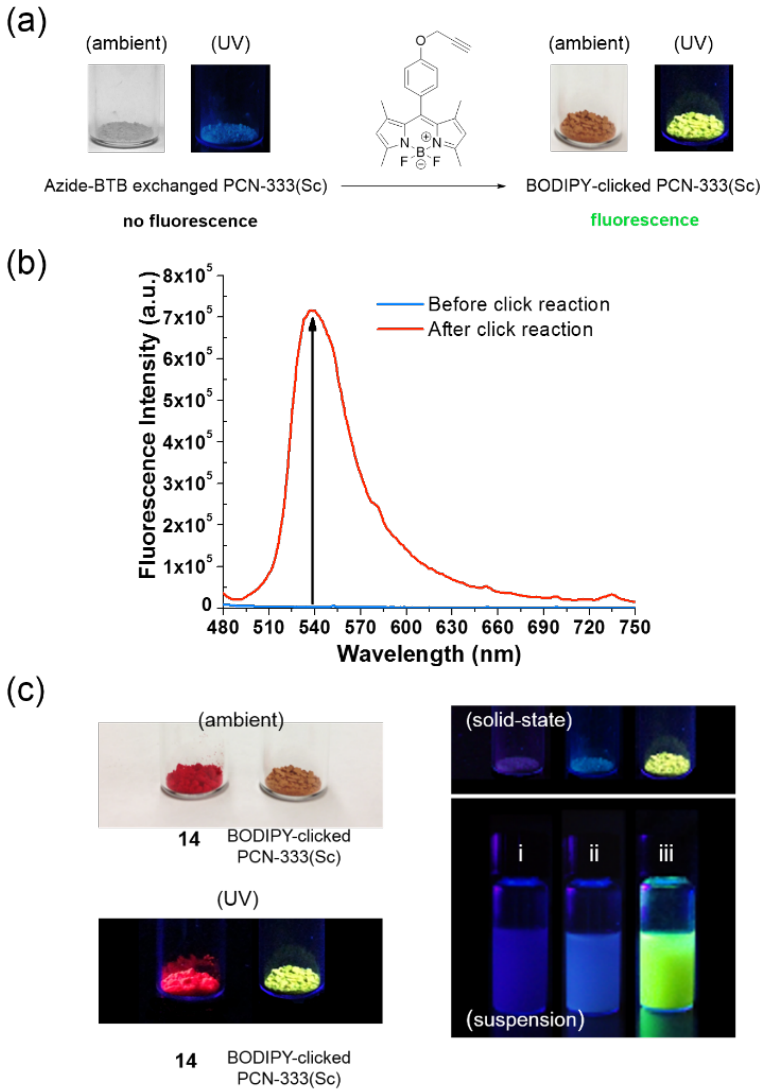

Figure 2.13 (a) Click reaction scheme performed on PCN-333(Sc) with BODIPY fluorophore. Photographs are before and after BODIPY introduction on PCN-333(Sc). (b) Solid-state fluorescence emission spectra of azide-BTB exchanged PCN-333(Sc) (blue) and BODIPY-clicked PCN-333(Sc) (red). λ_{ex} = 450 nm. (c) Comparison of solid-state **14** and BODIPY-clicked PCN-333(Sc) (left). Photographs of (i) pristine PCN-333(Sc), (ii) azide-BTB exchanged PCN-333(Sc), and (iii) BODIPY-clicked sample in both solid-state and suspension (right).

The click reaction of azide-functionalized PCN-333(Sc) and alkyne-BODIPY (**14**) was successfully performed with a catalytic amount of CuI in THF (65 °C, 21 h) (Figure 2.13a). To our delight, BODIPY-clicked PCN-333(Sc) showed strong

fluorescence in both suspension and solid-state. Notably, the emission of BODIPY-clicked PCN-333(Sc) in the solid state is green (λ = 550 nm; Figure 2.13b) suggesting that the clicked dye behaves as a monomeric dye, while dye aggregates (**14**) showed a red emission (Figure 2.13c). After close examination of the structure of PCN-333, it is very likely that the large pores provide enough space for clicked dyes to be spatially separated thereby emitting as single dye molecules. A click reaction on the samples containing different loading of azide groups showed that higher loading of azide groups resulted in a slight red shift in emission maxima (Figure 2.14).

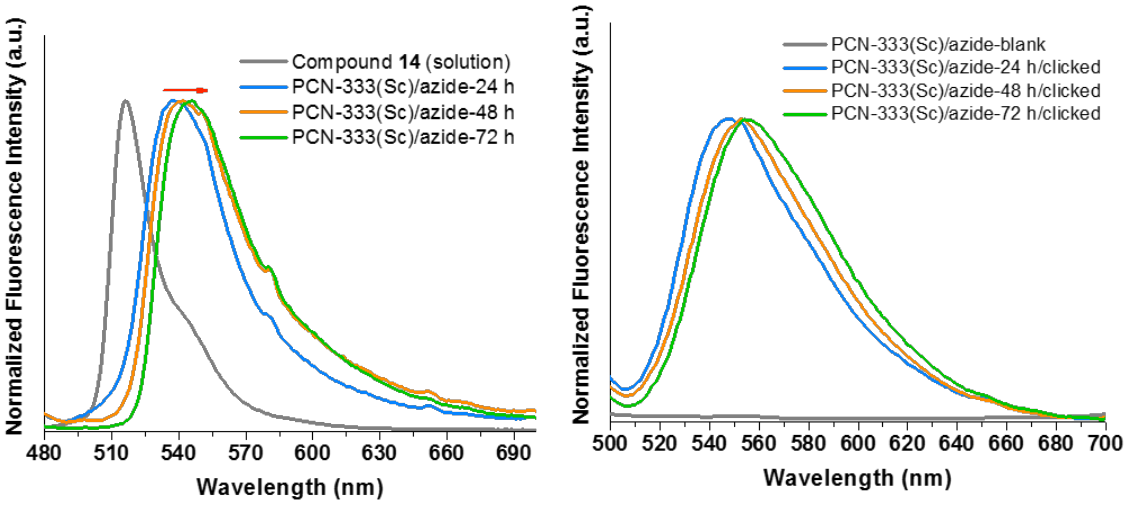

Figure 2.14 (left) Fluorescence emission spectra of azide-BTB exchanged PCN-333(Sc) and **14** clicked MOFs in acetone. λ_{ex} = 450 nm. (right) Solid-state fluorescence emission spectra of azide-BTB exchanged PCN-333(Sc) and **14** clicked MOFs. λ_{ex} = 450 nm.

2.4 Conclusions

In summary, a facile functionalization assisted by structural attributes of PCN-333 has been studied while maintaining the integrity of the parent MOF including ultralarge

pores, chemical robustness, and crystallinity. The foregoing results showed a promise that the extent of exchange can be tailored by varying temperature, concentration, or incubation time as potential applications may require. Furthermore, a variety of functional groups can be incorporated into PCN-333 via this strategy to covalently anchor guest species. Along this line, introduction of a secondary functionality was successfully performed via a click reaction with a BODIPY fluorophore. We anticipate the functionalized PCN-333 can serve as a stable platform for further chemistry to be explored in future applications.

3. DUAL EXCHANGE IN PCN-333: A FACILE STRATEGY TO CHEMICALLY ROBUST MESOPOROUS CHROMIUM METAL–ORGANIC FRAMEWORK WITH FUNCTIONAL GROUPS*

3.1 Introduction

As an emerging class of inorganic–organic hybrid materials, metal–organic frameworks (MOFs) have gained growing attention as advanced porous materials.[1] The unique combinations of organic/inorganic building blocks that compose these materials allow diverse functions leading to various applications.[23-25,70-76] Among many features of MOFs, mesoporosity is of great interest due to the prospect of hosting large guest molecules such as organometallic complexes, nanoparticles, and enzymes, creating diverse applications with MOFs.[10,28,77-79] Aside from such encapsulation within the large pores, molecular level design of organic ligands provides tailor-made structures and functionalities for targeted applications.[80-85]

It would be ideal if a mesoporous MOF could be directly synthesized from the ligand with a predesigned functionality. It has been shown, however, that in many cases this does not lead to a desired product due to the changes in molecular geometry of the ligand upon addition of functional group.[55,86] As a classic tactic for the aforementioned difficulty, postsynthetic exchange has greatly promoted the functionalization of MOFs.[42-46,48-53,55-58,61-63,66,87-92] However, most parent MOFs require that postsynthetic processes occur under mild conditions to maintain their integrity. Despite the advances of

---

*Reproduced with permission from Park, J.; Feng, D.; Zhou, H.–C., *J. Am. Chem. Soc.*, **2015**, *137*, 11801–11809. Copyright 2015 American Chemical Society.

postsynthetic exchange and solvent assisted linker exchange, introduction of various kinds of reactive functional groups is still challenging. Also, such methods usually involve labile metal–ligand (M–L) bonds in the MOF, suggesting a latent instability of the parent material. Therefore, the resulting product with postsynthetically inserted functional ligand still needs to overcome the stability issue.

With growing attention, MOFs have been utilized in various applications, including catalysis, sensing, biomedical imaging, as well as the areas of gas storage and separation.[23-25,70-73,75,76] As MOF applications have gained broader impacts in materials science, it gradually requires even more sophisticated design of materials encompassing their compatible stability in targeted applications (i.e., aqueous stability for biomedical applications), as well as pore size and shape. As a result, demands for framework robustness have increased in pursuit of applicability of MOF in more complex systems.[32-34,41,93-103] However, most reported mesoporous MOFs suffer from weak chemical stability, mainly arising from the labile M–L bond in those frameworks.[26,29-31,38] Also, reticular chemistry which usually involves the extension of linkers to obtain larger pores tends to weaken the stability of frameworks.[27,104,105] Therefore, extremely inert M–L bond is highly encouraged to increase the stability of MOFs with mesopores.

On the basis of literature reporting, Cr(III) based clusters might be strong candidates to serve as an inorganic node to support mesoporous MOFs as compared to other trivalent metal species due to the kinetic inertness of Cr(III).[93,106-109] However, such inert Cr–carboxylate bonding also impedes the direct synthesis of chromium MOFs (Cr-MOFs), resulting in few Cr-MOF examples.[93,106,108,109] Although postsynthetic metal

metathesis has led to obtaining MOFs that cannot be synthesized directly,[39,66,110-126] there is only one successful example where almost complete exchange, via a microporous Cr(II)-MOF intermediate, has yielded a Cr(III) MOF.[127] Moreover, the successful synthesis of Cr-MOFs typically involves water as a solvent, where solubility of larger organic ligands required to achieve larger pores can be rather poor.[93,106-109] In particular, mesoporous structures are commonly limited to specific topologies, requiring a subtle control of synthesis to have the expected configuration of both inorganic and organic building blocks,[35,108] which often limits the variation of synthetic conditions in Cr-MOF system.

In addition to the synthetic difficulties, the functionalization of Cr-MOFs has been a great challenge. For instance, functionalization through the ligand design in one of the most famous mesoporous MOFs, MIL-101(Cr) (MIL stands for Matérial Institut Lavoisier), has been limited to a small subset of functional groups, such as −Br, $-NO_2$, and $-SO_3H$, while relatively practical functional groups in organic reactions (e.g., −OH, $-NH_2$) on the ligands often undergo decomposition under the hydrothermal condition (~200 °C) required for synthesis.[128] Although postsynthetic modification could somewhat alleviate such difficulties, the conflict between the harsh reaction conditions and inherent stability of the parent MOF still hampers the diversification of functionalization. In comparison, postsynthetic ligand exchange may be more suitable to diversify the library of functionalized Cr-MOFs. However, the inertness of Cr-MOF also impedes efficient postsynthetic ligand exchange processes.[63,88]

Herein we present a stepwise exchange strategy of both ligands and metals, namely dual exchange in PCN-333(Fe) for the preparation of functionalized PCN-333(Cr) (PCN stands for Porous Coordination Network). After the dual exchange process, functionalized PCN-333(Cr) shows well preserved crystallinity, porosity, as well as enhanced chemical stability. Understanding of chemical dynamics along with the dual exchange in PCN-333(Fe) may allow for a generalized route to functionalized Cr-MOFs, which will exhibit a maintained structural integrity of parent MOF with desired functional groups and enhanced stability. Furthermore, having studied the incorporation of various functional groups in PCN-333(Fe), dual exchange shows a great potential to employ many different functional groups in the highly stable Cr-MOF platform.

3.2 Experimental section

Instrumentation

Nuclear magnetic resonance (NMR) spectra were recorded on Varian Inova 500 spectrometer unless otherwise noted. Powder X-ray diffraction (PXRD) was carried out on a Bruker D8-Focus Bragg–Brentano X-ray powder diffractometer equipped with a Cu sealed tube (λ = 1.54178) at 40 kV and 40 mA. Fourier transform infrared (FT-IR) measurements were performed on a Shimadzu IR Affinity-1 spectrometer. Scanning electron microscope (SEM) was performed on QUANTA 450 FEG and energy dispersive X-ray spectroscopy (EDS) was carried out by X-Max20 with Oxford EDS system equipped with X-ray mapping. N_2 adsorption–desorption isotherms at 77 K were measured by using a Micrometritics ASAP 2420 system. A high-purity grade (99.999%) of gas was used throughout the sorption experiments. Sample was activated by solvent

exchange (in several cycles using fresh acetone and hexanes), followed by degassing at elevated temperature (150 °C) for 2 h.

Synthesis

Synthesis of PCN-333(Fe). H_3TATB (60 mg), anhydrous $FeCl_3$ (60 mg), and trifluoroacetic acid (0.6 mL) were dissolved in 10 mL DEF. The mixture was heated in 150 °C oven for 12 h until a brown precipitate formed. The resulting brown precipitate was centrifuged and washed with fresh DMF five times.

Synthesis of PCN-333(Sc). H_3TATB (80 mg) and $ScCl_3 \cdot 6H_2O$ (200 mg) were dissolved in 10 mL DMF. The mixture was heated in 150 °C oven for 2 h until a white precipitate formed. The resulting white precipitate was centrifuged and washed with fresh DMF five times.

General procedure for ligand exchange of PCN-333(Fe). First, as-synthesized PCN-333(Fe) (ca. 50 mg) was thoroughly washed with hot DMF and the isolated sample was then incubated with a stock solution of N_3–BTB (50 mg in 10 mL of DMF) at 85 °C for 12 h.

General procedure for the preparation of PCN-333(Cr). Approximately 50 mg of as synthesized PCN-333(M) sample is initially immersed in the $CrCl_3 \cdot 6H_2O$ stock solution (200 mg in 10 mL of DMF) in 20 mL vial in a 150 °C oil bath. After 30 min of first incubation, the solution was decanted after centrifugation and additional 30 min of reaction was performed with new $CrCl_3 \cdot 6H_2O$ stock solution. Resulting product was then thoroughly washed with DMF five times. (Note: To preserve the morphology of the exchanged product, the reaction was not stirred, but refluxed. However, we observed the

exchange underwent slightly faster with stirring to yield similar exchanged metal ratio. In addition, according to our control experiment (pure $CrCl_3 \cdot 6H_2O$ in DMF), when heating at 150 °C is longer than 3 h, green precipitates gradually formed. Therefore, it is suggested not to leave the exchange reaction in mother solution too long at high temperature, to prevent possible formation of insoluble Cr formates or other unknown species, which are likely to affect porosity and crystallinity of the product.)

General procedure for metal metathesis of N_3–PCN-333(Fe). Approximately 10 mg of N_3–PCN-333(Fe) samples are initially immersed in the $CrCl_3 \cdot 6H_2O$ stock solution (40 mg in 2 mL of DMF) at 150 °C oven. After 30 min of first incubation, the solution was decanted after centrifugation and additional 30 min of reaction was performed with new $CrCl_3 \cdot 6H_2O$ stock solution. Resulting product was then thoroughly washed with DMF five times.

Sample activation procedure

Thoroughly washed samples underwent solvent exchange with acetone followed by hexanes at least five times, respectively and dried in a pre-heated 85 °C oven for 30 min. Resulting powder was then activated for BET measurement at 150 °C for 2 h.

MOF digestion

Approximately 10 mg of sample was digested with 37% HCl, refluxed overnight, and washed with water until a neutral pH was reached. DMSO-d_6 (0.5 mL) was added to dissolve the ligands. The ^{1}H NMR spectrum (500 MHz) was collected at room temperature (~21 °C).

Supernatant analysis

Upon completion of treatment, the supernatant was removed to examine TATB or N_3–BTB released from the parent MOF. The aliquot of supernatant was filtered through a syringe filter to exclude the possible presence of MOF crystals remaining and the ligands in supernatant were recovered by acidification with few drops of 1 M HCl, followed by washing with water. The resulting precipitates were dried and analyzed by ^{1}H NMR spectroscopy.

Click reaction

TEPP (50 mg) was added to a mixture of N_3–PCN-333(Cr) (30 mg) and CuI (5 mg) in DMF (7 mL) in a round-bottom flask. The reaction mixture was stirred at 60 °C for 28 h. The resulting precipitate was collected by centrifugation, washed thoroughly with DMF followed by acetone and hexanes, and dried to afford a dark purple solid in quantitative yield.

3.3 Results and discussion

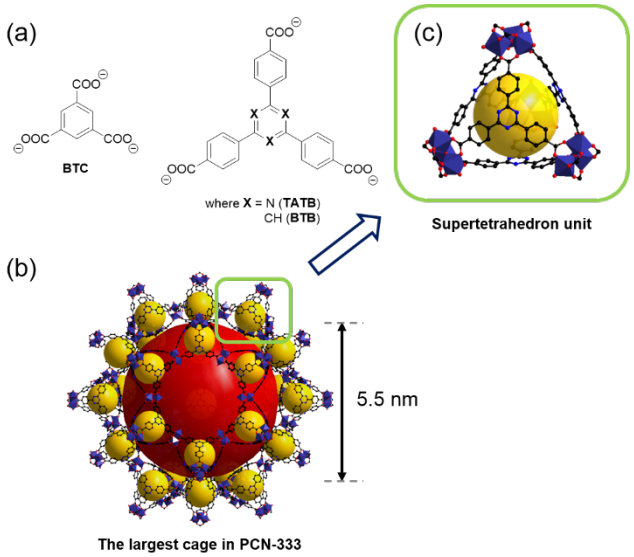

Figure 3.1 (a) Ligands in MIL-100 (BTC) and PCN-333 (TATB). (b) The largest cage in PCN-333. (c) Supertetrahedron in PCN-333.

PCN-333: An ideal scaffold for functionalizable Cr-MOF with mesoporosity

Our group recently reported a mesoporous MOF, PCN-333,[40] constructed from trivalent metal ions and isoreticular structure to MIL-100.[93] Due to the larger size of composing ligand 4,4′,4″-*s*-triazine-2,4,6-triyl-tribenzoate (TATB), extended version of benzene-1,3,5-tricarboxylate (BTC), PCN-333 exhibits larger pores (~5.5 nm) than that of MIL-100 (~2.9 nm), which allow the incorporation larger guest species as well as faster diffusion and provide sufficient room for chemical reactions in the mesopores (Figure 3.1). Having utilized the structural support of PCN-333, we recently studied a facile route to functionalize PCN-333(M) [M = Fe(III), Sc(III)] via postsynthetic ligand exchange.[129] As a result of the ligand exchange, a variety of reactive functional groups were introduced into PCN-333 to covalently anchor the guest molecules. Despite the successful

introduction of various functional groups into PCN-333, however, its innate stability at the expense of the extended ligand to achieve larger pore still remains a challenge for its utilization in harsh chemical conditions for MOFs (e.g., water) due to the relative lability of the Fe(III)– or Sc(III)–carboxylate bonds in aqueous environment. Having reviewed the reported stability of Cr-MOFs, we conceived that PCN-333(Cr) with covalent anchors might serve as a better platform for the utilizations in harsh environment. However, a direct synthesis of PCN-333(Cr) is not trivial due to the conflict between the hydrothermal synthetic condition required for the synthesis of Cr-MOFs and the poor solubility of TATB in water. Moreover, even if PCN-333(Cr) was obtained, it would be challenging to introduce functional group into the framework through the postsynthetic ligand exchange, because the kinetic inertness of Cr(III) prevents an effective ligand exchange process. Therefore, a stepwise exchange was considered to obtain functionalized PCN-333(Cr).

Optimization for metal metathesis in PCN-333

Having determined that a functionalizable PCN-333(Cr) might serve as a useful platform by providing exceptional stability and diverse functionality with large room for chemical reactions within the pores, we designed a procedure to achieve the targeted product, namely dual exchange. Possible routes to functionalized PCN-333(Cr) via dual exchange were conceived as two main schemes as shown in Scheme 3.1: (1) Metal exchange followed by ligand exchange and (2) Ligand exchange followed by metal exchange.

Prior to examining a better strategy to obtain functionalized PCN-333(Cr), PCN-333(Sc) and PCN-333(Fe) were tested for a Cr(III) metathesis to choose the most suitable

base MOF for successful dual exchange. PCN-333 was synthesized as previously reported. Because Cr(III) salts often yield insoluble formates due to DMF decomposition with long reaction time at high temperature, the reaction time was limited to preserve crystallinity and porosity while maintaining a high metal exchange ratio. After optimization for the reaction time, the following Cr(III) metathesis in PCN-333(M) was performed for 1 h by replacement of $CrCl_3 \cdot 6H_2O$ stock solution in DMF after the first 30 min of reaction.

To investigate an optimal exchange reaction temperature, first, PCN-333(Sc) and PCN-333(Fe) were incubated for 1 h (by changing stock solution after first 30 min) in Cr(III) stock solution at 85 and 150 °C in preheated ovens. Interestingly, both PCN-333(Sc) and PCN-333(Fe) showed no apparent color changes upon metathesis at 85 °C (Figure 3.2b,c). Energy-dispersive X-ray (EDX) spectra revealed low exchange ratios of both samples (37.0% for PCN-333(Sc/Cr) and 23.0% for PCN-333(Fe/Cr)), and especially poor powder X-ray diffraction (PXRD) patterns of PCN-333(Sc) (Figure 3.2). Notably, PCN-333(Sc) showed slightly higher Cr(III) exchange ratio than that of PCN-333(Fe) at 85 °C, while showing no PXRD pattern, which suggests its lability, whereas at 150 °C, both samples generally showed much higher Cr(III) exchange ratios than those at lower temperature [64.8% for PCN-333(Sc/Cr) and 99.8% for PCN-333(Fe/Cr)].

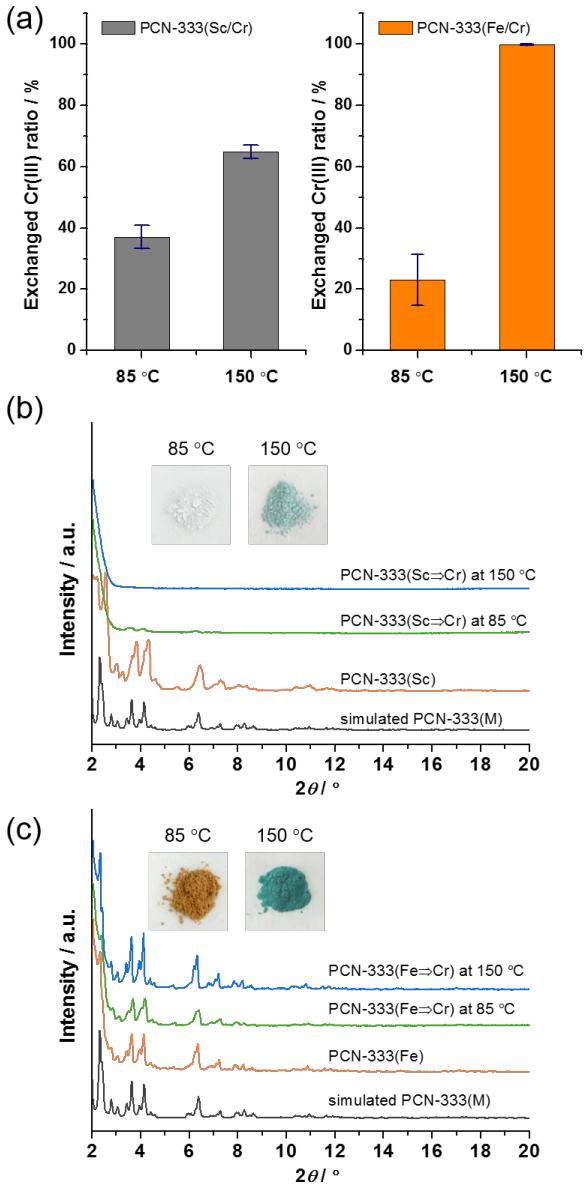

Figure 3.2 (a) Exchanged Cr(III) ratios in PCN-333(Sc) (left) and PCN-333(Fe) (right) after metal metathesis at different temperatures for 1 h. (b-c) Photographs and PXRD patterns of PCN-333(Sc) (b) and PCN-333(Fe) (c) after metal metathesis at different temperatures for 1 h.

In particular, Cr(III) metathesis from PCN-333(Fe) showed near complete exchange along with well-maintained crystallinity and porosity, which were confirmed by

PXRD (Figure 3.2c) and N_2 sorption at 77 K, respectively (Figure 3.3). On the other hand, the diffraction of PCN-333(Sc) almost completely disappeared after the Cr(III) metathesis. It is reasoned that these results are due to the discrepancy between dissociation rates of leaving metal species in the framework and incoming metal species from the solution. For instance, in our previous study of ligand exchange in PCN-333, the successful ligand exchange was carried out at low temperature (85 °C), which suggests it gives enough energy to overcome the energy barrier of Sc(III)–carboxylate or Fe(III)–carboxylate bond dissociations within the framework. Closely looking at the metal metathesis process, the M–L bond dissociation is required for both incoming metal complex and metals in the parent MOF to accomplish the overall exchange process. Even though the temperature is sufficient enough for the ligand dissociation in the framework, much slower ligand dissociation in the incoming Cr(III) complex can still be a rate limiting step. Therefore, the Cr(III) metathesis at low temperature was not successful. On the other hand, when the given energy is enough for breaking Cr(III)–X (i.e., Cl^-) bond from Cr(III) salts and following association with the open carboxylates in the framework after Fe(III) dissociation for successful exchange, Cr(III) exchange reached to higher exchange ratio in both cases (Figure 3.2a). When it comes to the retention of framework structure, however, the metathesis in PCN-333(Fe) was superior to PCN-333(Sc), presumably due to the relative robustness of PCN-333(Fe) resulting from the slower Fe(III)–carboxylate dissociation rate than that of PCN-333(Sc) allowing compatible exchange environment with Cr(III) association. Particularly, in the metal metathesis of labile PCN-333(Sc) platform, the framework would undergo significant destruction by free Cr(III) and

decomposed reactive species from DMF before obvious metal metathesis happened.[127] After discovering the previous result, PCN-333(Fe) was chosen as a platform for studying the dual exchange.

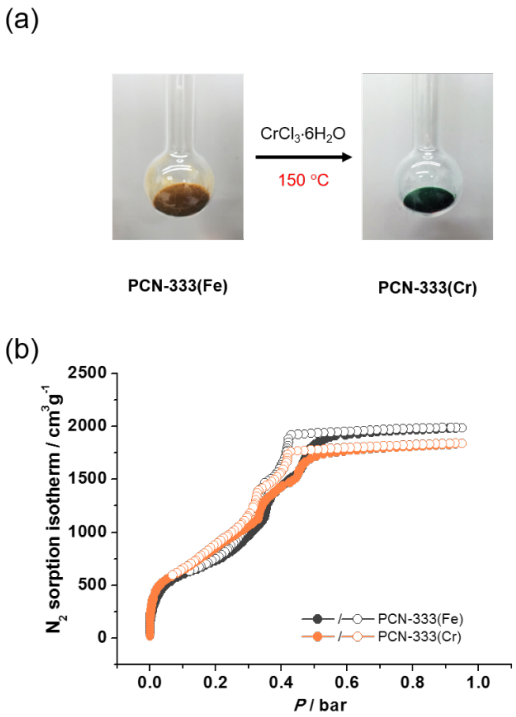

Figure 3.3 (a) Photographs of PCN-333(Fe) and PCN-333(Cr) exchanged at 150 °C. (b) N_2 sorption isotherm of PCN-333(Fe) and PCN-333(Cr) at 77 K.

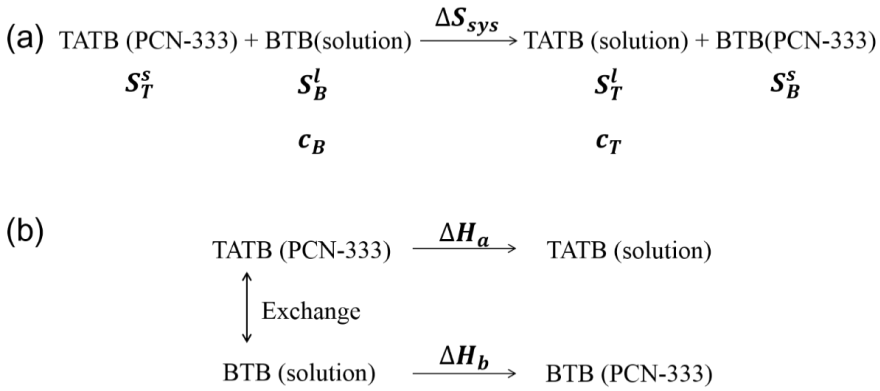

Figure 3.4 (a) Entropy change and (b) enthalpy change of the system during the ligand exchange.

Analysis of dual exchange

Following up on our previous study, exploring the chemical dynamics of ligand exchange in PCN-333,[129] we further sought to expand our observations and rationalizations focused on changes of entropy and enthalpy during the dual exchange. As was discussed in the previous study, the entropy change of the system (ΔS_{sys}), comprising a solid-state MOF and exchanging solution during the ligand exchange, was assumed to be largely dependent on ΔS in solution, as ΔS in the solid state MOF may be negligible. Thus, the ligand exchange process in PCN-333 was driven by a drastic entropy increase ($\Delta S_{sys}{}^{LE} > 0$) upon the provision of excess amount of the exchanging ligands (Figure 3.4). Similarly, the entropy change of the system during the metal metathesis ($\Delta S_{sys}{}^{MM}$) follows the same concept (Figure 3.5); thus, it yields a positive $\Delta S_{sys}{}^{MM}$ due to the excess input of Cr(III) in solution to replace Fe(III) in the framework. In S_{sys} standpoint, therefore, both ligand exchange and metal metathesis should have entropy contributions for the desired exchanges from the excess of exchanging entries.

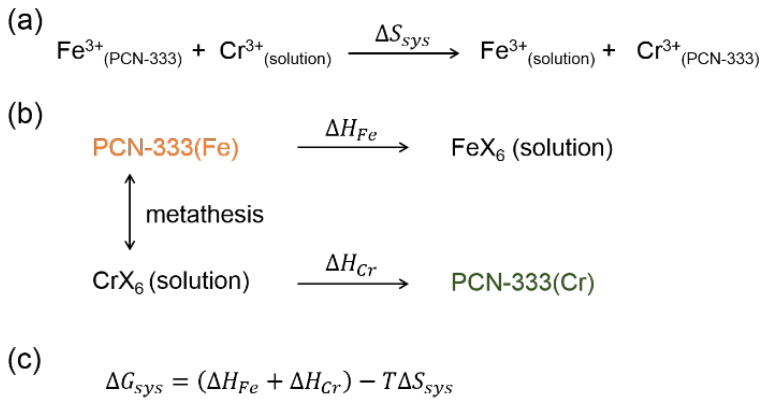

Figure 3.5 (a) Entropy and (b) enthalpy change of system during the metal metathesis. (c) Gibbs free energy of system during the metal metathesis in PCN-333.

When it comes to the enthalpy analysis of the ligand exchange process in PCN-333, as the degree of exchange increases the enthalpy of the system (H_{sys}) also increases ($\Delta H_{sys} > 0$) due to the insertion of BTB (1,3,5-benzenetribenzoate) derivatives with unfavored conformation in the framework (Figure 3.6). For this reason, although the large ΔS_{sys} at the early stage of ligand exchange could drive the exchange reaction forward, the system establishes an equilibrium with a certain ratio of ligand exchange.

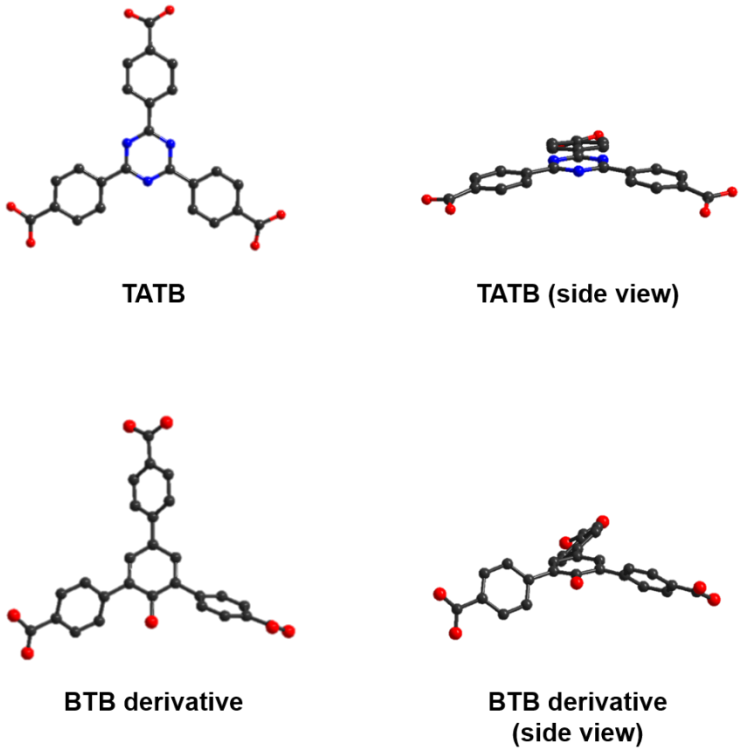

Figure 3.6 Structures of TATB and BTB derivative (OH-BTB). Top view (left) and side view (right) showing preferred non-planarity of BTB derivative.

However, metal metathesis between Fe(III) and Cr(III) accompanies the changes in M–L bond nature, comprising the framework, whereas the bond nature in the ligand exchange remains the same as Fe(III)–L bond (L represents carboxylate) in the

framework. Meanwhile, metal metathesis also involves changes of enthalpy in solution. For example, Fe(III) ions, coming out from the framework replace Cr(III) in the provided CrX_6 complex (X = Cl^-, DMF), resulting in FeX_6 species in solution. Consequently, there are two processes involving enthalpy changes of the system: (1) ΔH_{Fe}, corresponding to the enthalpy change of Fe(III) from the MOF to the solution; (2) ΔH_{Cr} corresponding to the enthalpy change of Cr(III) species from solution to the MOF. Thus, the enthalpy change of the system can be represented as $\Delta H_{sys} = \Delta H_{Fe} + \Delta H_{Cr}$.

Understanding of ΔH_{sys} during metal metathesis can be interpreted by focusing on electrostatic interaction and orbital interaction upon the exchange event. First, the Cr(III) has a smaller ionic radius than that of high spin Fe(III), leading to a larger Z/r value.[130] Considering carboxylate (L) is also a harder Lewis base compared to ligands, X, when Cr(III) coordinates to the carboxylates in the framework, the electrostatic interaction becomes stronger, providing larger enthalpy change upon metathesis compared to Fe(III).[131]

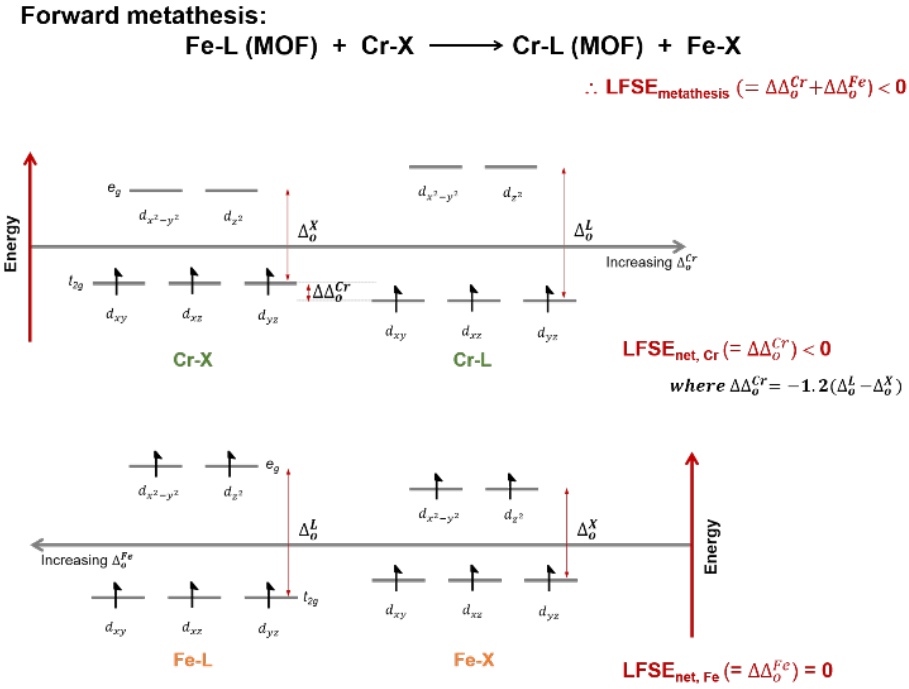

Figure 3.7 Analysis of the orbital interaction contribution to ΔH_{sys} using ligand field theory with a simplified coordination environment (O_h) for the metal metathesis process in PCN-333.

Aside from the electrostatic interaction, the orbital interaction also changes for each metal species along with the metathesis. To compare the changes in orbital interaction, which contributes to ΔH_{sys}, ligand field theory (LFT) was applied to simplify the given scenario. Although the actual coordination environment for the M(III) (M = Cr or Fe) in the framework gives rise to a C_{4v} symmetry due to the two different axial ligands and that for MX_6 species in the solution may even vary, herein we assumed O_h symmetry for both cases to simplify the analysis of the contributions from the coordinating ligands to ΔH_{sys}.

Considering ligands X in solution are relatively weaker field ligands than carboxylate (L),[132] and the metal-carboxylate (M–L) bonds are dominant in the

framework, the changes in the coordinating ligands upon metathesis will have impacts on ΔH_{sys}. For example, when Cr(III) is exchanged from solution into the framework, the *d* orbital splitting energy changes from $\Delta_O{}^X$ to $\Delta_O{}^L$ (Figure 3.7). As Cr(III) has d^3 configuration, such coordination environment change gives out a net ligand field stabilization energy (LFSE) of $-1.2(\Delta_O{}^L - \Delta_O{}^X)$. Therefore, from the Cr(III) standpoint, as $\Delta_O{}^L$ is larger, the system gets more stabilized. On the other hand, because Fe(III) adopts high spin d^5 configuration with weak field ligands, the LFSE is canceled out from its two electrons in e_g orbitals, resulting in no stabilization impacts from the exchange event. Overall, the system gets more stabilized after metal metathesis from the orbital interaction aspect. In short, while both electrostatic interaction and orbital interaction go through the changes during the metal metathesis, the absolute value of ΔH_{Cr} is more likely to be larger than that of ΔH_{Fe}, making the ΔH_{sys} negative and the overall metal metathesis from PCN-333(Fe) to PCN-333(Cr) an exothermic process. Thus, the metal metathesis from PCN-333(Fe) to PCN-333(Cr) can be considered as a both entropically and enthalpically favored process.

According to the findings in the previous section, the metal metathesis is optimized at high temperatures (150 °C). Interestingly, we found the metatheses of from Sc(III) to Cr(III) and Fe(III) to Cr(III) at 85 °C showed very low exchange ratios, suggesting indeed Cr(III)–X bond has to be sufficiently activated by high temperature. Such high temperature not only provided sufficient energy for Cr(III)–X bond dissociation, but also allowed a short reaction time, avoiding a long exposure of MOF in the reactive environment which further guarantees the framework intactness. Moreover, owing to the

high reaction temperature, the entropy contribution to ΔG_{sys} is magnified from the $T\Delta S$ term, which pushes the exchange more forward. In particular, our optimized metathesis involves the exchange of fresh the $CrCl_3 \cdot 6H_2O$ solution after first 30 min of exchange; and thus this can remove the Fe(III) in the solution to facilitate an entropy driven process, further driving the reaction forward to the almost fully exchanged PCN-333(Cr).

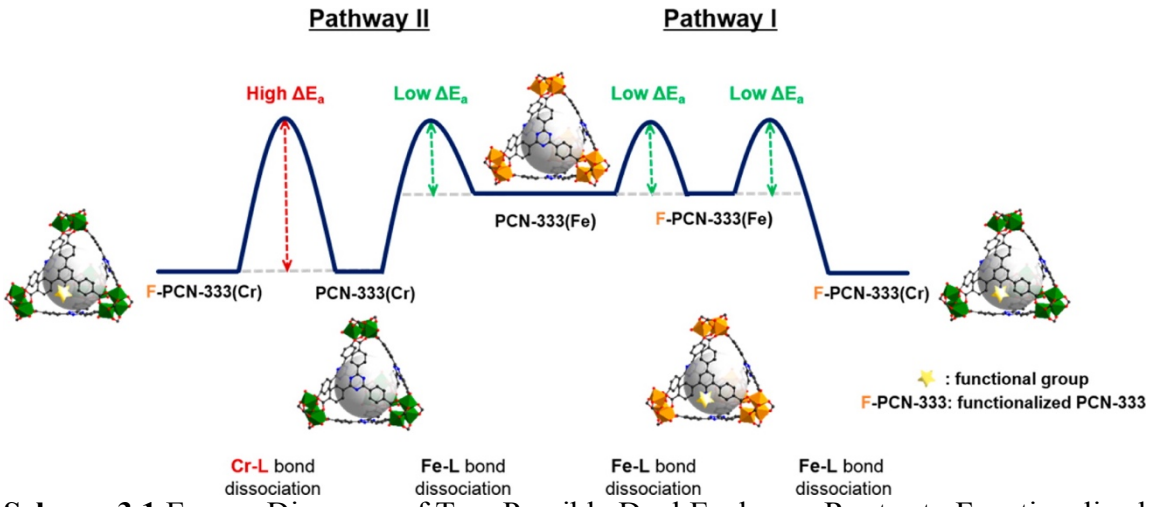

Scheme 3.1 Energy Diagrams of Two Possible Dual Exchange Routes to Functionalized PCN-333(Cr).

Functionalization of PCN-333(Cr) through dual exchange

Considering the previous results, schematic energy diagrams representing possible dual exchange pathways are summarized in Scheme 3.1. Pathway 1 (**path 1**) shows a case where the dual exchange to get the functionalized PCN-333(Cr) in an order of ligand exchange followed by metal metathesis. As shown in **path 1**, each step involves kinetically and thermodynamically favored process as analyzed the given temperature was sufficient to drive the reactions forward. From the framework standpoint, **path 1** involves

a dissociation of Fe-carboxylate bonds at each step, which takes less energy than breaking Cr–carboxylate bond.

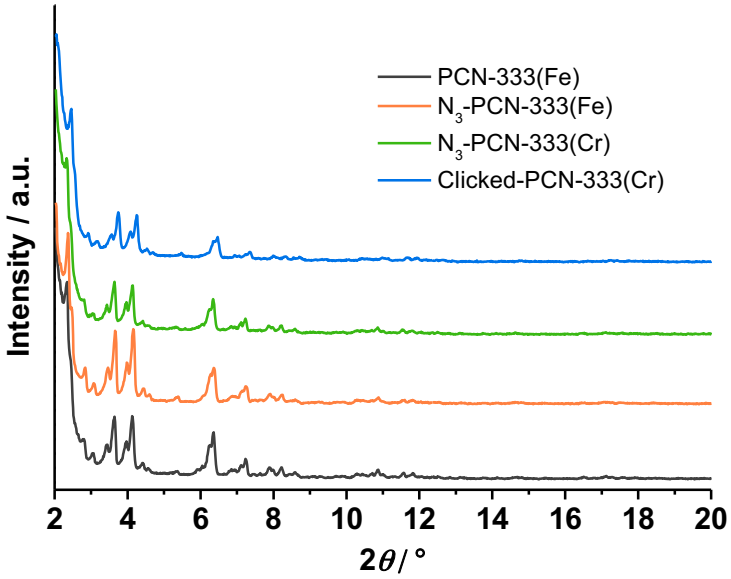

Figure 3.8 PXRD patterns of as-synthesized materials.

On the other hand, **path 2,** in which the functionalization (ligand exchange) is done after Cr-MOF formation (metal metathesis), requires a large amount of energy to overcome the barrier of Cr–carboxylate bond dissociation for the ligand exchange step. Therefore, to obtain functionalized PCN-333(Cr), thermodynamically favored **path 1** was chosen for the double exchange in the following experiments. However, to confirm our hypothesis, **path 2** was also examined for its feasibility for dual exchange. Having prepared PCN-333(Cr) by the optimized condition as previously described, first a ligand exchange in PCN-333(Cr) was tested via path 2 as shown in Scheme 3.1. For an incoming ligand, one of BTB derivatives having an azide group (N_3–BTB; shown in Figure 3.9a) was chosen as a model inserting ligand because of its versatile utilities in many

applications and allowance of click reaction after successful implantation of functional group, so as to confirm the feasibility of a secondary chemical reaction onto dual exchanged PCN-333(Cr). The ligand exchange followed the optimized condition (85 °C, 12 h) from our previous study wherein the exchange condition guarantees the crystallinity and porosity.[129] As a result of dual exchange following the **path 2**, though crystallinity of PCN-333(Cr) was retained after going through the ligand exchange, ^{1}H NMR analysis of supernatant of reaction revealed that no TATB released from PCN-333(Cr) under the given condition, as expected.

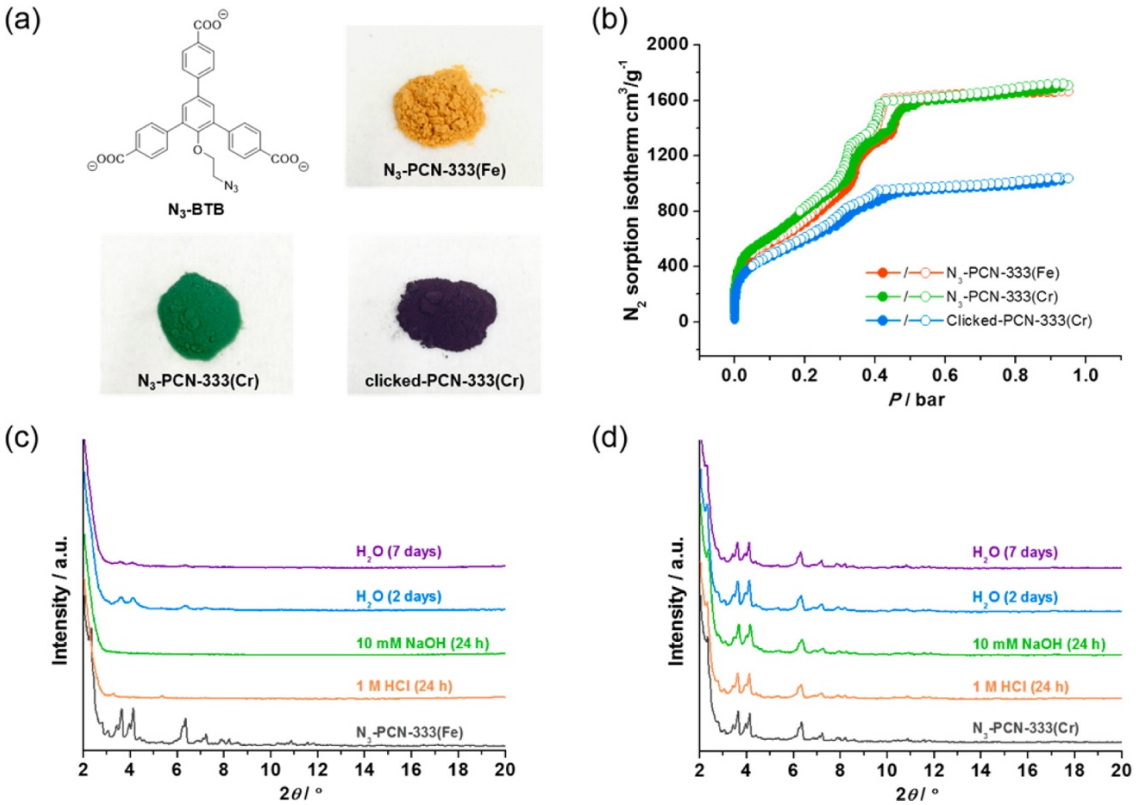

Figure 3.9 (a) N_3–BTB used for ligand exchange and photographs of N_3–PCN-333(Fe), N_3–PCN-333(Cr), and N_3–PCN-333(Cr) after click reaction. (b) N_2 sorption isotherm of N_3–PCN-333(Fe), N_3–PCN-333(Cr), and N_3–PCN-333(Cr) after click reaction. (c) PXRD patterns of N_3–PCN-333(Fe) and (d) N_3–PCN-333(Cr) after different treatments.

Having demonstrated **path 2** is not suitable to realize dual exchange on the PCN-333(Fe) platform, we then sought to optimize **path 1** to obtain the dual exchanged product. Again the ligand exchange from TATB to N_3–BTB in PCN-333(Fe) was performed as previously stated. ^{1}H NMR study confirmed that the ligand exchange ratio in PCN-333(Fe) showed a similar N_3–BTB ratio to the previous report (~30%). Also, the N_3–BTB inserted PCN-333(Fe) (N_3–PCN-333(Fe)) showed well retained crystallinity and porosity (Figures 3.8 and 3.9). In addition, a characteristic stretching band of the azide group at 2106 cm^{-1} was observed from infrared (IR) spectrum of N_3–PCN-333(Fe). As a second step of dual exchange in **path 1**, the previously optimized condition for metal metathesis was then applied to obtain the azide functionalized PCN-333(Cr) (N_3–PCN-333(Cr)). After 1 h of Cr(III) metathesis, the dual exchanged sample was prepared accompanying with an obvious color change from bright yellow to green (Figure 3.9a). EDX results revealed that ~97% of Fe(III) in N_3–PCN-333(Fe) was exchanged to Cr(III) without compromising its crystallinity (Figure 3.9 and Table 3.1).

Table 3.1 Summary of dual exchange

Entry	N_2 uptake (cm^3/g)[a]	Pore volume (cm^3/g)	Exchanged Cr (%)[b]
PCN-333(Fe)	1985	3.07	n/a
PCN-333(Cr)	1838	2.84	~99
N_3-PCN-333(Fe)	1663	2.57	n/a
N_3-PCN-333(Cr)	1707	2.64	~97
Clicked-PCN-333(Cr)	1033	1.60	n/a

[a]N_2 sorption was measured at 77 K. [b]Based on EDX results.

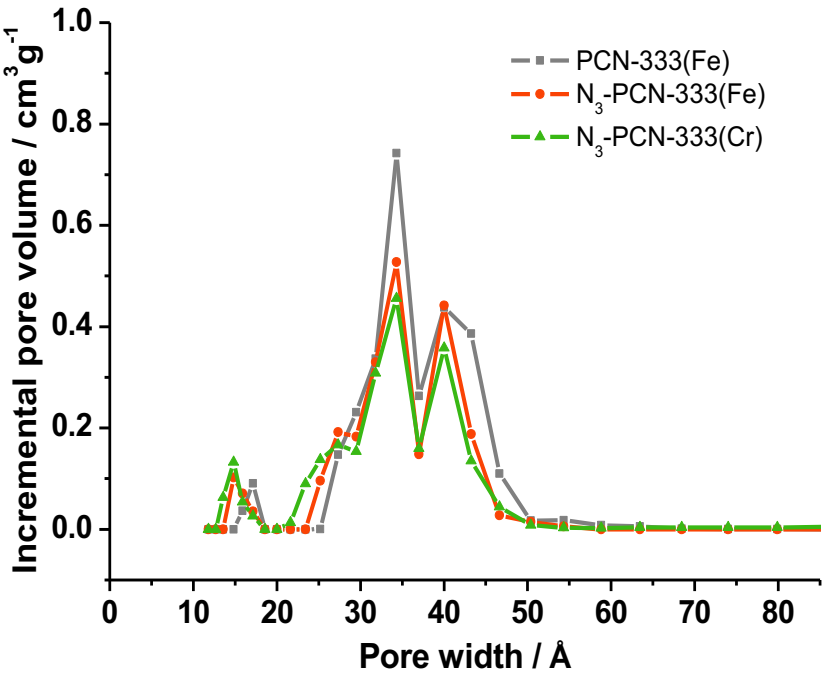

Figure 3.10 DFT pore size distribution of samples obtained from N_2 sorption isotherm at 77 K.

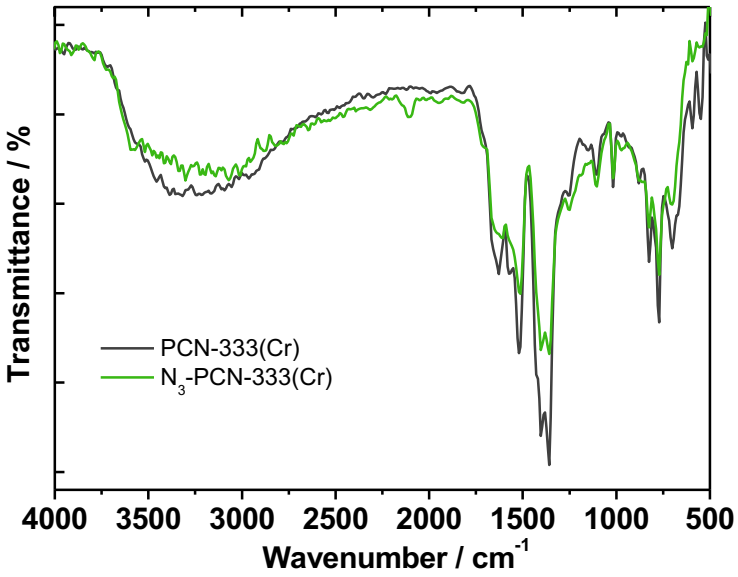

Figure 3.11 IR spectra of double exchanged N_3-PCN-333(Cr).

Additionally, ^{1}H NMR analysis of supernatant of Cr(III) exchange reaction showed no detectable TATB or N_3–BTB ligands leaching out from the parent MOF, which further suggests there is minimal destruction of framework as supported by PXRD. As shown in Figure 3.9b, the porosity of N_3–PCN-333(Cr) was almost perfectly retained compared to its starting material, N_3–PCN-333(Fe). According to DFT pore size distribution, a reduced pore size of the smallest pore in both N_3–PCN-333(Fe) and N_3–PCN-333(Cr) was observed (Figure 3.10). This suggests the presence of functional group on the N_3–BTB affected the smallest cage most. However, as we analyzed in the previous study, the middle-sized cages (~4.5 nm) and the largest cages (~5.5 nm) remained less affected due to their extralarge size. Thus, dual exchanged PCN-333(Cr) also showed well

preserved characteristics of mesoporosity after going through a sequential exchange of ligands and metals. IR spectrum of N_3–PCN-333(Cr) clearly showed the azide stretching band, which further confirms the undamaged functional group after the dual exchange process (Figure 3.11). In addition, after the metal metathesis from Fe(III) to inert Cr(III) of azide functionalized PCN-333, significantly enhanced stability than that of the parent material was observed. For instance, PXRD patterns showed that crystallinity of N_3–PCN-333(Cr) remains intact after submersion in deionized water for 7 days whereas that of N_3–PCN-333(Fe) showed gradually decreasing crystallinity upon the identical treatment. Moreover, N_3–PCN-333(Cr) showed well maintained crystallinity in harsh conditions, such as in 1 M HCl and 10 mM NaOH after treatment for 24 h, while N_3–PCN-333(Fe) was dissolved under the same conditions (Figures 3.9c,d). These findings suggest that dual exchange can be used as a means to prepare functionalized Cr-MOF. Expectedly, our results show successful dual exchange process via **path 1**, but not via **path 2**. This may seem different from a work by Cohen and co-workers that has studied a similar concept, called tandem exchange,[49] which is the only example involving both ligand exchange and metal metathesis within one framework yet to our best knowledge. Tandem exchange allowed for the preparation of microporous heterometallic zeolitic imidazolate frameworks (ZIFs), where two routes (e.g., different sequences of exchanges similar to Scheme 3.1) showed very similar results out of any pathway because of the similar lability of Zn–imidazolate and Mn–imidazolate bonds. Nonetheless, considering the different M–L bond natures and structures of each MOF, our rationalizations still validate the unfeasibility of dual exchange via **path 2**, while supporting **path 1** in the current work and

the results of Cohen's work. As we have demonstrated the successful ligand exchange in PCN-333(Fe) with a variety of BTB derivatives, other functional groups could also be introduced into PCN-333(Cr). Therefore, dual exchange strategy not only provides a facile route to obtain extremely robust Cr-MOFs, but also allows a generalized functionalization method of highly stable Cr-MOFs, which can vastly expand the scope of MOF applications.

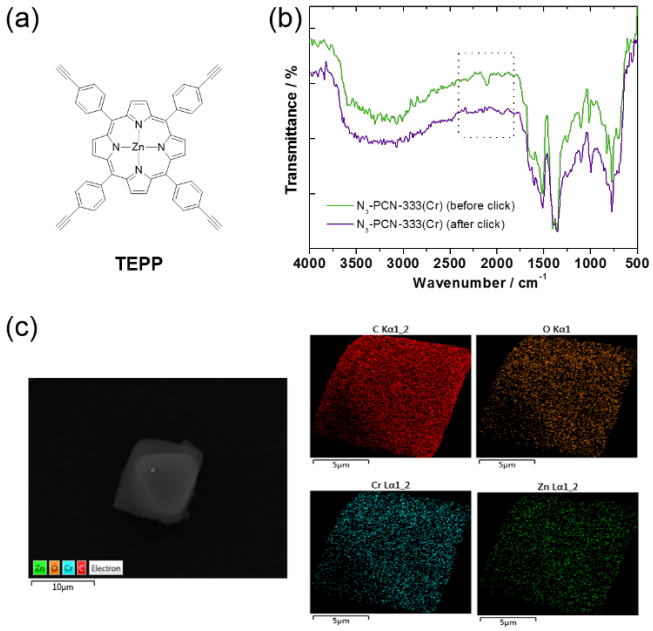

Figure 3.12 (a) TEPP used for the click reaction in N_3-PCN-333(Cr). (b) IR spectra of N_3-PCN-333(Cr) before and after the click reaction. (c) SEM-EDX mapping of N_3-PCN-333(Cr) after the click reaction.

Click reaction in N_3–PCN-333(Cr)

Having dual exchanged MOF prepared, a click reaction was performed on N_3–PCN-333(Cr) to demonstrate the introduction of large entity (Table 3.1). To illustrate our concept, *meso*-tetra(4-ethylphenyl)porphyrin (TEPP) was synthesized due to its two-dimensional large size (18 Å × 18 Å), which will demonstrate the feasibility of covalent

anchorage of a large guest molecule in the dual exchanged platform. The center of TEPP was metalated with Zn(II) aiming to achieve information about its spatial distribution by scanning electron microscopy/energy-dispersive X-ray spectroscopy (SEM/EDX). With this in mind, the click reaction between the N_3–PCN-333(Cr) and Zn-TEPP was performed in the presence of CuI in DMF (60 °C, 28 h) with stirring. The completion of reaction was determined by the disappearance of the azide band at 2106 cm^{-1} in the IR spectrum as shown in Figure 3.12b. The color of sample changed from green to dark purple upon the anchorage of Zn-TEPP in PCN-333(Cr), indicating successful incorporation of the strongly colored porphyrin (Figure 3.9a). In addition, the PXRD pattern of the clicked MOF also showed unaltered diffraction peaks, suggesting the robustness of PCN-333(Cr) scaffold (Figure 3.8). In parallel, porosity of N_3–PCN-333(Cr) was also examined. Figure 3.9b showed reduced N_2 uptake, which distinctly indicates the inserted TEPP does take up the corresponding pore volume in the MOF. Nevertheless, even after the incorporation of such large entity, the material still retains sufficient porosity (pore volume 1.60 cm^3/g) which may allow a volumetric capacity for further generations of guest molecules inclusion in PCN-333(Cr). As the size of TEPP is larger than the smallest cages (11 Å) in PCN-333, but much smaller than the middle sized cages (45 Å) and the largest cages (55 Å), theoretically Zn-TEPP can only occupy the middle sized cages and the largest cages. Expectedly, the pore size distribution showed the decreased size of middle cages and largest cages, as well as significantly decreased pore volume of those two cages while the smallest cage is not much affected after N_3–BTB insertion, which matches well with our size analysis (Figure 3.13). Next, we further sought to visualize positions of Zn-TEPP in

the PCN-333(Cr). As shown in Figure 3.12c, SEM/EDX mapping of this sample shows the inserted Zn-TEPP molecules via click reaction are well distributed throughout the crystals, indicating the exchanged ligands are well dispersed and the click reaction occurred evenly in the MOF through the efficient diffusion utilizing its large pores. Considering an ideal atomic ratio between M(III) and ligands in PCN-333(M) is 3:2 by structure, the ratio of ~5:1 between Cr(III) and N_3–BTB is expected in the framework, based on the ~30% of ligand exchange. In accordance with this analysis, the EDX results of clicked-PCN-333(Cr) matched well (Cr:Zn = 4.86:1), which further supports most azide group in the MOF reacted with the large guest molecule, TEPP, as well as successful incorporation of N_3–BTB (Table 3.2).

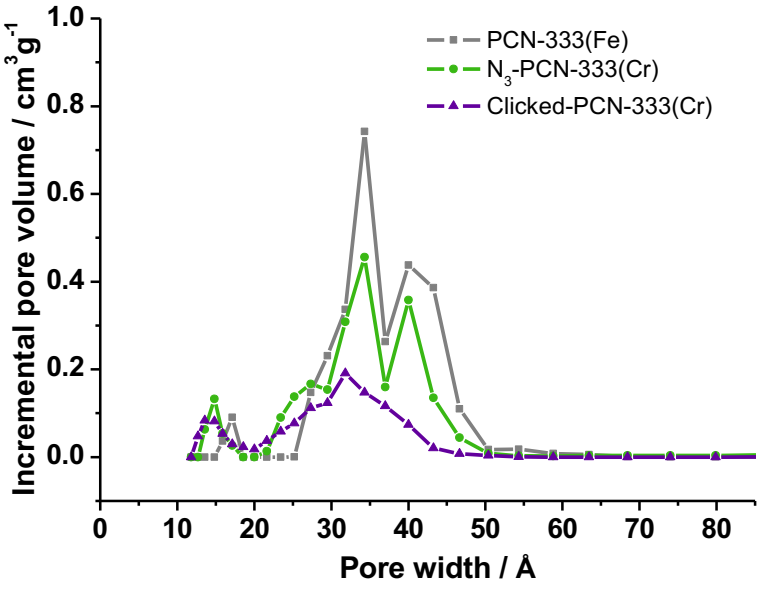

Figure 3.13 Comparison of DFT pore size distributions before and after the click reaction with TEPP (obtained from N_2 sorption isotherm at 77 K).

Table 3.2 Summary of EDX results. Numbers presented in the table were the average of at least three independent measurements. *Standard Deviation.

	Sc (atomic %)	Fe (atomic %)	Cr (atomic %)	Cr Exchange Ratio (%)	*SD (%)
PCN-333(Sc/Cr) at 85 °C	2.99	n/a	1.77	37.03	±3.79
PCN-333(Sc/Cr) at 150 °C	2.08	n/a	3.68	64.83	±2.12
PCN-333(Fe/Cr) at 85 °C	n/a	4.83	1.56	23.02	±8.34
PCN-333(Fe/Cr) at 150 °C	n/a	0.02	5.02	99.79	±0.30
N_3-PCN-333(Fe/Cr) at 150 °C	n/a	0.09	4.4	97.48	±3.56
	Fe (atomic %)	Cr (atomic %)	Zn (atomic %)	Cr:Zn ratio	
Clicked-N_3-PCN-333(Cr)	0	3.69	0.76	4.86:1	

3.4 Conclusions

In summary, a dual mode of postsynthetic exchange (dual exchange), involving a sequential exchange of ligands and metals in PCN-333(Fe) has been studied for the preparation of functionalized PCN-333(Cr). These results illustrate a possible step forward for the functionalization of mesoporous Cr-MOFs that allow covalent anchors for guest molecules, sufficient room (extralarge pore) for the introduction of secondary functionality, and exceptional stability from inert Cr(III). In addition, our rational design and analyses of dual exchange process give a comprehensive understanding of chemical dynamics in PCN-333 during dual exchange, following up our previous study of ligand exchange in this platform. The dual exchanged Cr-MOF, N_3–PCN-333(Cr) showed maintained integrity of the parent MOF, functionality, and enhanced chemical stability.

Meanwhile, dual exchange strategy may allow incorporation other wanted functional groups into PCN-333(Cr) platform, as noted. These findings have enabled the preparation of functionalized PCN-333(Cr) with a design flexibility to be utilized as a stable platform for a variety of desired applications by exploiting facile functionalization, enhanced chemical stability, and extremely large pores which will allow for more possible chemistry with MOFs.

4. PHOTOCHROMIC METAL–ORGANIC FRAMEWORKS: REVERSIBLE CONTROL OF SINGLET OXYGEN GENERATION*

4.1 Introduction

Singlet oxygen ($^1O_2$) is a reactive oxygen species (ROS) which can be generated by cellular metabolism, redox chemistry, or photosensitization between a photosensitizer and molecular oxygen ($^3O_2$) upon irradiation.[133-138] The development of a photosensitizer for the generation of singlet oxygen is of great interest owing to potential applications including industrial wastewater, photochemical synthesis, and photodynamic therapy (PDT).[139-146] While progress has been made to advance photosensitizers, more recently the design of a system in which the production of singlet oxygen is can be controlled or activated, upon environmental changes or interaction with biomolecules or nanomaterials, has attracted growing attention.[139,147-153] However, such methods often involve irreversible or passive interaction, which may lead to imprecise control over $^1O_2$ generation. In this sense, a system which inherently bears a photosensitizer and control functionality could be ideal to achieve controlled generation of singlet oxygen.

Photochromic molecules, which upon photoirradiation exhibit a reversible transformation between isomers having different properties, hold considerable promise for optical switches as a control unit in smart materials.[154-156] Of the many photochromic compounds, dithienylethene (DTE) derivatives are one of the most promising class of compounds because of their thermal stability, rapid response, and fatigue resistance.[154,157-

*Reproduced with permission from Park, J.; Feng, D.; Yuan, S.; Zhou, H.-C. *Angew. Chem. Int. Ed.* **2015**, *54*, 430–435. Copyright 2015 Wiley-VCH Verlag GmbH & Co. KGaA, Weinheim.

[160] By employing the DTE photochromic switch and a porphyrinic photosensitizer in a homogeneous bicomponent system, Feringa et al. have recently demonstrated reversible control of singlet oxygen generation.[161]

Attachment of the catalyst onto solid support materials, such as silica or metal oxides, has shown the potential to integrate distinctive attributes of both homogeneous and heterogeneous catalysis.[162-164] For instance, a heterogeneous system of two or more incompatible components could be of great value because of the ability to accommodate various functionalities as well as efficient recovery and recyclability. Along these lines, researchers have strived to design a photosensitizer in a hybrid material form to incorporate these features into one system for photocatalysis.[165-173] However, most of the approaches suffer from synthetic difficulty, leaching, and improper spatial arrangement.[162,167,174]

Metal–organic frameworks (MOFs) are an emerging class of porous materials and have captured widespread research interest because of their design flexibility and viability in potential applications such as gas storage/separation, sensing, and catalysis.[1,70,71] More recently, MOFs have been explored as light-harvesting platforms.[6,175-179] Because MOFs provide highly ordered structures in proximity to each other but not in direct contact, incorporation of chromophores as linkers to construct MOFs gives rise to an efficient platform for energy transfer. As a result of the structural diversity and tunability of MOFs, it is very convenient to introduce multiple functional moieties into the framework, thus making MOFs as ideal candidates for realizing cooperative functionalities based on periodic arrangement on a molecular scale.[180] Meanwhile, leaching of each component

can be alleviated on account of the strong coordination bond. Moreover, the porous feature of MOFs allows all the functionalities within the framework to be accessible by incoming reactants regardless of their solubility.

Herein, we present two MOFs, namely PC-PCN (photochromic porous coordination network) and SO-PCN (singlet oxygen-generating porous coordination network) which contain 1,2-bis(2-methyl-5-(pyridin-4-yl)thiophen-3-yl)cyclopent-1-ene (BPDTE) as a photochromic switch. Notably, a molecular dyad system which contains a photochromic switch and photosensitizer was well established with SO-PCN. The reversible control over $^1O_2$ generation through a competition of energy transfer pathways upon irradiation at specific wavelengths in SO-PCN was studied. Also, SO-PCN was demonstrated as a heterogeneous catalyst for photooxidation of 1,5-dihydroxynaphthalene (DHN).

4.2 Experimental section

Materials

All starting materials and solvents were used as received without further purification from commercial suppliers. 2-Chloro-5-methylthiophene was purchased from Alfa Aesar. Silica gel (40 – 42 μm) was purchased from Silicycle Inc. The abbreviation for some solvents and reagents were listed here: *N*,*N*-dimethylformamide (DMF), dimethylsulfoxide (DMSO), acetonitrile (MeCN), tetrahydrofuran (THF), and ethyl acetate (EtOAc).

Instrumentation

Synthetic manipulations that required an inert atmosphere (where noted) were carried out under nitrogen using standard Schlenk techniques. Nuclear magnetic resonance (NMR) spectra were recorded on Mercury 300 spectrometer and Varian Inova 500 spectrometer. The chemical shifts are given in units of δ (ppm) relative to tetramethylsilane (TMS) where δ (TMS) = 0, or referenced to the residual solvent resonances. Splitting patterns are denoted as s (singlet), d (doublet), t (triplet), q (quartet), quin (quintet), m (multiplet), and br (broad). Single crystal diffraction data set was collected at 110 K on a Bruker APEX CCD diffractometer with MoKα radiation (λ = 0.71609 Å). Powder X-ray diffraction (PXRD) was carried out on a Bruker D8-Focus Bragg-Brentano X-ray powder Diffractometer equipped with a Cu sealed tube (λ = 1.54178) at 40 kV and 40 mA. UV-Vis spectra were recorded on Shimadzu UV-2450 spectrophotometer. Fluorescence spectra were recorded on Horiba Fluorolog spectrofluorometer. Fourier transform infrared (IR) measurements were performed on a Shimadzu IR Affinity-1 spectrometer. High resolution electrospray ionization mass (ESI-MS) spectra was obtained at Texas A&M university mass spectrometry facility.

Synthesis

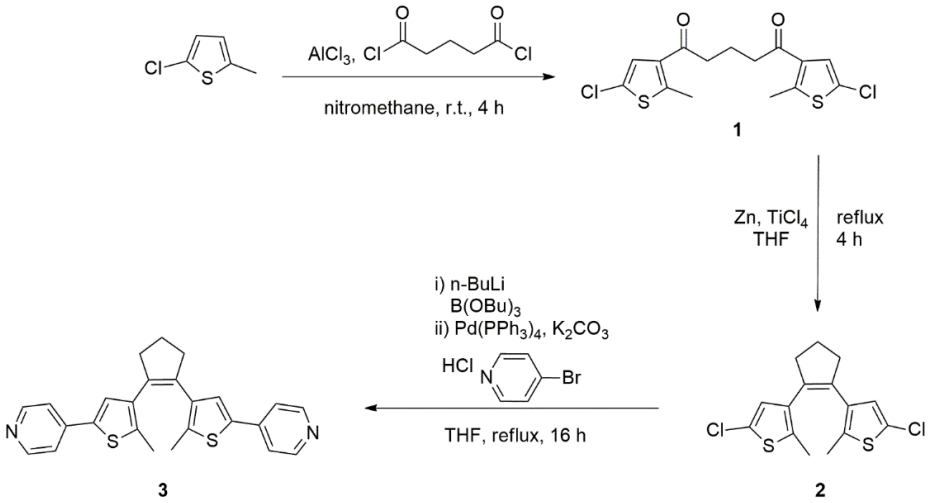

Scheme 4.1 Synthetic scheme of **3**

1,5-Bis-3-(2-chloro-5-dimethylthienyl)-1,5-pentadione (1). To a mixture of 2-Chloro-5-methylthiophene (5 g, 37.7 mmol) and glutaryl chloride (3 g, 17.95 mmol) in nitromethane (150 mL) was added $AlCl_3$ (5.3 g, 39.5 mmol) under N_2 atmosphere at 0 °C. The solution was then stirred for 4 h at room temperature. Afterward, the reaction mixture was poured onto ice-water and the resulting mixture was extracted with CH_2Cl_2. The combined organic layers were dried over anhydrous $MgSO_4$, the solvent was removed *in vacuo* and the resulting crude product was purified by column chromatography (silica, hexanes: EtOAc = 30:1) to yield **1** as a light yellow solid (84%).^{1}H NMR (500 MHz, $CDCl_3$): δ = 7.18 (s, 2H), 2.86 (t, 4H), 2.66 (s, 6H), 2.06 (quin, 2H). ^{13}C NMR (125 MHz, $CDCl_3$): 194.9, 147.7, 134.9, 126.8, 125.3, 40.5, 18.1, 16.1.

1,2-bis(5-chloro-2-methylthiophen-3-yl)cyclopent-1-ene (2). $TiCl_4$ (3.9 g, 20.7 mmol) was dissolved cautiously in ice-cooled dry THF (200 mL) under N_2 atmosphere whereupon the solution turned yellow. To the mixture was added Zn powder (1.63 g, 25

mmol) and the resulting mixture was stirred for 45 min at 65 °C. Afterwards, the reaction was cooled to 0 °C with an ice bath and compound **1** (3 g, 8.3 mmol) was added and was reheated to 65 °C for 4 h. A few drops of saturated aq. K_2CO_3 solution was added to the mixture followed by filtration over Celite and washing with EtOAc, and the filtrate was dried over anhydrous $MgSO_4$. The crude product was purified by column chromatography (silica, pure hexanes) to afford **2** as a pale yellow solid (91%). ^{1}H NMR (500 MHz, $CDCl_3$): δ = 6.58 (s, 2H), 2.71(t, 4H), 2.02 (qiun, 2H), 1.88 (s, 6H). ^{13}C NMR (125 MHz, $CDCl_3$): δ = 134.8, 134.4, 133.3, 126.7, 125.2, 38.3, 22.8, 14.2.

1,2-bis(2-methyl-5-(pyridin-4-yl)thiophen-3-yl)cyclopent-1-ene (3). To a two-neck round bottom flask, 1,2-bis(5-chloro-2-methylthiophen-3-yl)cyclopent-1-ene (2.44 g, 7.41 mmol) and dry THF (30 mL) were added under nitrogen atmosphere. The resulting mixture was cooled with an ice bath and 2.5 M *n*-BuLi (6.52 mL, 16.3 mmol) was slowly added. During the addition the mixture turned dark pink. Upon completion of addition, it was stirred for another 30 min at the same temperature. Subsequently, *tris*-*n*-butylborate (5.12 g, 6.0 mL, 22.23 mmol) was added and the resulted orange solution was allowed to warm up to room temperature and stirred for 1h. Concurrently to another two-neck flask equipped with a condenser, $Pd(PPh_3)_4$ (500 mg, 5 mol%) was suspended in THF (25 mL) and the resulting mixture was heated at 70 °C. After 30 min, aqueous 2.5 M K_2CO_3 (30 mL), ethylene glycol (10 drops), 4-bromopyridine hydrochloride (3.16 g, 16.3 mmol) were added. Afterwards, previously prepared reaction mixture was slowly added to this orange solution. The mixture was heated at 70 °C overnight until complete consumption of starting materials and cooled to room temperature followed by addition of water (20 mL).

Crude was extraction with diethyl ether and the combined organic phases were dried over anhydrous $MgSO_4$, the solvent was removed *under vacuum* and the resulting crude product was purified by column chromatography (silica, pure acetone) to yield **3**. The product was obtained as a light violet solid in 91% yield. ^{1}H NMR (500 MHz, $CDCl_3$): δ = 8.55 (d, 4H), 7.43(d, 4H), 7.28 (s, 2H), 2.87 (t, 4H), 2.14 (quin, 2H), 2.05 (s, 6H).

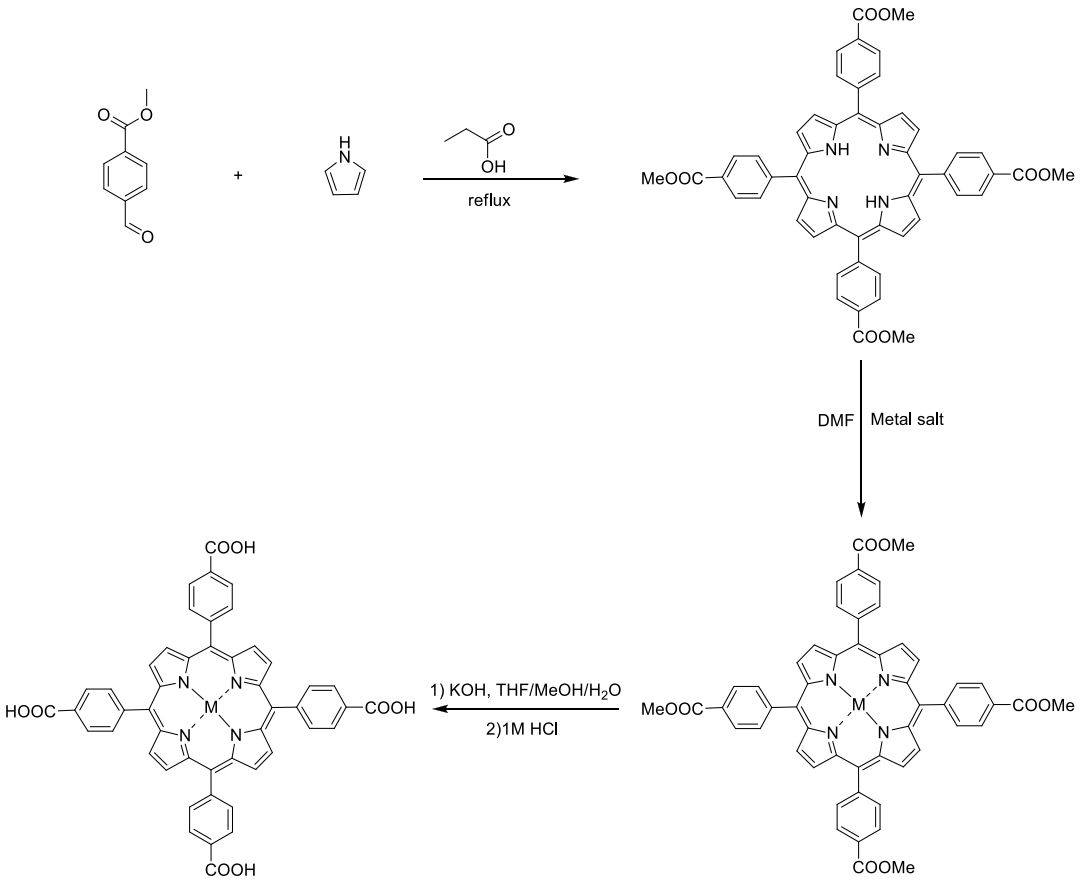

Scheme 4.2 Synthesis of **M-TCPP**

5,10,15,20-Tetrakis(4-methoxycarbonylphenyl)porphyrin (TPPCOOMe). To refluxed propionic acid (100 mL) in a 500 mL three-neck flask were added pyrrole (3.0 g, 0.043 mol) and methyl *p*-formylbenzoate (6.9 g, 0.042 mol), and the mixture was refluxed for 12 h in dark. After the reaction mixture was cooled to room temperature, crystals were

collected by filtration to afford purple crystals (1.9 g, 21% yield). ^{1}H NMR (300 MHz, $CDCl_3$) δ = 8.81 (s, 8H), 8.43 (d, 8H), 8.28 (d, 8H), 4.11 (s, 12H), 2.83 (s, 2H).

[5,10,15,20-Tetrakis(4-carboxyphenyl)porphyrinato]-Zn(II). The obtained ester compound (0.75 g) was stirred in THF (25 mL) and MeOH (25 mL) mixed solvent, to which a solution of KOH (2.63 g, 46.95 mmol) in H_2O (25 mL) was introduced. This mixture was refluxed for 12 h. After cooling down to room temperature, THF and MeOH were evaporated. Additional water was added to the resulting water phase and the mixture was heated until the solid was fully dissolved, then the homogeneous solution was acidified with 1 M HCl until no further precipitate was detected. The violet solid was collected by filtration, washed with water and dried in vacuum. FTIR (KBr): ν= 3438 (m), 3040 (m), 2665 (w), 1680 (s), 1605 (s), 1565 (m), 1504 (m), 1423 (s), 1316 (m), 1291 (s), 1182 (m), 1105 (m), 1002 (s), 867 (m), 798 (s), 768 (m), 720 (m) cm^{-1}.

[5,10,15,20-Tetrakis(4-methoxycarbonylphenyl)porphyrinato]-Fe(III) Chloride. A solution of TPP-COOMe 0.854 g (1.0 mmol) and $FeCl_2 \cdot 4H_2O$ (2.5 g, 12.8 mmol) in 100 mL of DMF was refluxed for 6 h. After the mixture was cooled to room temperature, 150 mL of H_2O was added. The resultant precipitate was filtered and washed with 50 mL of H_2O for two times. The obtained solid was dissolved in $CHCl_3$, followed by washing three times with 1 M HCl and twice with water. The organic layer was dried over anhydrous magnesium sulfate and evaporated to afford quantitative dark brown crystals. FTIR (KBr): ν= 3444 (m), 3034 (w), 2634 (w), 1702 (s), 1614 (s), 1570 (m), 1404 (s), 1311 (m), 1277 (s), 1204 (m), 1180 (m), 1106 (m), 1004 (s), 862 (m), 799 (s), 770 (s), 721 (m) cm^{-1}.

Synthesis of PC-PCN. BPDTE (9 mg), DBTCB (10 mg), $Zn(NO_3)_2.6H_2O$ (35 mg), and tetrafluoroboric acid (one drop) in 2 mL of DMF were ultrasonically dissolved in a 4 mL Pyrex vial. The mixture was heated at 85 ºC in a pre-heated oven for 18 h. After cooling to room temperature, a light yellow crystal was harvested.

Synthesis of SO-PCN. H_2-TCPP (10 mg), $Zn(NO_3)_2.6H_2O$ (35 mg) in 2 mL of DMF/DEF were ultrasonically dissolved in a 4 mL Pyrex vial. The mixture was heated at 85 ºC in a pre-heated oven for 2 h. After that, BPDTE (9 mg) and tetrafluoroboric acid (1 μL) were added and the mixture was heated for 12 h. After cooling to room temperature, purple crystals were harvested.

Instrumental set-up and general procedure

Spectrophotometric grade CH_3CN was used for spectroscopic measurements (Acros). Zn-TCPP was excited by 405 nm CW laser and laser power was measured by a laser powermeter (Thorlabs). Visible irradiation was provided using a fiber optic coupled halogen lamp (150 W, AmScope) combined with a 450 nm long pass filter (Thorlabs). UV irradiation was made using a 365 nm spectroline lamp (0.2 amp). To close the BPDTE 30 min of UV irradiation was employed, while 2 h of visible light was irradiated to re-open the BDPTE pillar.

Prior to addition of the DPBF, SO-PCN was washed thoroughly with hot DMF followed by acetonitrile until no residual ligands in the supernatant were detected by UV-Vis spectroscopy. Acetonitrile was bubbled with oxygen for 20 min before the measurements, where experiments are conducted in the presence of oxygen. For the control experiment in which the absence of oxygen was required, stock solution and

reaction medium were bubbled with nitrogen flow for 30 min. All stock solutions and SO-PCN samples prepared were kept in the dark before the measurements.

4.3 Results and discussion

Porphyrin derivatives have been widely used for $^1O_2$ generation because of their well-known photochemistry and high efficiency in light harvesting.[140] The dithienylethene derivative, BPDTE, serving as a photochromic switch can undergo a reversible 6π electrocyclic reaction upon photoirradiation at distinct wavelengths (e.g., ultraviolet or visible). The open and closed forms of BDPTE resulting from photoisomerization exhibit distinctive absorption properties, and can provide different energy transfer pathways for photosensitizers to control the $^1O_2$ generation (Figure 4.1a,c). As one of the most frequently used linkers in porphyrinic MOFs, tetrakis(4-carboxyphenyl)-porphyrin (TCPP) has been extensively explored to construct different MOFs.[6,177,181] Particularly, pillar-layer three-dimensional (3D) frameworks, which are constructed from TCPP mixed with linear dipyridyl linkers, have been widely studied because of the ease of design and synthesis. Simultaneously, BPDTE, having dipyridyl heads, is ideal for forming the pillar-layer structure with TCPP to provide a solid-state platform for the controlled generation of singlet oxygen.

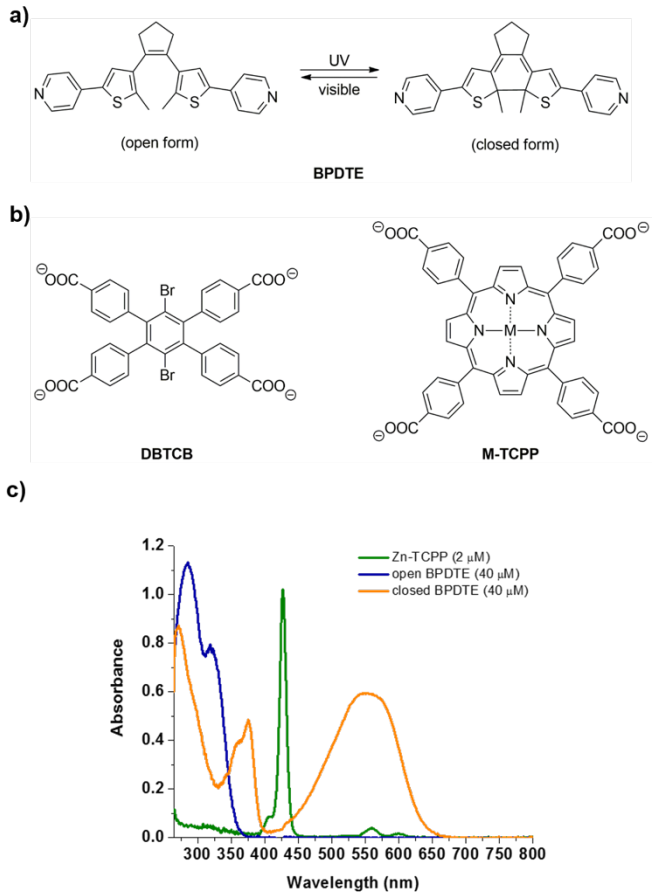

Figure 4.1 (a) Photoisomerization of BPDTE under UV and visible light. (b) Structures of ligands consist of 2D layers in **PC-PCN** and **SO-PCN**, respectively. (c) UV-Vis spectra of H_4Zn-TCPP and two different forms of BPDTE.

Such structures lead to a paddlewheel-type of inorganic building block and gives rise to a 1:1 ratio between the photosensitizer (TCPP) and the photochromic switch (BPDTE), and precisely matches the stoichiometry in an ideal energy transfer process. We selected Zn^{2+} as the inorganic species, because its d^{10} configuration is unlikely to disturb the energy transfer between TCPP and BPDTE. In general, photoisomerizations rarely occur in crystals because a large structural change is extremely unfavorable in the solid state. As an exceptional example, DTE derivatives undergo only a small structural change

upon photoisomerization and therefore photochromism in the single crystalline phase can be achieved.[182] Thus BPDTE in the framework may still retain its photochromic property without significant alteration or breaking of the 3D structure.

The solvothermal reaction of BPDTE, TCPP (no metal), $Zn(NO_3)_2 \cdot 6H_2O$ in DMF and tetrafluoroboric acid at 85 °C for 15 hours resulted in platelike, dark-purple single crystals (SO-PCN). Although some of the single crystals are large enough in two of the three dimensions, because of the limited thickness of the crystals, diffractions from certain directions are too weak to determine the overall structure. Since the crystal growth behavior differs with the variation of the metal species within the TCPP center, as observed for a series of Zr-MOFs,[33,183] we tried other metallo-TCPP (M-TCPP, where M is Cu, Co, Ni, Mn, and Fe) species and obtained much thicker crystals using Fe-TCPP. With better diffraction patterns, the space group of SO-PCN was determined to be *P4/mmm*, which has a unit cell parameter of $a \approx 16.63$ Å and $b \approx 22.28$ Å. From the solved structure, porphyrin layers are clearly observed while the pillars are missing because of the random orientation of the pillars resulting from the free rotation of the single bonds. However, the distance between Zn_2 paddlewheels in the adjacent layers precisely matches the length of BPDTE, which indicates the formation of our expected structure. The simulated structure showed good agreement with the experimental PXRD pattern of SO-PCN. ^{1}H NMR spectrum, upon digestion of SO-PCN, shows a 1:1 ratio between Zn-TCPP and BPDTE, and further confirms the structure.

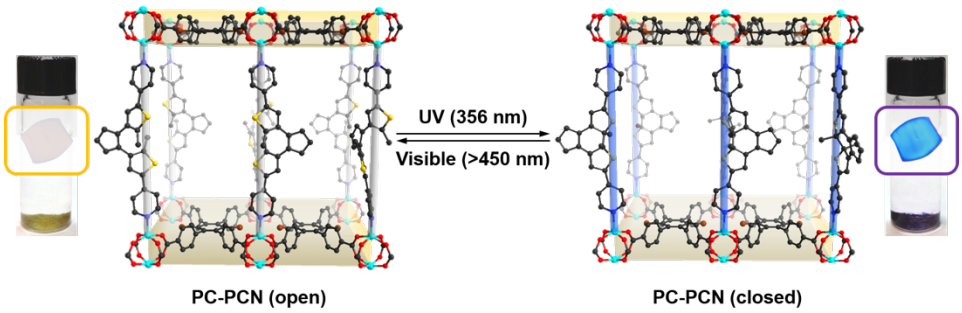

Figure 4.2 Illustration of reversible photochromic reaction in **PC-PCN**. Colorless single crystal (left, bulk in yellow) turns blue (right, bulk in purple) upon UV irradiation (λ=365 nm) and it goes back to colorless form under visible light (with λ=450 nm cut-on filter). Single crystals are highlighted in the insets.

Intuitively, direct evidence showing the presence of BPDTE in SO-PCN could be a color change of BPDTE upon photoirradiation. However, the dark-purple Zn-TCPP impedes the observation of the color change from the photochromic pillar. Hence, we chose a colorless tetratopic carboxylate linker DBTCB, which has been reported to form a similar structure with TCPP, to show the photochromism of the BPDTE pillar (Figure 4.1b). Under similar solvothermal conditions, a colorless flake-shaped single crystal of PC-PCN, which has a light-yellow color in the bulk sample, was obtained (Figure 4.2). Single-crystal X-ray diffraction of PC-PCN shows dipyridine coordination but the BPDTE pillar was not clearly solved because of the significant disorder as discussed above. PC-PCN exhibits the same layer to layer distance (21.69 Å) as in SO-PCN and also exhibits a 1:1 ratio between BPDTE and DBTCB, thus further validating SO-PCN as our expected structure. When the open form of PC-PCN in the bulk was irradiated under ultraviolet (UV) light, deep-purple crystals of PC-PCN were clearly observed by the naked eye within 10 minutes, and suggests the pillar ligands were closed. Irradiation with visible light

(λ>450 nm) was performed on these purple crystals to re-open the closed pillars and the recovery of the light-yellow color was observed in 1 hour. We further examined the photochromic reaction in a single crystal to single crystal fashion in PC-PCN. As shown in Figure 4.2, single crystallinity of PC-PCN was almost completely maintained upon alternating irradiation, thus demonstrating excellent structural reversibility of the BPDTE pillar within the framework.

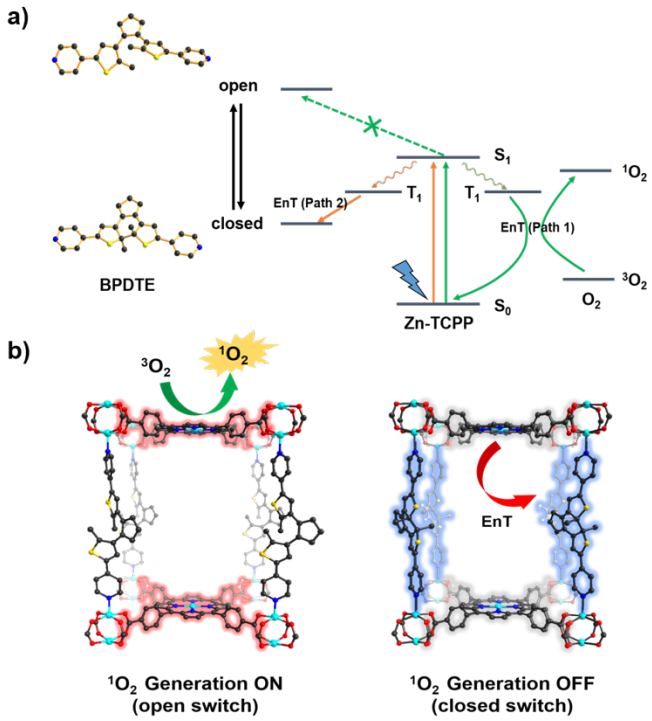

Figure 4.3 (a) Proposed mechanism of energy transfer (EnT) in **SO-PCN**. (b) Illustration of switching operation in **SO-PCN**.

Having demonstrated the photoisomerization of BPDTE in PC-PCN, we then examined SO-PCN for regulating $^1O_2$ generation. To evaluate the ability of SO-PCN in generating singlet oxygen, 1,3-diphenylisobenzofuran (DPBF), a well-known $^1O_2$

scavenger, was used to detect the $^1O_2$ produced in our system. Upon oxidative degradation of DPBF by $^1O_2$, the absorption of DPBF at λ=410 nm decreased, thus serving as an indication of the singlet oxygen generated. First, the experiment was carried out using a visible light source (λ>450 nm) at room temperature to examine the photosensitizing ability of SO-PCN. Prior to addition of the probe, SO-PCN was washed thoroughly with hot DMF followed by acetonitrile until no residual ligands in the supernatant were detected by UV-Vis spectroscopy. Acetonitrile was bubbled with oxygen for 20 minutes before the measurements.

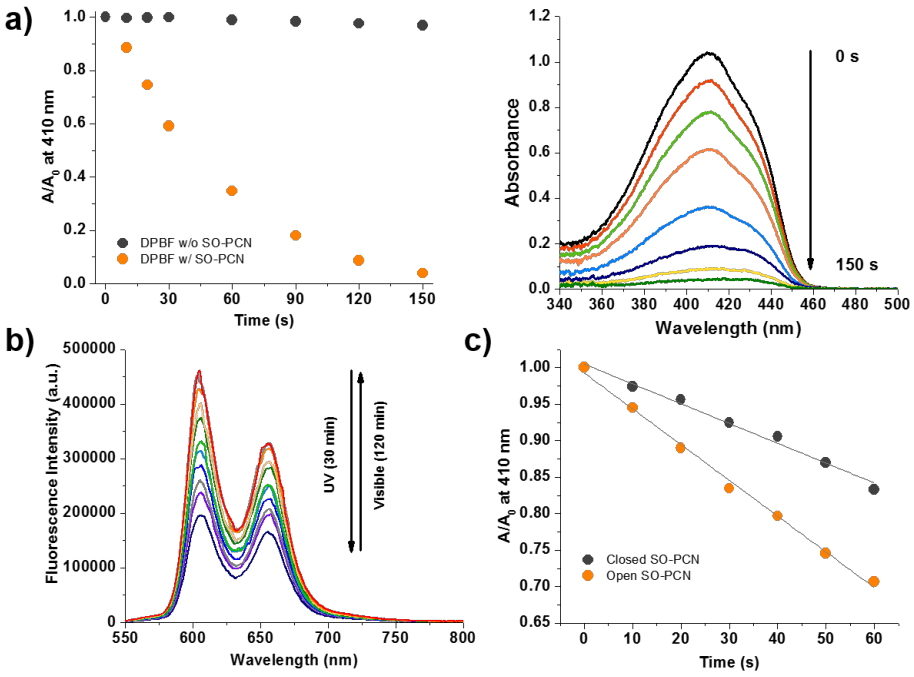

Figure 4.4 (a) Absorbance decay of DPBF (left) and the corresponding spectra in the presence of **SO-PCN** (right). (b) Emission spectra of **SO-PCN** showing reversibility. (c) Comparison of decay rate of DPBF upon on/off switching.

As a control experiment, DPBF (50 μM) in acetonitrile without SO-PCN was

irradiated by visible light (λ>450 nm). Only a negligible decrease in the absorbance of DPBF was observed during 150 seconds of irradiation, and indicates DPBF was stable under these conditions. Knowing this, we examined the photosensitization of the open form of SO-PCN (1.42 μmol) using DPBF (50 μM) in 2.8 mL of acetonitrile. Upon irradiation, the absorbance at λ=410 nm showed a complete degradation within 150 seconds, thus suggesting excellent photosensitizing ability of SO-PCN (Figure 4.4a).

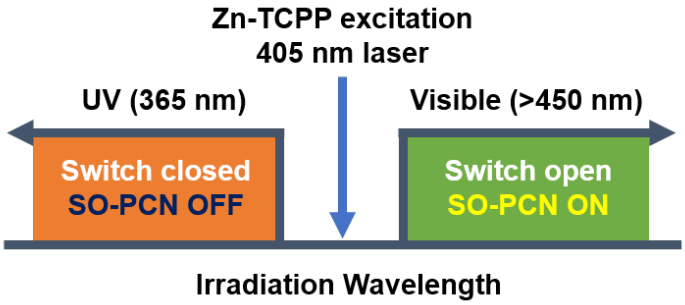

Figure 4.5 Scheme of switching operation in SO-PCN.

Next, we investigated the control of the switch (BPDTE) embedded in SO-PCN for $^1O_2$ generation upon photoisomerization. Figure 4.3a illustrates a proposed mechanism of control of $^1O_2$ generation in SO-PCN by an energy transfer (EnT) process. Energy transfer of excited Zn-TCPP is known to be dependent on triplet energy of BPDTE[161,184-186] because of different photophysical properties of its isomers. When Zn-TCPP in SO-PCN is excited, the triplet energy of ^{3}[Zn-TCPP]* can follow different pathways for energy transfer depending on the state of BPDTE. For example, $^1O_2$ can be generated when the EnT process occurs from ^{3}[Zn-TCPP]* in the open form of SO-PCN to $^3O_2$ (Path 1 in Figure 4.3a). Another pathway is based on the energy state of closed form of BPDTE,

which lies at a lower energy than that of ^{3}[Zn-TCPP]*, thus the energy transfer takes place to the closed BPDTE and results in quenching of $^1O_2$ generation. The feasibility of reversible energy transfer of the TCPP-BPDTE dyad in SO-PCN was evaluated by recording emission spectra. We chose a Soret band (λ=420 nm) to excite the SO-PCN to circumvent potential interference of the switching operation (Figure 4.5). The emission spectrum of open SO-PCN shows emission maxima at λ=605 nm and λ=655 nm in CH_3CN (λ_{ex}=420 nm). To close the BPDTE pillars in SO-PCN, UV light (λ=365 nm) was used. The emission was gradually quenched by EnT to the closed BPDTE and no further quenching was observed after 30 minutes. Recovery of emission upon photoisomerization was subsequently carried out with visible light (λ>450 nm), and a complete recovery was made in 120 minutes (Figure 4.4b).

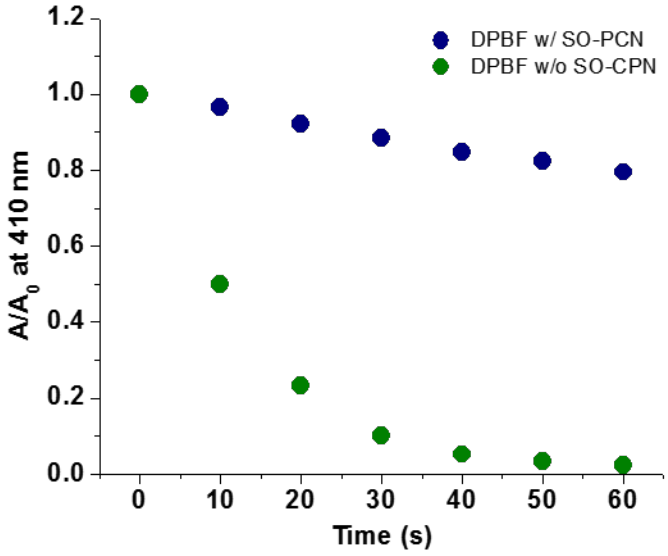

Figure 4.6 Control experiments showing absorbance decay of (green) pure DPBF in the absence of SO-PCN and (blue) DPBF with the closed form of SO-PCN in the absence of oxygen.

After validating reversibility in SO-PCN, the system was excited by a λ=405 nm CW laser to examine the controlled $^1O_2$ generation by on/off switching (Figure 4.3b). Evolution of $^1O_2$ with the open form of SO-PCN was monitored by UV/Vis spectra every 10 seconds. Over the course of 60 seconds with 6 mW cm^{-2} of laser power, 30 % of DPBF absorption decreased compared to its initial absorption, whereas the closed form of SO-PCN showed an approximately 15 % decrease in absorbance at λ=410 nm. A steeper slope of the open form of SO-PCN suggests the energy of ^{3}[Zn-TCPP]* was transferred to $^3O_2$ to generate $^1O_2$, while that of the closed form was quenched by closed BPDTE, thus resulting in less efficient $^1O_2$ generation (Figure 4.4c). When we attempted to perform a control experiment, we found that the laser irradiation led to a complete degradation of DPBF in the absence of SO-PCN within 60 seconds (Figure 4.6). Presumably because of the light sensitive nature of DPBF, the laser significantly affected DPBF solution in the absence of other chromophores. To obtain a practical blank of our system, we further examined the system with DPBF and the closed form of SO-PCN. An N_2 saturated solvent was employed to suppress the supply of oxygen so that we could examine the system solely with photodegradation of DPBF in the presence of closed SO-PCN (other chromophores). Interestingly in this control experiment, the rate and extent of decrease in absorption at λ=410 nm of DPBF were very similar to previous experimental data of the closed SO-PCN with oxygen (Figure 4.6), and further confirms that a successful switching operation, using photoisomerization of BPDTE towards $^1O_2$ generation in SO-PCN, was demonstrated.

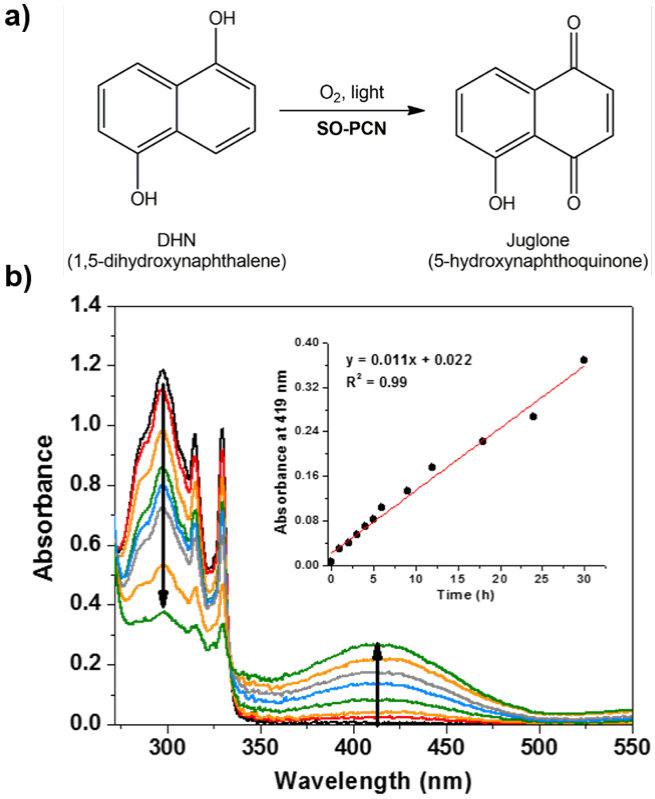

Figure 4.7 (a) Photooxidation of DHN catalyzed by **SO-PCN** in the presence of oxygen and light irradiation. (b) UV-Vis spectra of photooxidation of DHN in CH_3CN catalyzed by **SO-PCN**. Inset: Absorbance of juglone (λ=419 nm) as a function of reaction time.

In addition to the ability to generate singlet oxygen, we further sought to study potential use of SO-PCN as a heterogeneous catalyst. Catalytic performance was demonstrated by photooxidation of DHN, which is mediated by $^1O_2$ and resulted in the corresponding oxidized product juglone (Figure 4.7a). The photooxidation was carried out with 0.036 mmol of DHN in acetonitrile with 10 % SO-PCN (open form) under visible light irradiation (λ>450 nm). As the reaction occurred, the absorption peaks of the starting material at λ=298 nm and 330 nm decreased, whereas a characteristic peak of juglone

around λ=419 nm increased. After 30 hours, a significant decrease in absorption of DHN was observed, while leaching was not seen (Figure 4.7b).

4.4 Conclusions

In summary, through a classical pillar-layer structure, we have developed two photochromic MOFs, PC-PCN and SO-PCN. Photochromism has been successfully realized in PC-PCN while maintaining its single crystallinity. In particular, as a solid-state material which inherently integrates a photochromic switch and photosensitizer, SO-PCN has demonstrated reversible control of $^1O_2$ generation. Meanwhile, SO-PCN shows catalytic activity towards photooxidation of DHN. Based on the photophysical properties of the chromophore dyads realized within the MOF regime, our findings can be extended to the design of materials for potential applications in photocatalysis, photoswitching, and sensing.

5. CONTROLLED GENERATION OF SINGLET OXYGEN IN LIVING CELLS WITH TUNABLE RATIOS OF THE PHOTOCHROMIC SWITCH IN METAL–ORGANIC FRAMEWORKS*

5.1 Introduction

The development of photosensitizers that can control the generation of singlet oxygen ($^1O_2$) has gained increasing attention in photodynamic therapy (PDT) research to reduce nonspecific damage from undesirably generated $^1O_2$.[147,148] PDT is a minimally invasive cancer treatment using cytotoxic $^1O_2$ that is generated by energy transfer (EnT) from an excited photosensitizer to molecular oxygen ($^3O_2$) upon appropriate light irradiation.[187,188] In this regard, the addition of an activation step provides another layer of selectivity on top of the localized nature of PDT, which is based on the directed light placement at the tumor site. As such, PDT with an activatable photosensitizer becomes an appealing therapeutic option whose sensitizing ability is activated in response to target stimuli.[147,189-191] However, common activation mechanisms often involve irreversible or passive means. Therefore, the capability of controlling $^1O_2$ generation in a non-invasive and reversible manner is highly desired in photosensitizers.

To address this issue, a molecular dyad consisting of a porphyrinic photosensitizer and a dithienylethene (DTE) derivative as a molecular switch to reversibly turn on/off the $^1O_2$ generation was reported.[154,161,192-194] However, the delivery of such a complex system

*Reproduced with permission from Park, J.; Jiang, Q.; Feng, D.; Zhou, H.-C., *Angew. Chem. Int. Ed.* **2016**, *55,* 7188–7193. Copyright 2016 Wiley-VCH Verlag GmbH & Co. KGaA, Weinheim.

with multiple components is a formidable challenge in biological environments owing to the different molecular properties of each component, resulting in distinctive cell response or permeability.[195,196]

As a promising class of nanocarriers, metal–organic frameworks (MOFs) have captured extensive research interest because of their high porosity, synthetic tunability, and structural diversity.[1,13,197] Recently, MOFs have been studied as an efficient platform for energy transfer between linkers because of the highly accessible and spatially discrete linkers in the framework.[100,177,186,198-201] Herein we show energy transfer-based $^1O_2$-controlled PDT using a Zr-MOF as a nanocarrier, in which the photosensitizing system installed in the MOF pores can control the $^1O_2$ generation using a photochromic switch. A widely employed photosensitizer, porphyrin[140] and a DTE derivative were successfully incorporated into the Zr-MOF with adjustable ratios. Our strategy, therefore, allows optimization of the energy transfer for $^1O_2$ control via fine-tuning of the ratios between two dyes incorporated into the MOF, as well as a successful delivery of the dyad into cells.

5.2 Experimental section

Materials

Terephthalic acid (BDC) and 4-(2-Hydroxyethyl) piperazine-1-ethanesulfonic acid (HEPES) were purchased from Sigma-Aldrich. Tetrakis(4-carboxyphenyl)porphyrin (H_2TCPP) was purchased from Frontier Scientific. Dulbecco's modified Eagle medium (DMEM/HIGH GLUCOSE 1X) were purchased from HyClone, GE Life Sciences. Fetal bovine serum (FBS) was purchased from Gibco, Thermo Fisher Scientific. Cell culture

reagents were purchased from Invitrogen. Singlet Oxygen Sensor Green were purchased from Life Technologies (USA). Cell Counting Kit-8 (CCK-8) was obtained from Beyotime Institute of Biotechnology. Other chemicals were of at least analytical grade and were used as received. All aqueous solutions were prepared with Milli-Q water generated from a Milli-pore system (Bedford, MA). All other not mentioned starting materials and solvents were used as received without further purification from the following suppliers (Alfa Aesar, Sigma-Aldrich, TCI America, Cambridge Isotope, Oakwood Products, Fisher Scientific). The abbreviation for some solvents and reagents were listed here: *N,N*-dimethylformamide (DMF), ethyl acetate (EtOAc), and dimethylsulfoxide (DMSO).

Instrumentation

Synthetic manipulations that required an inert atmosphere (where noted) were carried out under nitrogen using standard Schlenk techniques. Nuclear magnetic resonance (NMR) spectra were recorded on Varian Inova 500 spectrometer. The chemical shifts are given in units of δ (ppm) relative to tetramethylsilane (TMS) where δ (TMS) = 0, or referenced to the residual solvent resonances. Splitting patterns are denoted as s (singlet), d (doublet), t (triplet), q (quartet), quin (quintet), m (multiplet), and br (broad). Powder X-ray diffraction (PXRD) was carried out on a Bruker D8-Focus Bragg-Brentano X-ray Powder Diffractometer equipped with a Cu sealed tube (λ = 1.54178) at 40 kV and 40 mA. N_2 sorption isotherms at 77 K were measured by using a Micrometritics ASAP 2420 system with high-purity grade (99.999%) of gases. UV-Vis spectra were recorded on Shimadzu UV-2450 spectrophotometer. Fluorescence spectra were recorded on a Hitachi F-4600 spectrometer (Hitachi Co. Ltd., Japan) with Xe lamp as the excitation source at

room temperature. Visible irradiation was provided using a fiber optic coupled halogen lamp (150 W, AmScope) combined with a 450 nm long pass filter (Thorlabs). UV irradiation was made using a 365 nm spectroline lamp (0.2 amp) unless otherwise noted. Dynamic light scattering and Zeta potential were measured at 25 °C on a Zetasizer Nano ZS ZEN3600 analyser (Malvern Instrument Ltd, UK). Singlet oxygen was generated from a CEL-S500 xenon lamp with separate passing filter (power density was 100 mW/cm^2). Confocal laser scanning microscopy (CLSM) images were performed on an Olympus FV1000-IX81 CLSM and a Leica TCS SP confocal system (Leica, Germany). TEM images were taken on a transmission electron microscopy (JEOL JEM-2100F, Japan) operated at an acceleration voltage of 200 keV by dropping solution onto a carbon-coated copper grid. SEM image were recorded on a scanning electron microscopy (Hitachi S4800, Tokyo, Japan) operates at 10 keV. Energy-dispersive X-ray spectroscopy (EDS) characterization were taken on a scanning electron microscopy (Hitachi S4800, Tokyo, Japan) operates at 15 keV. X-ray photoelectron spectroscopy (XPS) was performed on an ESCALab 220i-XL electron spectrometer from VG Scientific using 300 W Al Kα radiation.

Cell culture

Murine melanoma cell line B16F0 (called as B16) was supplied by KeyGEN Biotech. Co., Ltd. Cells were cultured in high-glucose DMEM supplemented with 10% (v/v) FBS and 1% antibiotics (penicillin/streptomycin, 100 U/mL) at 37 °C under a 5% CO_2 atmosphere.

Cytotoxicity assay

The cytotoxicity of materials was tested on B16 cells using a standard CCK-8 assay, as previously described. Cells were plated at a density of 1×10^4 /well in a 96-well cell culture plate at 37 °C under 5% CO_2 atmosphere for 24 h. The cells were treated with increasing concentrations (20, 40, 60, 80, 100 μM) of samples (100 μL/well) as treatment group, treated with free DMEM (100 μL/well) as control group for 24 h at 37 °C under a 5% CO_2 atmosphere respectively. Afterward, the cells were grown in a fresh DMEM for another 24 h. Then combined CCK-8/DMEM solution (10 μL/100 μL) was added to each well for additional 1 h incubation under the same condition. An enzyme-linked immunosorbent assay (ELISA) reader (infinite M20, Tecan, Austria) was used to measure the OD450 (Absorbance value) of each well. The following formula was used to calculate the viability of cell growth: Cell Viability (%) = [(As-Ab) / (Ac-Ab)] · 100%

Each independent experiment was performed in triplicate (As = OD value of treatment group, Ac = OD value of control group and the Ab = OD value of blank well).

Synthesis

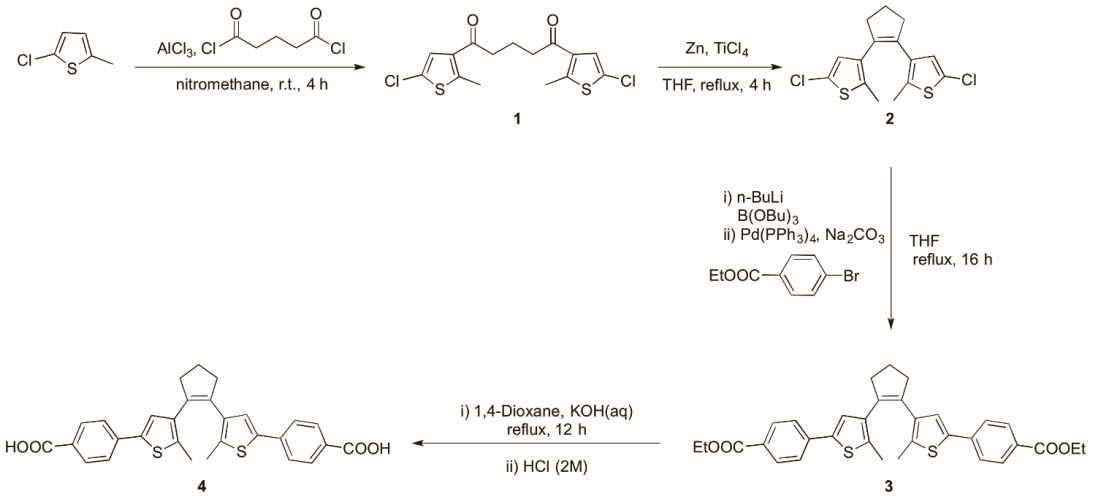

Scheme 5.1 Synthetic scheme of **BCDTE**.

1,5-Bis-3-(2-chloro-5-dimethylthienyl)-1,5-pentadione (1). To a mixture of 2-Chloro-5-methylthiophene (5 g, 37.7 mmol) and glutaryl chloride (3 g, 17.95 mmol) in nitromethane (150 mL) was added $AlCl_3$ (5.3 g, 39.5 mmol) under N_2 atmosphere at 0 °C. The solution was then stirred for 4 h at room temperature. Afterward, the reaction mixture was poured onto ice-water and the resulting mixture was extracted with CH_2Cl_2. The combined organic layers were dried over anhydrous $MgSO_4$, the solvent was removed in vacuo and the resulting crude product was purified by column chromatography (silica, hexanes: EtOAc = 30:1) to yield **1** as a light yellow solid (84%).^{1}H NMR (500 MHz, $CDCl_3$): δ = 7.18 (s, 2H), 2.86 (t, 4H), 2.66 (s, 6H), 2.06 (quin, 2H). ^{13}C NMR (125 MHz, $CDCl_3$): 194.9, 147.7, 134.9, 126.8, 125.3, 40.5, 18.1, 16.1.

1,2-bis(5-chloro-2-methylthiophen-3-yl)cyclopent-1-ene (2). $TiCl_4$ (3.9 g, 20.7 mmol) was dissolved cautiously in ice-cooled dry THF (200 mL) under N_2 atmosphere whereupon the solution turned yellow. To the mixture was added Zn powder (1.63 g, 25

mmol) and the resulting mixture was stirred for 45 min at 65 °C. Afterwards, the reaction was cooled to 0 °C with an ice bath and compound 1 (3 g, 8.3 mmol) was added and was reheated to 65 °C for 4 h. A few drops of saturated aq. K_2CO_3 solution was added to the mixture followed by filtration over Celite and washing with EtOAc, and the filtrate was dried over anhydrous $MgSO_4$. The crude product was purified by column chromatography (silica, pure hexanes) to afford **2** as a pale yellow solid (91%). ^{1}H NMR (500 MHz, $CDCl_3$): δ = 6.58 (s, 2H), 2.71(t, 4H), 2.02 (quin, 2H), 1.88 (s, 6H). ^{13}C NMR (125 MHz, $CDCl_3$): δ = 134.8, 134.4, 133.3, 126.7, 125.2, 38.3, 22.8, 14.2.

1,2-Bis(5-(4-ethyloxycarbonylphenyl)-2-methylthien-3-yl)cyclopent-1-ene (3). 1,2-bis(5-chloro-2-methylthiophen-3-yl)cyclopent-1-ene (**2**) (2.00 g, 6.07 mmol) was dissolved in 60 mL of anhydrous THF and *n*-BuLi (2.5 M in hexane, 6.56 mL, 16.40 mmol) was added dropwise at 0 °C. The solution was then stirred and warmed to room temperature for 30 min. Then, tri(n-butyl) borate (4.91 mL, 18.22 mmol) was added in one portion and the resulting mixture was stirred at room temperature for 1 h. In the meantime, ethyl 4-bromobenzoate (2.92 mL, 18.22 mmol) was dissolved in 20 mL of THF with $Pd(PPh_3)_4$ (0.70 g), and the mixture was stirred at room temperature for 15 min then heated to 80 °C. An aqueous solution of Na_2CO_3 (2 M, 50.0 mL) and the previously prepared solution of the borylated bisthienylcyclopentene were slowly added and the mixture was stirred at 80 °C for 16 h. After cooling to room temperature, 100 mL of water were added and the mixture was extracted with 50 mL of diethyl ether three times. The combined organic phases were washed with brine, dried over $MgSO_4$. Purification by column chromatography (silica, petroleum ether: EtOAc = 10:1) afforded compound **3**

(2.4 g, 71%) as a pale yellow solid. ^{1}H NMR (500 MHz, $CDCl_3$): δ (ppm) = 7.99 (d, 4 H), 7.53 (d, 4 H), 7.12 (s, 2 H), 4.37 (q, 4 H), 2.85 (t, 4 H), 2.10 (quin, 2H), 2.02 (s, 6 H), 1.40 (t, 6H). ^{13}C NMR (126 MHz, $CDCl_3$): δ (ppm) = 166.34, 138.57, 138.54, 137.01, 136.24, 134.77, 130.20, 128.63, 125.48, 124.82, 60.93, 38.48, 23.03, 14.59, 14.39.

1,2-Bis(5-(4-carboxyphenyl)-2-methylthien-3-yl)cyclopent-1-ene (4) (BCDTE). 1,2-Bis(5-(4-ethyloxycarbonylphenyl)-2-methylthien-3-yl)cyclopent-1-ene (**3**) (1.0 g, 1.8 mmol) was suspended in 160 mL 1,4-dioxane/H_2O (v:v = 1:1), and 2 g of KOH solution was added. The mixture was stirred overnight under reflux. The pH value was adjusted to ~pH 2 using 2 M HCl. The resulting white precipitate was collected by centrifugation, washed with water, and dried under vacuum to afford **BCDTE** (0.94 g, 99%). ^{1}H NMR (500 MHz, DMSO-d_6): δ (ppm) = 12.93 (s, 2H), 7.92 (d, 4H), 7.66 (d, 4H), 7.47 (s, 2H), 2.85 (t, 4 H), 2.07 (quin, 2H), 1.93 (s, 6H). ^{13}C NMR (126 MHz, DMSO-d_6): δ (ppm) = 166.93, 137.83, 137.66, 137.07, 135.36, 134.29, 130.21, 129.05, 126.05, 124.67, 38.12, 22.32, 14.16.

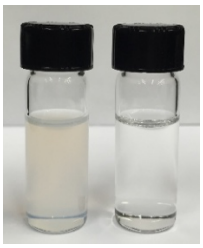

Figure 5.1 Products by addition of the starting materials together when dissolving (left) and addition of BA stock solution to the mixture of BDC and $ZrOCl_2 \cdot 8H_2O$ in DMF (right).

UiO-66 nanoparticles. Terephthalic acid (BDC) (15 mg, 0.09 mmol), zirconyl chloride octahydrate ($ZrOCl_2 \cdot 8H_2O$) (20 mg, 0.062 mmol), and benzoic acid (BA) (200 mg, 1.6 mmol) in 3 mL of *N,N*-dimethylformamide (DMF) were ultrasonically dissolved in a Pyrex vial. The reaction mixture was stirred (300 rpm) at 90 °C for 2.5 h. After the reaction is done, UiO-66 nanoparticles were collected by centrifugation (15000 rpm, 20 min) followed by washing with fresh DMF for 3 times. The resulting UiO-66 nanoparticles were suspended in DMF for further characterization and analysis.

Note: The sequence of adding starting materials was important to obtain nanoparticles. All starting materials had to be added together with other starting materials to yield UiO-66 nanoparticles (Fig. S1, left). When BDC and $ZrOCl_2 \cdot 8H_2O$ were dissolved and stayed longer than *ca.* 5 min before the addition of BA, the reaction did not form nanoparticles, but clear solution under given reaction condition (Fig. S1, right). Therefore, this finding was applied in the following syntheses as well.

Sample 1. H_2TCPP (0.5 mg, 0.0006 mmol), BDC (15 mg, 0.09 mmol), $ZrOCl_2 \cdot 8H_2O$ (20 mg, 0.062 mmol), and BA (200 mg, 1.6 mmol) in 3 mL of DMF were ultrasonically dissolved in a Pyrex vial. The reaction mixture was stirred (300 rpm) at 90 °C for 2.5 h. The oil bath was covered with aluminum foil to avoid lights. After the reaction is done, nanoparticles were collected by centrifugation (15000 rpm, 20 min) followed by washing with fresh DMF for 3 times. The resulting nanoparticles were suspended in DMF for further characterization and analysis.

Sample 2. H_2TCPP (0.5 mg, 0.0006 mmol), BCDTE (1 mg, 0.002 mmol), BDC (15 mg, 0.09 mmol), $ZrOCl_2 \cdot 8H_2O$ (20 mg, 0.062 mmol), and BA (200 mg, 1.6 mmol) in

3 mL of DMF were ultrasonically dissolved in a Pyrex vial. The reaction mixture was stirred (300 rpm) at 90 °C for 2.5 h. The oil bath was covered with aluminum foil to avoid lights. After the reaction is done, nanoparticles were collected by centrifugation (15000 rpm, 20 min) followed by washing with fresh DMF for 3 times. The resulting nanoparticles were suspended in DMF for further characterization and analysis.

Sample 3. H_2TCPP (0.5 mg, 0.0006 mmol), BCDTE (5 mg, 0.01 mmol), BDC (15 mg, 0.09 mmol), $ZrOCl_2 \cdot 8H_2O$ (20 mg, 0.062 mmol), and BA (200 mg, 1.6 mmol) in 3 mL of DMF were ultrasonically dissolved in a Pyrex vial. The reaction mixture was stirred (300 rpm) at 90 °C for 2.5 h. The oil bath was covered with aluminum foil to avoid lights. After the reaction is done, nanoparticles were collected by centrifugation (15000 rpm, 20 min) followed by washing with fresh DMF for 3 times. The resulting nanoparticles were suspended in DMF for further characterization and analysis.

Sample 4. H_2TCPP (0.5 mg, 0.0006 mmol), BCDTE (10 mg, 0.02 mmol), BDC (15 mg, 0.09 mmol), $ZrOCl_2 \cdot 8H_2O$ (20 mg, 0.062 mmol), and BA (200 mg, 1.6 mmol) in 3 mL of DMF were ultrasonically dissolved in a Pyrex vial. The reaction mixture was stirred (300 rpm) at 90 °C for 2.5 h. The oil bath was covered with aluminum foil to avoid lights. After the reaction is done, nanoparticles were collected by centrifugation (15000 rpm, 20 min) followed by washing with fresh DMF for 3 times. The resulting nanoparticles were suspended in DMF for further characterization and analysis.

Sample 5. H_2TCPP (0.5 mg, 0.0006 mmol), BCDTE (15 mg, 0.03 mmol), BDC (15 mg, 0.09 mmol), $ZrOCl_2 \cdot 8H_2O$ (20 mg, 0.062 mmol), and BA (200 mg, 1.6 mmol) in 3 mL of DMF were ultrasonically dissolved in a Pyrex vial. The reaction mixture was

stirred (300 rpm) at 90 °C for 2.5 h. The oil bath was covered with aluminum foil to avoid lights. After the reaction is done, nanoparticles were collected by centrifugation (15000 rpm, 20 min) followed by washing with fresh DMF for 3 times. The resulting nanoparticles were suspended in DMF for further characterization and analysis.

Sample 6. H_2TCPP (0.5 mg, 0.0006 mmol), BCDTE (20 mg, 0.04 mmol), BDC (15 mg, 0.09 mmol), $ZrOCl_2 \cdot 8H_2O$ (20 mg, 0.062 mmol), and BA (200 mg, 1.6 mmol) in 3 mL of DMF were ultrasonically dissolved in a Pyrex vial. The reaction mixture was stirred (300 rpm) at 90 °C for 2.5 h. The oil bath was covered with aluminum foil to avoid lights. After the reaction is done, nanoparticles were collected by centrifugation (15000 rpm, 20 min) followed by washing with fresh DMF for 3 times. The resulting nanoparticles were suspended in DMF for further characterization and analysis.

Sample 7. BCDTE (20 mg, 0.04 mmol), BDC (15 mg, 0.09 mmol), $ZrOCl_2 \cdot 8H_2O$ (20 mg, 0.062 mmol), and BA (200 mg, 1.6 mmol) in 3 mL of DMF were ultrasonically dissolved in a Pyrex vial. The reaction mixture was stirred (300 rpm) at 90 °C for 2.5 h. The oil bath was covered with aluminum foil to avoid lights. After the reaction is done, nanoparticles were collected by centrifugation (15000 rpm, 20 min) followed by washing with fresh DMF for 3 times. The resulting nanoparticles were suspended in DMF for further characterization and analysis.

Synthesis of large batch of samples. The syntheses can be scaled up to five times of that of the small batch scale while maintaining stoichiometry.

Table 5.1 Summary of synthetic conditions.

Samples	BDC (mg)	TCPP (mg)	BCDTE (mg)
UiO-66 NP	15	n/a	n/a
1	15	0.5	n/a
2	15	0.5	1
3	15	0.5	5
4	15	0.5	10
5	15	0.5	15
6	15	0.5	20
7	15	n/a	20

Transmission electron microscopy (TEM)

MOF nanoparticles were washed with fresh DMF three times to remove residual starting materials, then washed with pure water three time to remove excess DMF. The resulting samples were re-dispersed in water for the preparation. TEM images were taken on a JEOL JEM-2100F, operated at an acceleration voltage of 200 keV by dropping solution onto a carbon-coated copper grid. Image-Pro Plus software (version 5.1) was used to calculate the average size.

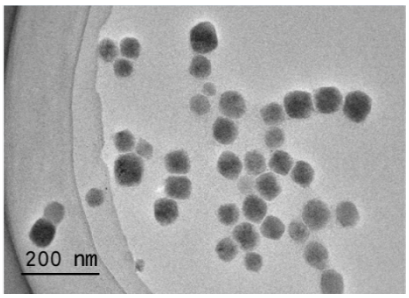

Figure 5.2 TEM image of UiO-66 nanoparticles. Scale bar = 200 nm.

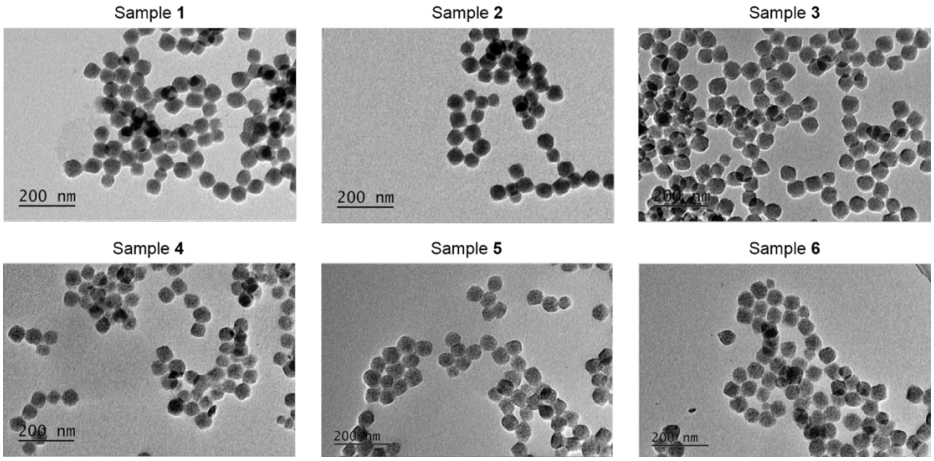

Figure 5.3 TEM images of samples **1** – **6**. Scale bars = 200 nm.

Scanning electron microscopy (SEM)

MOF nanoparticles were washed with fresh DMF three times to remove excess starting materials, then washed with pure water three times to remove excess DMF. The resulting samples were re-dispersed in water for preparation. SEM images were recorded on a Hitachi S4800 (Tokyo, Japan), operated at 10 keV by dropping solution onto a silicon wafer, then dried in air.

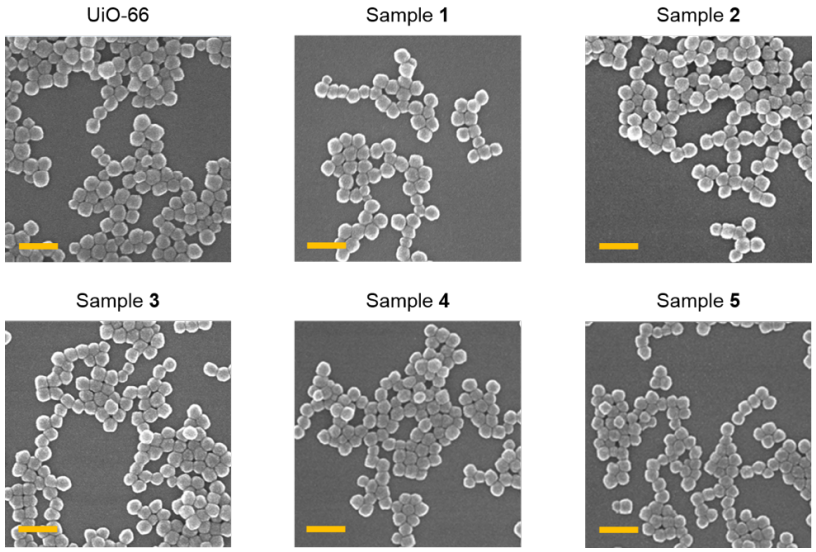

Figure 5.4 SEM images of UiO-66 nanoparticles and samples **1-6**. Scale bars = 200 nm.

Table 5.2 Summary of nanoparticle sizes from the TEM and SEM images.

Samples	TEM diameter (nm)	SEM diameter (nm)
UiO-66	62 ± 8	76 ± 6
1	52 ± 6	69 ± 5
2	49 ± 6	68 ± 4
3	53 ± 6	63 ± 4
4	48 ± 6	68 ± 4
5	48 ± 3	64 ± 4
6	48 ± 3	66 ± 4

DLS and ζ-potential measurement in water were conducted on a Zetasizer Nano ZS ZEN3600 analyzer (Malvern Instrument Ltd, UK) equipped with a 50 mW single laser diode (633 nm). Scattered light was detected at 165° and analyzed using a log correlator over 120 accumulations. The peak averages of histograms from number distributions out of 120 accumulations were reported as the Z-average diameters of the particles. The ζ-potential of the particles in suspension was obtained by measuring the electrophoretic movement of charged particles under an applied electric field. The ζ-potential was measured at twelve regions in the flow cell, and a weighted mean was calculated. These twelve measurements were used to correct for electro-osmotic flow that was induced in the cell due to the surface charge of the cell wall. Each sample was measured three times.

Table 5.3 Physiochemical properties of samples.

Samples	DLS (nm)	PDI	ζ potential (mV)
1	70 ± 19	0.080	31.6±6.90
2	68 ± 20	0.133	32.4±5.52
3	68 ± 19	0.122	35.6±6.70
4	68 ± 20	0.127	35.2±6.11
5	73 ± 20	0.076	35.0±6.24
6	65 ± 24	0.276	31.3±7.86

5.3 Results and discussion

While incorporation of the desired functional molecules as linkers of the MOF could be straightforward, there are several major obstacles to be applied in living cells for the desired $^1O_2$ control. First, porphyrin and DTE derivatives are not suitable for constructing stable MOFs, compatible in physiological environments owing to their large sizes.[202] Moreover, classical mixed-linker strategies to incorporate multiple functionalities often employ labile coordination bonds, resulting in an instability of the framework in aqueous media.[203] In particular, the mixed-linker strategy usually yields a locked ratio between pre-designed functional molecules in the framework when the linkers are not topologically identical,[31,204,205] which could inherently limit the tuning of the system for targeted application. Therefore, a system, where the ratio between photosensitizer and photochromic switch can be tuned in the MOF, is highly desired to optimize the controllability of $^1O_2$ generation.

We chose UiO-66 as a base platform to build a photosensitizing MOF system that can realize a reversible control of $^1O_2$ generation for PDT. As an archetype of Zr-MOF, UiO-66 exhibits excellent chemical stability through coordination bonds between high valent Zr^{IV} and carboxylate. [96,206] Meanwhile, 2,12-connected **fcu-a** net of UiO-66 allows for many sub-networks, including **bcu-a**, **reo-a**, **hxg-a**, or high-defect frameworks.[207-210] Accompanied with the reduced connectivity, available coordination sites on Zr_6 clusters $[Zr_6O_4OH_4(COO)_{12}]$ can be generated for the introduction of the functionalities via postsynthetic modification.[211] However, the narrow pore window and small pore size of UiO-66 hinder the entrance of large DTE and porphyrin derivatives into the framework

when postsynthetically approached. Therefore, we turned to an *in situ* insertion of these molecules into UiO-66 nanoparticles with a thermodynamic controlled synthesis.

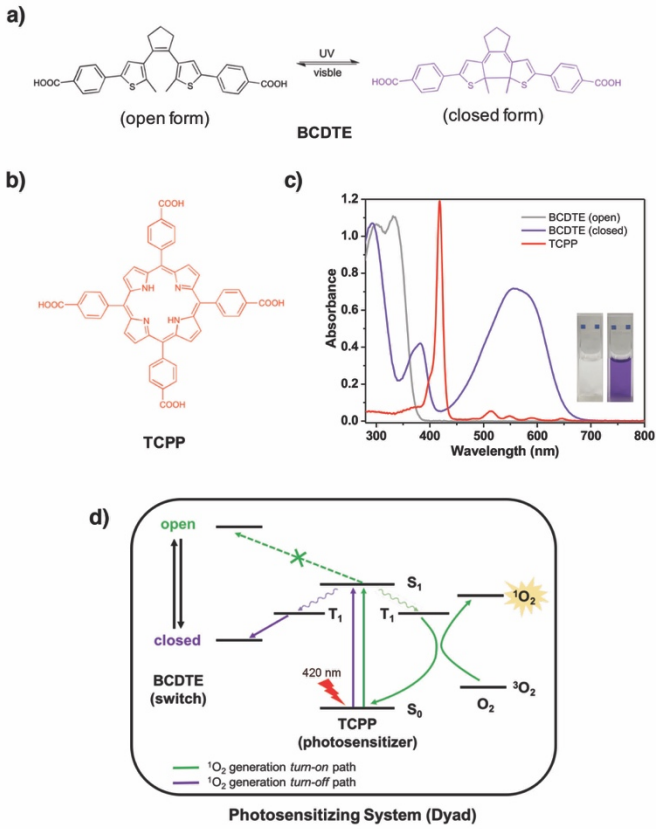

Figure 5.5 (a) Structures and photoisomerization of BCDTE and (b) structure of TCPP. (c) UV-Vis absorption spectra of BCDTE (30 μM) and TCPP (2 μM). Inset: photographs of BCDTE open (left) and closed (right) isomers. (d) Proposed scheme of $^1O_2$ control via competitive EnT pathways upon photoisomerization.

In order to incorporate the photosensitizing system (dyad), derivatization of DTE and porphyrin cores to 1,2-bis(5-(4-carbonxyphenyl)-2-methylthien-3-yl)cyclopent-1-ene (BCDTE) and a free-base tetrakis(4-carboxyphenyl)-porphyrin (TCPP) was implemented for their potential coordination to Zr_6 cluster (Figure 5.5a,b). Because the

energy transfer efficiency for switching on/off the $^1O_2$ generation is highly dependent on the molar ratios between the photosensitizer and photochromic switch,[161] we designed photosensitizing systems in UiO-66 nanocarriers (**1**–**6**) by increasing the feed ratio of the BCDTE switch at a constant amount of TCPP for fine-tuning of the photosensitization and switching ability.

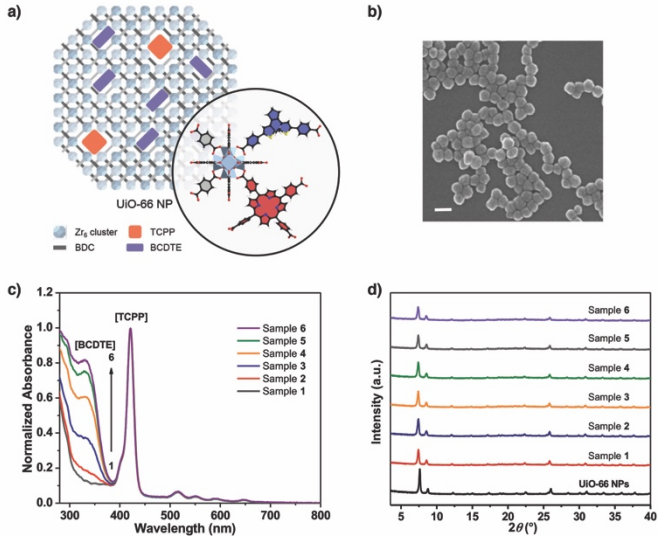

Figure 5.6 (a) Defective structure of UiO-66 with inserted TCPP and BCDTE, and a proposed binding scheme of TCPP and BCDTE on Zr_6 cluster. (b) SEM image of sample **6**. Scale bar = 100 nm. (c) UV-Vis absorption spectra of samples **1**–**6**, normalized at the same concentration of TCPP. (d) PXRD patterns of UiO-66 nanoparticles and samples **1**–**6**.

Interestingly, the optimized synthetic condition modified from the reported synthesis of UiO-66 nanoparticles, [212,213] where TCPP and BCDTE were simply added with other starting materials, could produce a pure phase of UiO-66 nanoparticles rather than a mixture of different MOFs (Figure 5.6). It is reasoned that the superior

thermodynamic stability of UiO-66 inhibits possible formation of BCDTE-Zr-MOF, while the growth of TCPP-Zr-MOF, despite its high thermodynamic stability, was controlled by the low dose of TCPP.[214] Therefore, the single phase of UiO-66 can be targeted regardless of the complexity of the system. Meanwhile, both TCPP and BCDTE, containing multiple carboxylates, can readily participate in the coordination of Zr_6 clusters by partially substituting terephthalate linkers during the growth of UiO-66 (Figure 5.6a). Once TCPP and BCDTE were installed inside the framework, the "ship-in-a-bottle" effect resulting from the small pore windows of UiO-66 and the robustness Zr-COO bonds can prevent the leaching of the inserted functionalities, thus maintaining the desired ratio after the synthesis.[215] More importantly, since TCPP and BCDTE are not serving as the linkers, our design allows for tuning the molar ratios between two dyes upon varying synthetic conditions, as well as the proximity of the dyes within the MOF nanoparticle for efficient energy transfer.

Table 5.4 UV-Vis spectroscopically determined ratios between BCDTE/TCPP in samples (**1**–**6**).

Samples	BCDTE/TCPP Ratio
1	n/a
2	1.0
3	4.2
4	8.1
5	10.5
6	11.4

TEM and SEM images of **1**–**6** show approximately 70 nm of spherical nanoparticles with a high uniformity and a narrow size distribution (Figure 5.6b and Figures 5.2-5.4). After confirming the phase purity of **1**–**6** (Figure 2d), the ratio between

BCDTE and TCPP in each sample was then determined by UV/Vis spectra (Table 5.4). Adjustable ratios of the incorporated molecules were further confirmed by XPS and EDS data (Tables 5.5,5.6). The homogeneity of the dyad in the samples was also confirmed by UV/Vis spectroscopy showing linear responses of each compound in the MOF (Figure 5.7) and TEM/EDS mapping results (Figure 5.8).

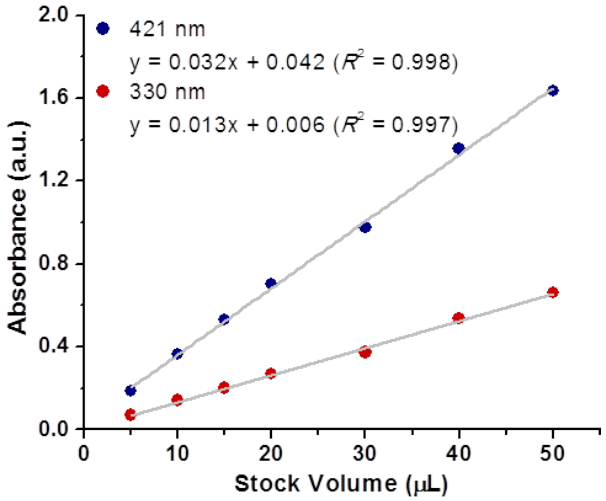

Figure 5.7 Absorbance of BCDTE (λ_{abs} = 330 nm) and TCPP (λ_{abs} = 421 nm) in **3**, respectively, as a function of stock volume of **3**.

Table 5.5 Contents of S and Zr in the samples from EDX characterization.

Samples	S (Atomic%)	Zr (Atomic%)	S/Zr Ratio
1	0.03±0.03	4.40±0.46	0.007±0.006
2	0.06±0.01	4.24±0.35	0.014±0.001
3	0.22±0.06	4.10±0.23	0.054±0.012
4	0.36±0.12	3.48±0.94	0.100±0.009
5	0.60±0.11	4.39±0.36	0.136±0.013
6	0.61±0.10	3.67±0.49	0.166±0.007

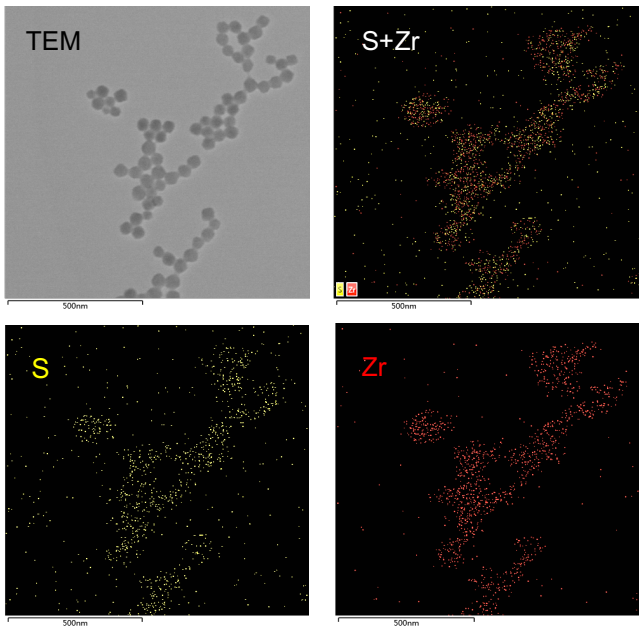

Figure 5.8 TEM/EDS mapping of sample **6**. Scale bars = 500 nm.

Table 5.6 Summary of XPS results. Contents of S2p, N1s and Zr3d in samples (**1**-**6**).

Samples	S2p (Atomic %)	N1s (Atomic %)	Zr3d (Atomic %)	S/Zr Ratio
1	0.1	1.51	5.35	~0.02
2	0.3	1.44	5.39	~0.06
3	0.52	1.58	4.94	~0.11
4	0.77	1.3	4.96	~0.16
5	0.85	1.44	4.53	~0.19
6	1	1.46	4.7	~0.21

The $^1O_2$ generation controllability of the photosensitizing systems **1**–**6** was tested upon photoisomerization. A proposed mechanism for the control of $^1O_2$ generation is centered on competitive energy transfer pathways of TCPP emission between closed BCDTE and $^3O_2$ (Figure 5.5d). Representative photoisomerization of BCDTE isomers was shown in Figure 5.5c, exhibiting distinctive changes in absorption profile. Depending on the form of BCDTE isomers, therefore, the excited energy of TCPP can take different

energy transfer routes as shown in Figure 5.5d. For instance, when the BCDTE switch is in the open form, the energy transfer occurs from ^{3}TCPP* to $^3O_2$, resulting in $^1O_2$ generation.[161] On the other hand, the closed BCDTE upon UV irradiation quenches the $^1O_2$ generation due to possible EnT pathway to the closed BCDTE over $^3O_2$. To validate the feasibility of photoisomerization of BCDTE in UiO-66 nanoparticles, we prepared a sample only with BCDTE in UiO-66 (**7**) using the same synthetic strategy. Upon UV irradiation (λ=302 nm) on the open form of BCDTE at UiO-66, the maximum absorbance of BCDTE was observed in 10-15 s, while prolonged UV irradiation led to a decrease in absorbance (Figure 5.10a). The reverse reaction was also tested with a visible irradiation (λ>450 nm) and a near complete recovery was achieved in 15 min (Figure 10b). It is worth noting that sample **7** shows much faster photoisomerization than that of other reported MOFs in which the photochromic molecules were incorporated as the linker.[186,216,217] Knowing this, sample **6** was also tested for the photoisomerization. The reversible photoisomerization was clearly observed on a similar time frame while showing characteristic bands of both TCPP and BCDTE (Figure 5.9).

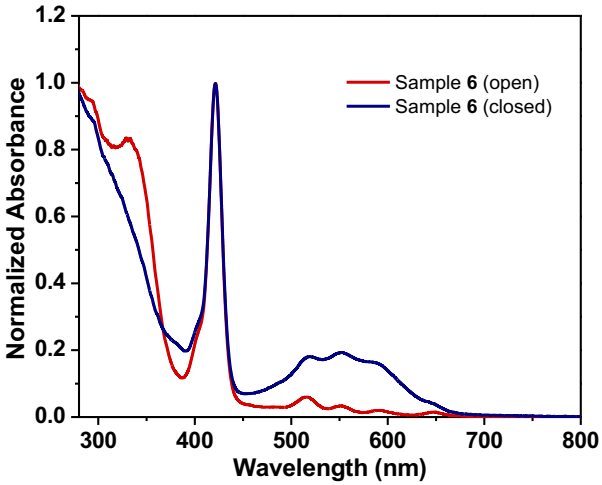

Figure 5.9 UV-Vis absorption spectra of open and closed isomers of **6**.

Because the emission of TCPP could strongly indicate the results of proposed energy transfer, the viability of regulating energy transfer pathways in our system was then evaluated by fluorescence spectroscopy. The photosensitizing system **6** was chosen because the highest ratio of BCDTE over TCPP would result in the greatest quenching ability. The system was excited at the Soret band (λ=420 nm) of TCPP to avoid possible intervention of the switching operation. The emission spectrum of **6** with the open switch (denoted as **6-o**) shows an emission maximum at 650 nm. To this sample, UV irradiation was applied to close the BCDTE switch in **6**. As expected, the emission at 650 nm was quenched upon UV irradiation, suggesting energy transfer occurred to the closed BCDTE as proposed (Figure 5.10c). Reverse photoisomerization of BCDTE was subsequently carried out with visible irradiation (λ>450 nm), and a recovery of emission was achieved in 15 min, consistent with UV/Vis spectroscopic studies. Next, reversibility of the system was monitored by recording changes in emission intensity at 650 nm by alternating cycles of switching on/off. Slight loss of fatigue resistance was observed as cycles proceeded,

which may be attributed to the substituent effect on DTE switch as studied in literature.[218] Nevertheless, in system **6**, the BCDTE to TCPP ratio can be as high as around 11:1, in which the emission of TCPP can be sufficiently quenched by a high concentration of the closed form of BCDTE.

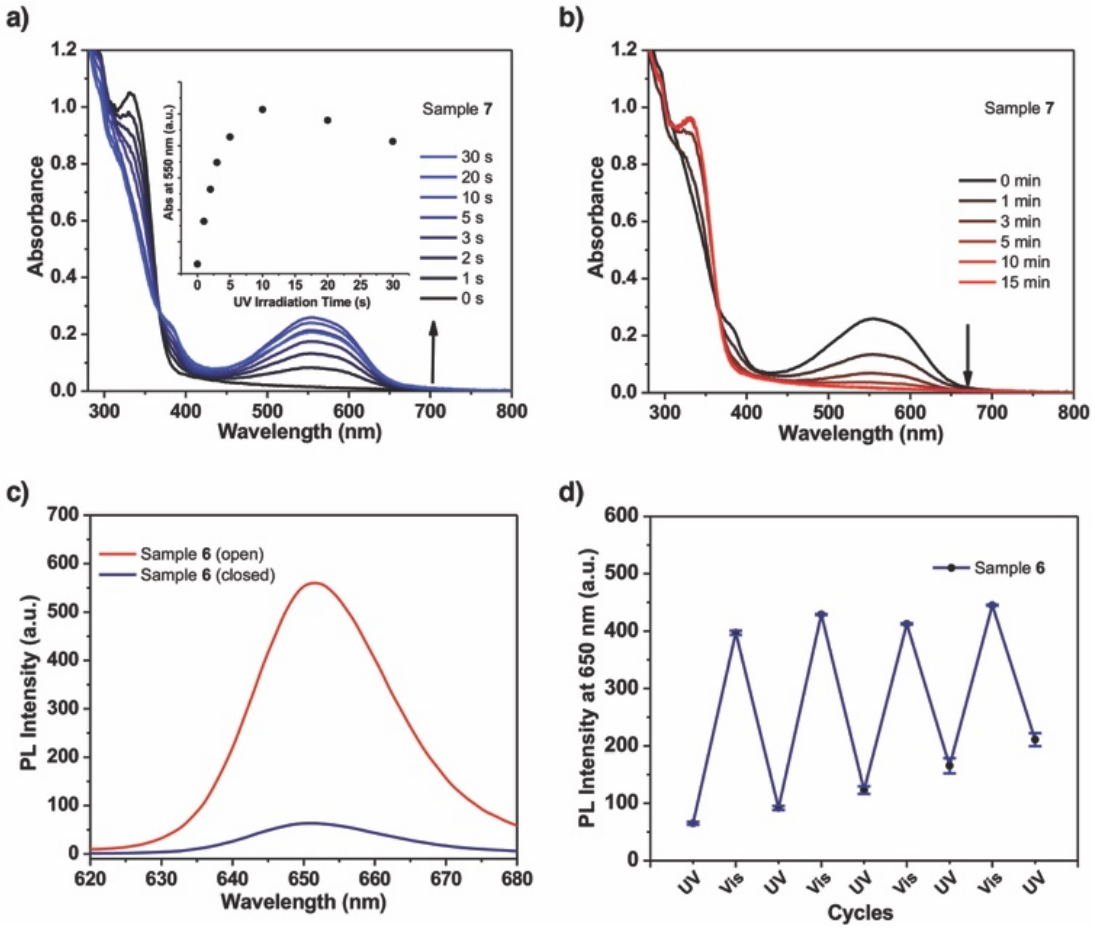

Figure 5.10 (a) Changes in the UV-Vis absorption of sample **7** upon UV irradiation at 302 nm and (b) recovery of UV-Vis absorption of **7** upon visible irradiation ($\lambda > 450$ nm with long pass filter) in DMF. (c) Emission spectra of open and closed isomers of **6**. λ_{ex} = 420 nm. (d) Changes in emission intensity of **6** at 650 nm over few cycles of photoisomerization. λ_{ex} = 420 nm.

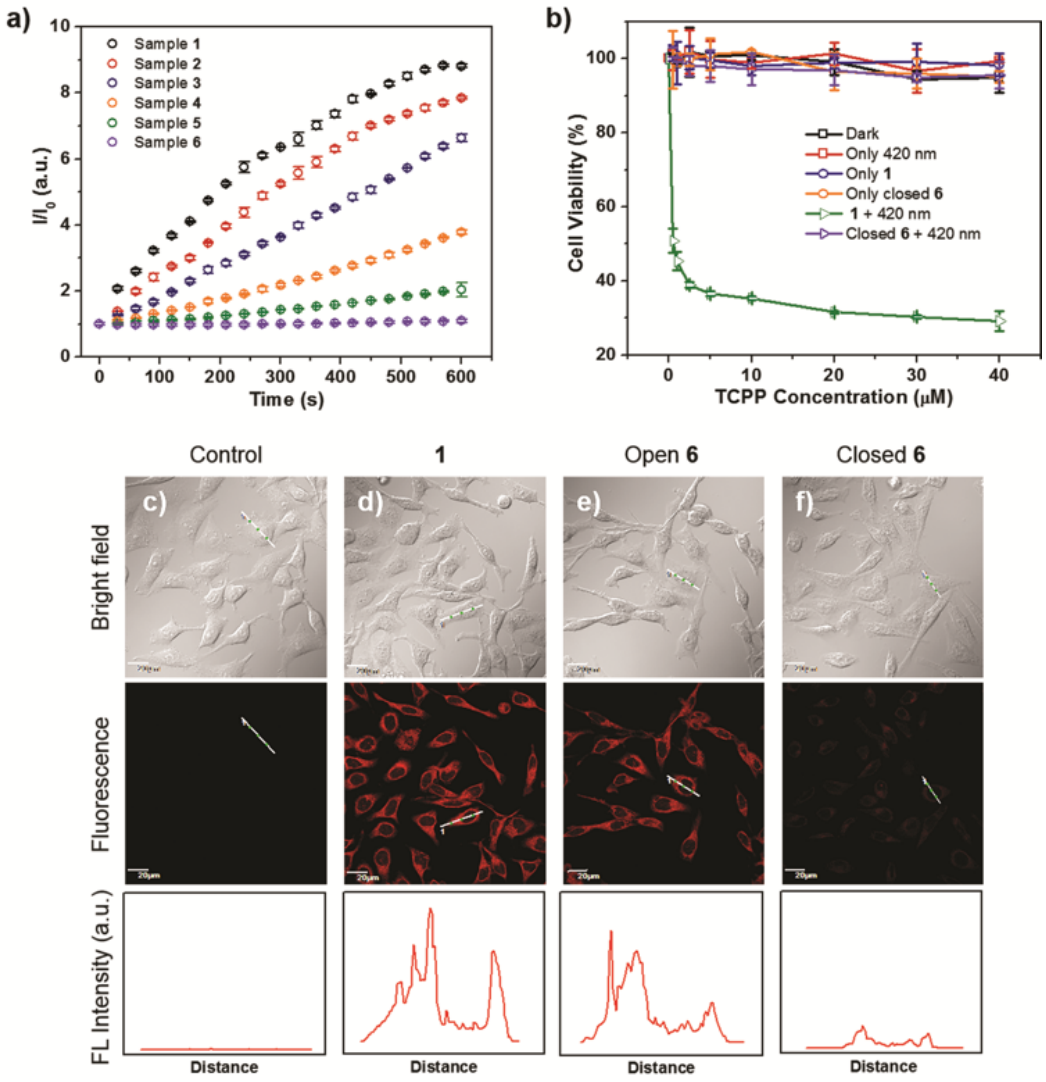

Figure 5.11 (a) Irradiation time-dependent SOSG fluorescence response incubated with the closed form of samples **1**–**6** upon 420 nm irradiation for photosensitization. λ_{ex} = 504 nm, λ_{em} = 550 nm. (b) *In vitro* PDT efficacy of sample **1** and **6-c** at various concentrations in B16 melanoma cells. Incubation time = 24 h. Irradiation time = 30 min. c-f) CLSM images of B16 cells treated with 20 μM of samples **1** and **6**, respectively (middle row). Cells treated with (c) FBS free DMEM as a control; (d) sample **1**; (e) sample **6-o**; (f) sample **6-c** for 60 min, respectively. The corresponding DIC images are shown at top row. Fluorescence intensity profiles within the line across B16 cells are shown at bottom row. Scale bars = 20 μm.

After validating the reversible nature, [BCDTE]-dependent $^1O_2$ controllability was then examined with the closed form of BCDTE in each sample to compare the quenching efficiency of $^1O_2$ generation. The generated $^1O_2$ was monitored by turn-on fluorescence of singlet oxygen sensor green (SOSG). Samples **1**–**6** (closed forms) were irradiated by 420 nm (100 mW/cm^2) to generate $^1O_2$. As expected, the $^1O_2$ quenching efficiency was proportional to the concentration of BCDTE switch in each system (Figure 5.11a). In particular, **6** showed almost a near complete quenching of $^1O_2$ upon turn-off operation, suggesting energy transfer to $^3O_2$ was indeed more efficiently inhibited by the higher concentration of the closed BCDTE in **6**.

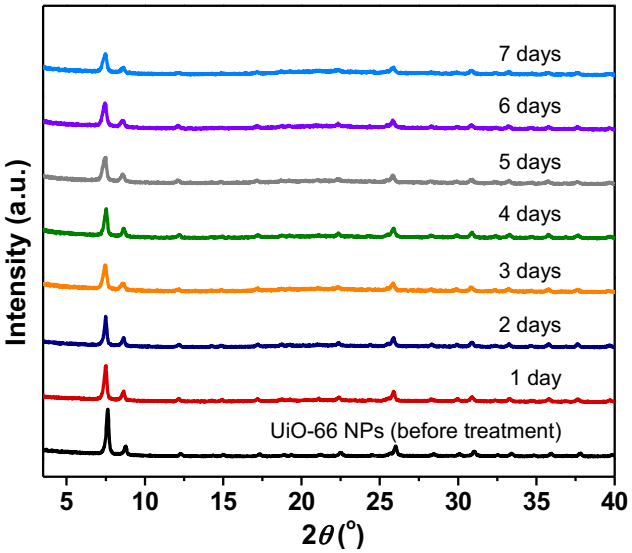

Figure 5.12 PXRD patterns of UiO-66 nanoparticle soaked in HEPES buffer (0.01 M, pH 7.4, 37 °C).

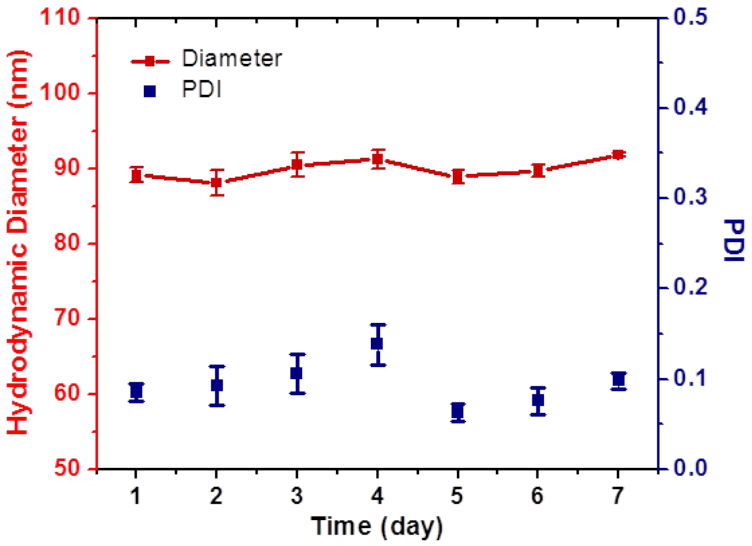

Figure 5.13 Colloidal stability of UiO-66 nanoparticles in water for seven days. Cumulant results were recorded for hydrodynamic meter. Data are means ± s.d. (N = 3).

Having confirmed their $^1O_2$ controllability as well as effective photosensitization, we then evaluated the applicability of the systems in live cells. First, stability of the nanocarrier was examined in aqueous media where PXRD and dynamic light scattering (DLS) data showed no obvious destruction of the framework over a week (Figures 5.12 and 5.13). In vitro PDT studies were then carried out using B16 melanoma cells, a skin cancer model. Imaging capability of the material was examined by **1**, composed of only TCPP in UiO-66 nanoparticles, showing a strong red fluorescence, indicative of the emission from the photosensitizer (Figure 5.11d). Next, B16 cells were treated with **6-o** (the same TCPP equiv), exhibiting red emission as intense as **1**, which suggests the excited energy of TCPP was not disturbed by the open switch in **6** (Figure 5.11e). Switching ability of **6** was then validated by the cells incubated with the closed **6** (denoted as **6-c**), which shows a negligible fluorescence as a result of the proposed energy transfer to the closed

form of BCDTE (Figure 5.11f). In addition, cell viability tests show low cytotoxicity of materials **1–6** to B16 cells at various concentrations for as long as 48 h (Figure 5.14).

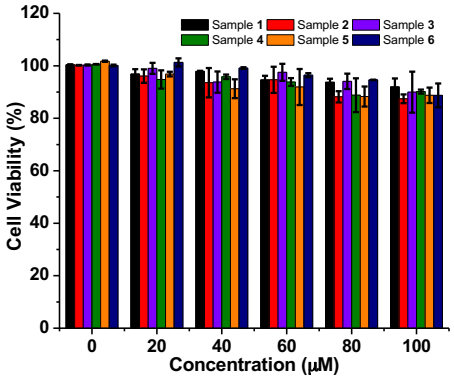

Figure 5.14 Cell viability of B16 cells incubated with samples (**1-6**) at various concentrations for 48 h. Data are means ± s.d. N = 3.

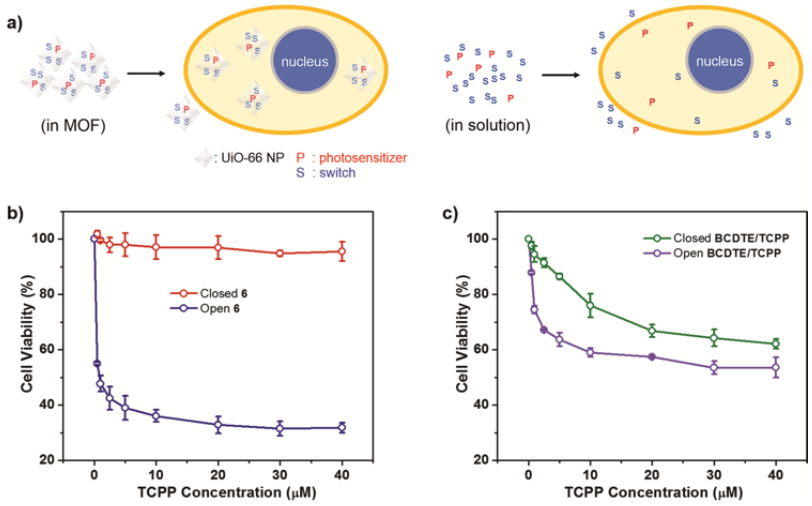

Figure 5.15 (a) Proposed delivery of the photosensitizing system (BCDTE and TCPP) via MOF nanoparticle formulation (left) and a mixture of small molecules in solution (right). (b) Comparison of *in vitro* PDT efficacy between **6-c** and **6-o** at various concentrations in B16 cells upon irradiation at 420 nm. Incubation time = 24 h. Irradiation time = 30 min. (c) Comparison of *in vitro* PDT efficacy between open and closed forms of free BCDTE/TCPP mixture at various concentrations in B16 cells upon irradiation at 420 nm. Incubation time = 24 h. Irradiation time = 30 min.

Next, in vitro PDT efficacy was examined in B16 melanoma cells. While various control groups showed no apparent phototoxicity, sample **1** showed a significant PDT efficacy (Figure 5.11b). In particular, the cells treated with **6-c** showed almost no PDT efficacy, clearly supporting our hypothesis that energy transfer-based control of $^1O_2$ generation was indeed realized in cell model (Figure 5.11b). To further confirm this concept, we directly compared PDT efficacy between **6-c** and **6-o**. As shown in Figure 5b, the PDT results indicate that switching operation can turn on $^1O_2$ generation in **6-o**, enabling desired control of $^1O_2$ for PDT through the photochromic switch. As a control experiment, the switching ability and ensuing PDT efficacy of a homogeneous mixture of BCDTE and TCPP molecules (without MOF nanoparticle formulation) were tested at the same concentrations as those in **6**. Interestingly, PDT efficacy of the small molecule system (open BCDTE/TCPP mixture) was less effective than that of **6-o**, further supporting the improved PDT efficacy by enhanced permeability and retention (EPR) effect, of which the improved delivery was achieved by the UiO-66 nanocarrier (Figure 5.15b,c). In particular, the results indicate that delivery of the mixture to target cells with their optimized molar ratio might be challenged presumably due to biological barriers (e.g., different cell permeability), suggested by noticeable loss of $^1O_2$ control (green in Figure 5.15c). Furthermore, the failure of maintaining effective local concentration of the homogeneous mixture of the dyad in the cells may also result in a significantly diminished control for $^1O_2$ quenching (Figure 5.15a). Therefore, in situ incorporation of multiple functionalities in MOF nanoparticle not only enhanced the delivery and PDT efficacy of the photosensitizing system over the molecular analogues, but also can be an attractive

strategy to maintain the pre-designed system with multiple components (i.e., the optimized ratio) for desired applications.

5.4 Conclusions

In summary, our strategy of the in situ incorporation of the multiple functionalities in the MOF nanoparticle has been successfully demonstrated with a tunable ratio of the photochromic switch for the control of $^1O_2$ generation. This method also shows great potential for protected delivery of an integrated photosensitizing system as desired, allowing enhanced in vitro PDT efficacy with superior controllability of $^1O_2$ generation, using a MOF formulation compared to that of homogeneous mixture of the dyad.

6. SIZE-CONTROLLED SYNTHESIS OF PORPHRYINIC METAL–ORGANIC FRAMEWORK AND FUNCTIONALIZATION FOR TARGETED PHOTODYNAMIC THERAPY*

6.1 Introduction

Nanotechnology has shown great potential for cancer treatment due to the unique properties of nanomaterials, including optical, electrical, and magnetic behaviors. Meanwhile understanding the interactions between the nanomaterials and biological systems with respect to their size, shape, and surface chemistry is of significant importance when designing nanomaterials to improve the precision of cancer therapy.[219-222] Current nanomaterials in cancer therapy have evolved to improve specific accumulation at the tumor site with two major mechanisms: passive and active targeting. Passive targeting is often referred to as the enhanced permeability and retention (EPR) effect, while active targeting is achieved by coating targeting ligands onto the nanomaterials that can promote cellular uptake at the tumor sites.[223,224]

With conventional nanomaterials, however, achievement of such targeting modalities is often complex, because nanomaterials are usually employed as carriers of therapeutics or imaging agents, of which their inherent traits are hardly modifiable at a molecular level.[196] Recent studies reveal that physical parameters of nanomaterials have shown a strong correlation to cellular processes.[225-230] However, engineering of

*Reproduced with permission from Park, J.; Jiang, Q.; Feng, D.; Mao, L.; Zhou, H.-C., *J. Am. Chem. Soc.,* **2016**, *38,* 3518–3525. Copyright 2016 American Chemical Society.

nanoparticles to carry a single variable for studying a targeted parameter remains a daunting challenge with formulations of conventional nanoparticles, because these often depend on more than one single factor.[231] Thus, such systems could disturb interpretation of the pure effects of the targeted parameter under controlled conditions, against other dependent variables. Therefore, it is of critical importance to integrate functionality into materials while having controllability of size and shape with no significant alteration of their designed physicochemical properties, as well as with a high degree of uniformity.[231-233]

As an emerging modality of cancer treatments, photodynamic therapy (PDT) has gained attention due to its minimally invasive nature and innate selectivity upon a localized irradiation at the tumor sites.[187,234] PDT requires a combination of light, a photosensitizer (PS), and tissue oxygen to generate cytotoxic singlet oxygen ($^1O_2$) that can damage tumors. Although porphyrin derivatives are widely employed photosensitizers in PDT, the effective delivery of porphyrinic molecules to the tumor sites still leaves much to be desired due to their hydrophobic nature.[195] Alternatively, nanomaterials have been involved as carriers for PDT therapeutics, but these examples often show limitations of imprecise control of loading, increased toxicity, leaching, and instability.[232,235,236] As an emerging class of porous materials, metal–organic frameworks (MOFs) have earned a significant amount of attention due to their superior design flexibility from their components of organic linkers and inorganic building blocks.[1,237] Despite broad interest in the synthesis of new MOFs, formulations of MOFs as nanomaterials have been relatively underdeveloped but a few synthetic methods (e.g., microwave, modulating

chemical, spray-drying) have been applied.[213,238-240] Thus, expanding the study of nanomaterials with the design flexibility of MOFs at a molecular level can greatly diversify the core function of nanoparticles, broadening the scope of applications beyond the traditional use of their pores as carriers.[13,197,241-246] For instance, MOFs can integrate photosensitizers in periodic arrays, significantly reducing quenching of excited energy in a minimal volume, while allowing the accessibility of substrates due to their porous features. [25,177,198] In that regard, having MOFs as a base platform of nanomaterials can be advantageous due to their structural and chemical tunability via a bottom-up design. Here we show size-dependent targeted photodynamic therapy with porphrynic Zr-MOF nanoparticles, PCN-224. The size-dependent cellular uptake and ensuing PDT were studied with various sizes of PCN-224 nanoparticles with an imaging and a therapeutic modality from the porphyrinic linker. In addition, further functionalization with folic acid (FA) onto the Zr_6 cluster in the MOF was also demonstrated, showing enhanced PDT efficacy owing to the active targeting of the modified MOF nanomaterial.

6.2 Experimental section

Materials

Folic acid and 4-(2-Hydroxyethyl) piperazine-1-ethanesulfonic acid (HEPES) were purchased from Sigma-Aldrich. Tetrakis(4-carboxyphenyl)porphyrin (H_2TCPP) was purchased from Frontier Scientific. Dulbecco's modified Eagle medium (DMEM/HIGH GLUCOSE 1X) were purchased from HyClone, GE Life Sciences. Fetal bovine serum (FBS) was purchased from Gibco, Thermo Fisher Scientific. Cell culture reagents were purchased from Invitrogen. Cell Counting Kit-8 (CCK-8) and Mito Tracker Green FM dye

were obtained from Beyotime Institute of Biotechnology (Beijing, China). Hoechst 33342 was obtained from Solarbio (Beijing, China). Lyso Tracker Green DND-26 and Singlet Oxygen Sensor Green were purchased from life technologies (USA). Other chemicals were of at least analytical grade and were used as received. All aqueous solutions were prepared with Milli-Q water generated from a Milli-pore system (Bedford, MA). All other not mentioned starting materials and solvents were used as received without further purification from the following suppliers (Alfa Aesar, Sigma-Aldrich, TCI America, Cambridge Isotope, Oakwood Products, Fisher Scientific). The abbreviation for some solvents and reagents were listed here: *N,N*-dimethylformamide (DMF), and dimethylsulfoxide (DMSO).

Instrumentation

Synthetic manipulations that required an inert atmosphere (where noted) were carried out under nitrogen using standard Schlenk techniques. Powder X-ray diffraction (PXRD) was carried out on a Bruker D8-Focus Bragg-Brentano X-ray powder Diffractometer equipped with a Cu sealed tube (λ = 1.54178) at 40 kV and 40 mA. N_2 sorption isotherms at 77 K were measured by using a Micrometritics ASAP 2420 system with high-purity grade (99.999%) of gases. UV-Vis spectra were recorded on Shimadzu UV-2450 spectrophotometer and TU-1900 spectrophotometer (Beijing Purkinje General Instrument Co. Ltd., China). Fluorescence spectra were recorded on a Hitachi F-4600 spectrometer (Hitachi Co. Ltd., Japan) with Xe lamp as the excitation source at room temperature. Dynamic light scattering and Zeta potential were measured at 25 °C on a Zetasizer Nano ZS ZEN3600 analyser (Malvern Instrument Ltd, UK). Singlet oxygen was

generated from a CEL-S500 xenon lamp (Ceaulight, Beijing) with separate passing filter (power density was 100 mW/cm^2). Confocal laser scanning microscopy (CLSM) images were performed on an Olympus FV1000-IX81 CLSM and a Leica TCS SP confocal system (Leica, Germany). Inductively coupled plasma mass spectrometry (ICP-MS) was carried out on an Agilent 7700x series ICP-MS instrument. TEM images were taken on a transmission electron microscopy (JEOL JEM-2100F, Japan) operated at an acceleration voltage of 200 keV by dropping solution onto a carbon-coated copper grid.

Cell culture

Human cervical carcinoma cell line (HeLa cells) and human lung adenocarcinoma cell line (A549 cells) were supplied by Peking Union Medical College Hospital (Beijing, China). Cells were cultured in high-glucose DMEM supplemented with 10% (v/v) FBS and 1% antibiotics (penicillin/streptomycin, 100 U/mL) at 37 °C under a 5% CO_2 atmosphere.

ICP-MS analysis

Inductively coupled plasma mass spectrometry (ICP-MS) was carried out on an Agilent 7700x series ICP-MS instrument. Cells were cultured in 35 mm glass-bottomed dishes at a density of $1.0x10^6$/well. After incubation with different concentrations of PCN224 nanoparticles for certain time, the cells were digested with 0.25% pancreatin at 37 °C for 60 seconds and centrifuged at 2000 rpm for 5 min. Precipitations were lysed in nitric acid at 200 °C for 1 h, then re-suspended in 5% nitric acid overnight for the preparation. For ICP-MS analysis, 20 μL of the cell lysates was diluted to 2 mL with Milli-Q water. ICP-MS calibration standards was used for preparing the calibration curves, of

which Zr^{4+} concentrations were 0, 0.01, 0.1, 1, and 10 ppb (μg/mL). The isotope detected was ^{90}Zr, and the readings were made in He gas mode.

Synthesis of single crystalline PCN-224

Single crystalline PCN-224. 5,10, 15, 20 -Tetrakis (4-carboxyphenyl)porphyrin (H_2TCPP) (10 mg, 0.013 mmol), zirconyl chloride octahydrate ($ZrOCl_2 \cdot 8H_2O$) (30 mg, 0.093 mmol), and benzoic acid (BA) (300 mg, 2.4 mmol) in 2 mL of *N,N*-Dimethylformamide (DMF) were ultrasonically dissolved in a Pyrex vial. The reaction mixture was heated in the 120 °C oven for 24 h. After cooling down to room temperature, dark purple crystals were harvested by filtration.

Variation of DMF

80 mL DMF sample. H_2TCPP (100 mg, 0.13 mmol), $ZrOCl_2 \cdot 8H_2O$ (300 mg, 0.93 mmol), and benzoic acid (2.8 g, 23 mmol) were dissolved in *80 mL* of DMF in a 250 mL round bottom flask and the mixture was stirred (300 rpm) at 90 °C for 5 h. After the reaction is done, PCN-224 nanoparticles were collected by centrifugation (15000 rpm, 30 min) followed by washing with fresh DMF for 3 times. The resulting PCN-224 nanoparticles were suspended in DMF for further characterization and analysis.

100 mL DMF sample (reference condition). H_2TCPP (100 mg, 0.13 mmol), $ZrOCl_2 \cdot 8H_2O$ (300 mg, 0.93 mmol), and benzoic acid (2.8 g, 23 mmol) were dissolved in *100* mL of DMF in a 250 mL round bottom flask and the mixture was stirred (300 rpm) at 90 °C for 5 h. After the reaction is done, PCN-224 nanoparticles were collected by centrifugation (15000 rpm, 30 min) followed by washing with fresh DMF for 3 times. The

resulting PCN-224 nanoparticles were suspended in DMF for further characterization and analysis.

120 mL DMF sample. H_2TCPP (100 mg, 0.13 mmol), $ZrOCl_2 \cdot 8H_2O$ (300 mg, 0.93 mmol) and benzoic acid (2.8 g, 23 mmol) were dissolved in *120 mL* of DMF in a 250 mL round bottom flask and the mixture was heated at 90 °C for 5 h under stirring. After the reaction is done, PCN-224 nanoparticles were purified by centrifugation (15000 rpm, 30 min) followed by washing with fresh DMF for 3 times. The resulting PCN-224 nanoparticles were suspended in DMF for further characterization and analysis.

140 mL DMF sample. H_2TCPP (100 mg, 0.13 mmol), $ZrOCl_2 \cdot 8H_2O$ (300 mg, 0.93 mmol), and benzoic acid (2.8 g, 23 mmol) were dissolved in *140 mL* of DMF in a 250 mL round bottom flask and the mixture was stirred (300 rpm) at 90 °C for 5 h. After the reaction is done, PCN-224 nanoparticles were collected by centrifugation (15000 rpm, 30 min) followed by washing with fresh DMF for 3 times. The resulting PCN-224 nanoparticles were suspended in DMF for further characterization and analysis.

Variation of benzoic acid

2.2 g benzoic acid sample. H_2TCPP (100 mg, 0.13 mmol), $ZrOCl_2 \cdot 8H_2O$ (300 mg, 0.93 mmol), and benzoic acid (*2.2 g*, 18 mmol) were dissolved in 100 mL of DMF in a 250 mL round bottom flask and the mixture was stirred (300 rpm) at 90 °C for 5 h. After the reaction is done, PCN-224 nanoparticles were collected by centrifugation (15000 rpm, 30 min) followed by washing with fresh DMF for 3 times. The resulting PCN-224 nanoparticles were suspended in DMF for further characterization and analysis.

2.6 g benzoic acid sample. H_2TCPP (100 mg, 0.13 mmol), $ZrOCl_2 \cdot 8H_2O$ (300 mg, 0.93 mmol), and benzoic acid (*2.6 g*, 21 mmol) were dissolved in 100 mL of DMF in a 250 mL round bottom flask and the mixture was stirred (300 rpm) at 90 °C for 5 h. After the reaction is done, PCN-224 nanoparticles were collected by centrifugation (15000 rpm, 30 min) followed by washing with fresh DMF for 3 times. The resulting PCN-224 nanoparticles were suspended in DMF for further characterization and analysis.

2.8 g benzoic acid sample. H_2TCPP (100 mg, 0.13 mmol), $ZrOCl_2 \cdot 8H_2O$ (300 mg, 0.93 mmol), and benzoic acid (*2.8 g*, 23 mmol) were dissolved in 100 mL of DMF in a 250 mL round bottom flask and the mixture was stirred (300 rpm) at 90 °C for 5 h. After the reaction is done, PCN-224 nanoparticles were collected by centrifugation (15000 rpm, 30 min) followed by washing with fresh DMF for 3 times. The resulting PCN-224 nanoparticles were suspended in DMF for further characterization and analysis.

3.0 g benzoic acid sample. H_2TCPP (100 mg, 0.13 mmol), $ZrOCl_2 \cdot 8H_2O$ (300 mg, 0.93 mmol), and benzoic acid (*3.0 g*, 24 mmol) were dissolved in 100 mL of DMF in a 250 mL round bottom flask and the mixture was stirred (300 rpm) at 90 °C for 5 h. After the reaction is done, PCN-224 nanoparticles were collected by centrifugation (15000 rpm, 30 min) followed by washing with fresh DMF for 3 times. The resulting PCN-224 nanoparticles were suspended in DMF for further characterization and analysis.

3.3 g benzoic acid sample. H_2TCPP (100 mg, 0.13 mmol), $ZrOCl_2 \cdot 8H_2O$ (300 mg, 0.93 mmol), and benzoic acid (*3.3 g*, 27 mmol) were dissolved in 100 mL of DMF in a 250 mL round bottom flask and the mixture was stirred (300 rpm) at 90 °C for 5 h. After the reaction is done, PCN-224 nanoparticles were collected by centrifugation (15000 rpm,

30 min) followed by washing with fresh DMF for 3 times. The resulting PCN-224 nanoparticles were suspended in DMF for further characterization and analysis.

Variation of H_2TCPP

50 mg H_2TCPP sample. H_2TCPP (*50 mg*, 0.07 mmol), $ZrOCl_2 \cdot 8H_2O$ (300 mg, 0.93 mmol), and benzoic acid (2.9 g, 24 mmol) were dissolved in 100 mL of DMF in a 250 mL round bottom flask and the mixture was stirred (300 rpm) at 90 °C for 5 h. After the reaction is done, PCN-224 nanoparticles were collected by centrifugation (15000 rpm, 30 min) followed by washing with fresh DMF for 3 times. The resulting PCN-224 nanoparticles were suspended in DMF for further characterization and analysis.

75 mg H_2TCPP sample. H_2TCPP (*75 mg*, 0.09 mmol), $ZrOCl_2 \cdot 8H_2O$ (300 mg, 0.93 mmol), and benzoic acid (2.9 g, 24 mmol) were dissolved in 100 mL of DMF in a 250 mL round bottom flask and the mixture was stirred (300 rpm) at 90 °C for 5 h. After the reaction is done, PCN-224 nanoparticles were collected by centrifugation (15000 rpm, 30 min) followed by washing with fresh DMF for 3 times. The resulting PCN-224 nanoparticles were suspended in DMF for further characterization and analysis.

100 mg H_2TCPP sample. H_2TCPP (*100 mg*, 0.13 mmol), $ZrOCl_2 \cdot 8H_2O$ (300 mg, 0.93 mmol), and benzoic acid (2.9 g, 24 mmol) were dissolved in 100 mL of DMF in a 250 mL round bottom flask and the mixture was stirred (300 rpm) at 90 °C for 5 h. After the reaction is done, PCN-224 nanoparticles were collected by centrifugation (15000 rpm, 30 min) followed by washing with fresh DMF for 3 times. The resulting PCN-224 nanoparticles were suspended in DMF for further characterization and analysis.

125 mg H_2TCPP sample. H_2TCPP (*125 mg*, 0.16 mmol), $ZrOCl_2 \cdot 8H_2O$ (300 mg, 0.93 mmol), and benzoic acid (2.9 g, 24 mmol) were dissolved in 100 mL of DMF in a 250 mL round bottom flask and the mixture was stirred (300 rpm) at 90 °C for 5 h. After the reaction is done, PCN-224 nanoparticles were collected by centrifugation (15000 rpm, 30 min) followed by washing with fresh DMF for 3 times. The resulting PCN-224 nanoparticles were suspended in DMF for further characterization and analysis.

150 mg H_2TCPP sample. H_2TCPP (*150 mg*, 0.19 mmol), $ZrOCl_2 \cdot 8H_2O$ (300 mg, 0.93 mmol), and benzoic acid (2.9 g, 24 mmol) were dissolved in 100 mL of DMF in a 250 mL round bottom flask and the mixture was stirred (300 rpm) at 90 °C for 5 h. After the reaction is done, PCN-224 nanoparticles were collected by centrifugation (15000 rpm, 30 min) followed by washing with fresh DMF for 3 times. The resulting PCN-224 nanoparticles were suspended in DMF for further characterization and analysis.

Thermodynamic analysis

When the concentration of the system is diluted to 1/n, the concentration of PCN-224 monomer can be represented as the following.

$$\text{PCN-224}_{\text{monomer}} = [Zr_6(TCPP)_{1.5}] = \frac{K \times [Zr_6(BA)_{12} \times \frac{1}{n}] \times \left[TCPP \times \frac{1}{n}\right]^{1.5}}{\left[BA \times \frac{1}{n}\right]^{12}}$$

$$= \frac{K \times [Zr_6(BA)_{12}] \times [TCPP]^{1.5}}{[BA]^{12}} \times n^{9.5} \quad \text{(eq 1)}$$

Similar to the variable of TCPP, $[Zr_6(BA)_{12}]$ is also proportional to $Zr_6(TCPP)_{1.5}$. Therefore, a similar trend of size change in PCN-224 particles was

expected when varying the amount of Zr source. However, as $ZrOCl_2 \cdot 8H_2O$ undergoes severe hydrolysis and generates large amount of HCl, increasing the amount of Zr source led to significant protonation of porphyrin center in TCPP leading to a formation of different phase.

$$\ln K = \frac{-\Delta G^{\emptyset}}{RT} = -\frac{\Delta H^{\emptyset}}{RT} + \frac{\Delta S^{\emptyset}}{R} \quad \text{(eq 2)}$$

For the equilibrium constant (K), theoretically, temperature change can affect K value, thus influencing the concentration of PCN-224 monomer. Since the formation of MOF is an exothermic process (negative $\Delta H^{\emptyset}$), increasing the reaction temperature will result in a decreased K value, thus resulting in decreased monomer concentration (eq 2). However, because the impact of temperature on K is not linear in a range that can guarantee phase purity of MOF, the effect of temperature was not fully studied to tune the size of PCN-224 nanoparticles.

6.3 Results and discussion

Size-controlled synthesis of PCN-224 nanoparticles

In MOFs, each linker is spatially isolated by the framework, thus greatly preserving its molecular property regardless of dimensions. As a result, MOFs can be fully utilized as are small molecules, while their built-in properties are not affected by particle size.[24] We conceived that this feature would allow for maximization of passive targeting by screening optimal size of MOF nanoparticles for PDT. To investigate size-dependent targeted PDT, a Zr(IV)-based porphyrinic MOF was chosen as a model system to test our hypothesis. Zr(IV) is known for relatively good biocompatibility while its high valence

allows strong electrostatic interaction with the carboxylate linkers in the MOF for the framework robustness.[96,247] Meanwhile, the photosensitizing ability as well as the emissive nature of the porphyrinic linker endows the theranostic modality of MOF, making this platform multifunctional. The concept of PDT was demonstrated by Lin and co-workers during the course of our study. Nonetheless, we believe that the investigation of size and other factors on a suitable platform (e.g., controlled morphology) would allow us to study a correlation between MOF nanoparticles and cellular uptake for maximization of therapeutic efficacy, addressing a gap in the literature.

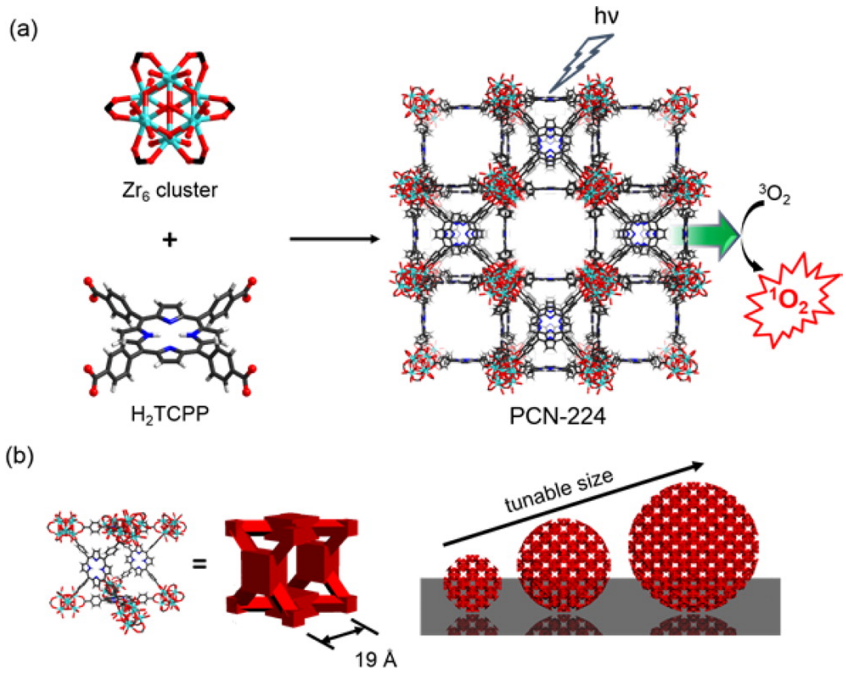

Figure 6.1 Illustration of PCN-224 structure. (a) 6-connected Zr_6 cluster ($Zr_6O_4(OH)_4(H_2O)_6(OH)_6(COO)_6$), tetratopic linker (tetrakis (4-carboxyphenyl)porphyrin (H_2TCPP)), and 3D nanoporous framework of PCN-224. (b) A cubic unit of PCN-224 and schematic illustration of spherical PCN-224 nanoparticles on the basis of building of cubic units, yielding different sizes.

Of the many reported porphyrinic Zr-MOFs, PCN-224 was considered as a strong candidate due to its extraordinary chemical stability and nanoporous channels, allowing efficient diffusion of molecular oxygen.[33,34,183] Most importantly, the cubic space group of PCN-224 would allow for isotropic growth of crystals, enabling clearer size evaluation without having to carry dependent variables along with the size variation (e.g., aspect ratio, thickness in a rod, or a plate morphology) (Figure 6.1). Therefore, we chose PCN-224 as a model system for studying the particle size effect for targeted PDT.[183]

However, downsizing of PCN-224 from a millimeter scale to nanoscale upon varying the synthetic condition was not trivial due to the easy formation of unwanted phases. To overcome such difficulty, thermodynamic analysis was attempted along with the manipulation of synthetic conditions to tune the size of PCN-224 to nanoscale. In principle, MOF formation can be simplified as ligand substitution reactions on the metal clusters.[41,240] This simple coordination chemistry enables us to derive an equilibrium of MOF formation. In the specific example of PCN-224 synthesis, the equilibrium of the PCN-224 monomer [Zr_6 $(TCPP)_{1.5}$] formation can be simplified as eq 3 where excessive benzoic acid (BA) was employed as a competing reagent that is assumed to competitively coordinate to Zr_6 cluster, forming $Zr_6(BA)_{12}$. In this work, the PCN-224 monomer was defined as a soluble species with a negligible scattering contribution, where the formula of $Zr_6(TCPP)_{1.5}$ is derived from a repeating unit of PCN-224 (H_2O and extra OH^- in the Zr_6 cluster are ignored). Therefore, the formation of the PCN-224 monomer can be summarized as eq 4.

$$Zr_6(BA)_{12} + 1.5TCPP \overset{K}{\rightleftharpoons} Zr_6(TCPP)_{1.5} + 12BA \qquad \text{(eq 3)}$$

$$[\text{PCN-224}_{\text{monomer}}] = [Zr_6(TCPP)_{1.5}] = \frac{K \times [Zr_6(BA)_{12}] \times [TCPP]^{1.5}}{[BA]^{12}} \quad \text{(eq 4)}$$

Ideally, manipulation of any factor in eq 4 would cause a change in the concentration of the PCN-224 monomer, which would eventually affect the particle size through the nucleation step.[213,248-250] However, our attempts to directly tune these factors (e.g., benzoic acid) from its synthetic condition of millimeter-sized single crystals failed to reduce the size to nanoscale, while giving phase impurity, presumably due to the dramatic change in the ratios between each reactant.

Table 6.1 Effect of the reaction volume on the particle size.

DMF (mL)	*D* (nm)[a]	PDI
80	225.7 ± 30.2	0.005
100	95.9 ± 24.0	0.103
120	71.6 ± 18.2	0.080
140	42.1 ± 11.0	0.191

Table 6.2 Effect of benzoic acid (competing reagent) on the particle size.

Benzoic Acid (g)	*D* (nm)[a]	PDI
2.2	23.8 ± 6.8	0.239
2.6	60.2 ± 15.7	0.086
2.8	94.1 ± 24.2	0.132
3.0	182.8 ± 46.6	0.072
3.3	232.5 ± 51.8	0.055

Table 6.3 Effect of H_2TCPP on the particle size.

H_2TCPP (mg)	*D* (nm)[a]	PDI
50	280.4 ± 36.3	0.032
75	110.4 ± 30.0	0.197
100	84.1 ± 23.2	0.215
125	64.8 ± 18.0	0.196
150	57.9 ± 15.5	0.177

Thus, we embarked on downsizing PCN-224 by diluting the system to preserve the phase purity from unchanged stoichiometry between reactants, while aiming to create more MOF monomers, which would result in smaller particles (Tables 6.1-6.3). Upon five times of dilution from its single crystal synthetic condition, PCN-224 nanoparticles with a size of ~90 nm, based on dynamic light scattering (DLS) in DMF, were achieved and this condition was established and denoted as a reference condition for the following investigation. Then, we sought to realize a precise size control of the particles in the nano regime by utilizing different impact of size-tuning ability of each factor as analyzed. According to eq 4, for instance, the concentration of PCN-224 monomer is strongly dependent on the concentration of BA due to the high order of $[BA]^{12}$ in the equation, suggesting a significant impact of [BA] on the size of PCN-224 nanoparticles. Starting from the reference condition, when the amount of BA was varied with a ~200 mg interval from 2.2 to 3.3 g, the size of PCN-224 nanoparticles increased from 24 to 232 nm (Table 6.2). The tuning of the particle size in a narrower range was observed from variation of [TCPP] due to a lower order ($[TCPP]^{1.5}$) in the equation, making it a suitable variable for fine-tuning (Table 6.3). These results are also consistent with our thermodynamic analysis. For instance, according to eq 4, the increased amount of BA would result in decreased number of the PCN-224 monomer in the system, thus yielding larger nanoparticles. Similarly, varying the concentration of TCPP can also change the concentration of the monomer in an opposite trend to BA, which can also be predicted by eq 4. Therefore, adjustment of each factor in eq 4 allows fine-tuning of the size of PCN-224 nanoparticles. These results also suggest that understanding the size tunability of each factor holds great

potential in providing design insights for nanomaterials that require such control in diverse future applications.

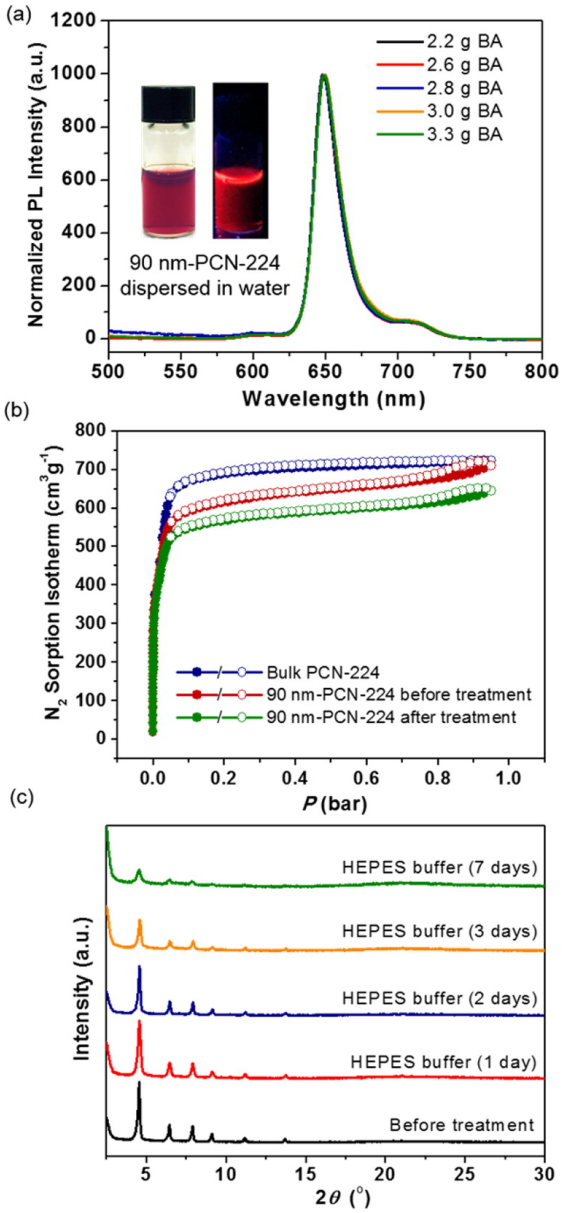

Figure 6.2 Characterization of PCN-224 nanoparticles. (a) Size-dependence of emission spectra (λ_{ex} = 420 nm). Inset: 90 nm-PCN-224 dispersed in water under (left) ambient light and (right) UV irradiation (λ = 365 nm), respectively. (b) N_2 adsorption isotherms of PCN-224 (bulk sample, 90 nm-PCN-224 before and after the water treatment (37 °C, 24 h). (c) Powder X-ray diffractions of PCN-224 nanoparticles after stability test (0.1 M HEPES, pH 7.4, 37 °C).

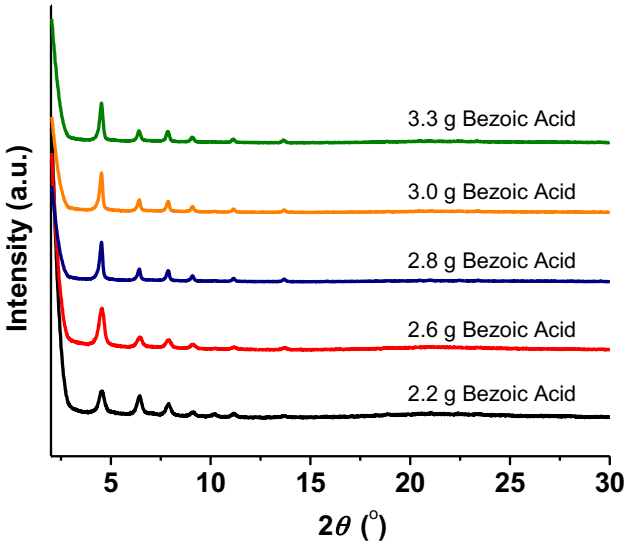

Figure 6.3 PXRD of PCN-224 samples with BA variation.

Among the variables, the set varied with the concentration of benzoic acid was chosen for detailed studies, due to an ease of variable control and a broad range of sizes. Powder X-ray diffraction (PXRD) data clearly show the pure phase of PCN-224 (Figure 6.3). To further confirm our hypothesis that the identity of MOF nanoparticles will not be altered by size variation, photophysical properties of the BA-varied set were tested by UV–vis and fluorescence spectroscopy. In absorption spectra, a slight red shift was observed as the particle size increased along with more scattering, as expected from typical observation in nanomaterials (Figure 6.4). Interestingly, their emission profiles, which are closely related to the photosensitization to generate $^1O_2$, show the same emission maxima (λ_{em} = 650 nm) for any size of samples, indicating the molecular level of design is well maintained regardless of their size (Figure 6.2a).

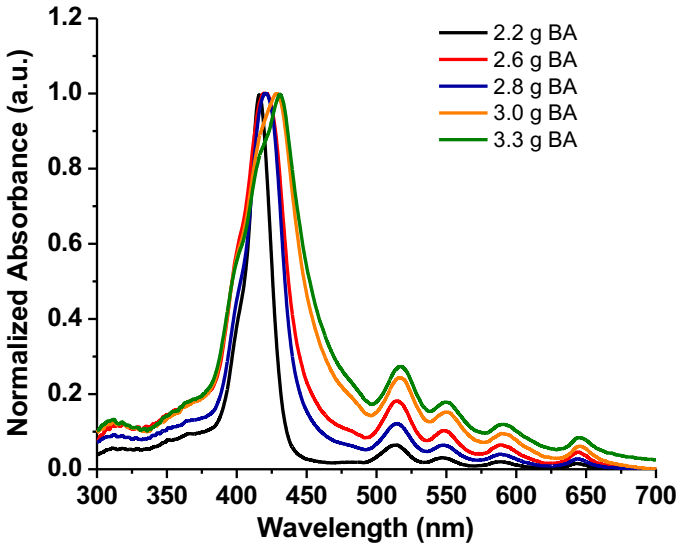

Figure 6.4 Absorption spectra of PCN-224 samples with different sizes varied by BA.

Having confirmed this unaltered molecular property of different sizes of PCN-224 nanoparticles, the stability of the framework in aqueous media was then examined. In Figure 6.2b, N_2 sorption of nanoparticles showed well maintained porosity compared to that of bulk crystalline PCN-224. Notably, after 24 h of water treatment at 37 °C, the porosity of PCN-224 nanoparticles was still preserved only with a slight decrease in N_2 uptake probably due to the inevitable destruction of the framework under aqueous condition (Figure 6.2b). PXRD data also confirmed that PCN-224 nanoparticles can retain their crystallinity in buffer (0.1 M HEPES, pH 7.4, 37 °C) for 2 days while gradually decreasing in crystallinity over 7 days (Figure 6.2c). In particular, PXRD data revealed that PCN-224 nanoparticles treated with cell culture medium, DMEM for 24 h maintained the crystallinity. These results indicate that PCN-224 nanoparticles would remain intact as the MOF until PDT treatment, considering typical cellular internalization and

irradiation time for the treatment. To our surprise, PCN-224 nanoparticles can also be well dispersed in both DMF and H_2O in the absence of additional surfactant (Figure 6.2a inset). With most other conventional nanoparticles, surfactants are often required to prevent strong interparticle interaction for better dispersibility. Perhaps due to the 3D cubic grid-like porous structure of PCN-224 as well as its spherical morphology, it may provide tangential contact between particles, allowing minimal interaction on their surface. The ζ potential of PCN-224 nanoparticles of ~20 mV also supports their moderate dispersibility (Table 6.4).

Table 6.4 Summary of physicochemical properties of PCN-224 nanoparticles.

PCN-224 label	BA (g)	TEM (nm)	D_h (nm)	PDI	ζ potential (mV)
30 nm	2.2	33 ± 4	65 ± 3	0.246	19.6±6.41
60 nm	2.6	59 ± 5	114 ± 3	0.067	25.3±6.27
90 nm	2.8	91 ± 8	137 ± 2	0.053	19.8±7.15
140 nm	3.0	144 ± 7	197 ± 1	0.035	22.7±5.92
190 nm	3.3	189 ± 11	255 ± 2	0.025	20.7±5.59

Table 6.5 Physiochemical properties of PCN-224 samples with different sizes varied by BA.

Sample label	TEM diameter (nm)	D_h (nm)	PDI	ζ potential (mV)
30 nm	33 ± 4	65 ± 3	0.246	19.6±6.41
60 nm	59 ± 5	114 ± 3	0.067	25.3±6.27
90 nm	91 ± 8	137 ± 2	0.053	19.8±7.15
140 nm	144 ±7	197 ± 1	0.035	22.7±5.92
190 nm	189 ± 11	255 ± 2	0.025	20.7±5.59

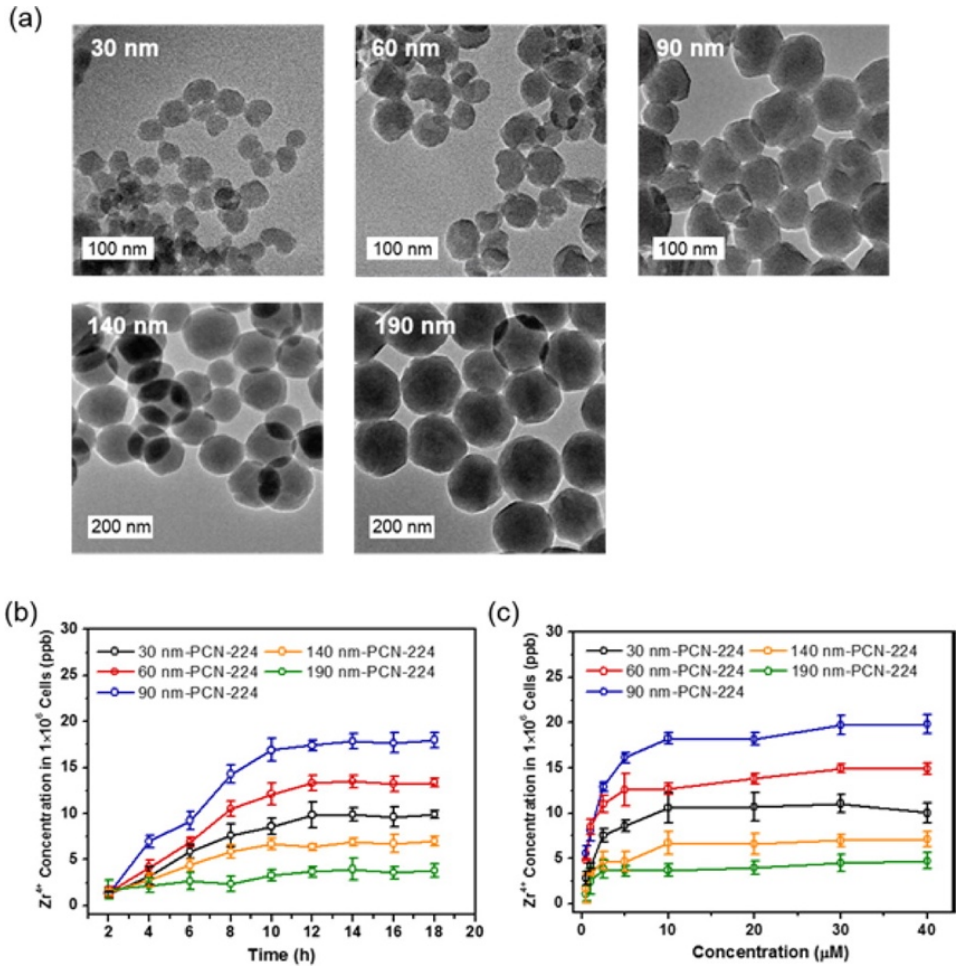

Figure 6.5 TEM images and cellular studies of PCN-224 nanoparticles. (a) TEM images of PCN-224 nanoparticles of 30, 60, 90, 140, and 190 nm. (b) Cellular uptake of PCN-224 samples with different sizes at various incubation time. Concentration = 20 μM. (c) Cellular uptake of different sized PCN-224 nanoparticles at various concentrations. Incubation time = 24 h. Data are based on ICP analysis of the Zr concentration internalized into HeLa cells. Data are means ± s.d. (N = 3).

Passive targeting: particle size-dependent cellular uptake and PDT

Although the effect of physical dimension of some other nanoparticles (i.e., gold nanoparticles, carbon nanotubes) for cellular uptake has been studied, it has been known that their correlations are also significantly affected by the composition of the nanomaterials.[14] Considering only a rare example can be referred as a study of the size-

related cellular response with MOF nanomaterials,[206] PCN-224 model platform, covering a broad range in interest of biological studies, can provide important design insight for future study in MOF size-cell interaction. To determine the size-dependent cellular response, five size fractions, ranging from 30 to 190 nm, based on transmission electron microscopy (TEM) results, were applied to HeLa (human cervical cancer) cells (Table 6.4 and Figure 6.5a). Quantitative analysis of uptake of the nanoparticles was achieved using inductively coupled plasma mass spectrometry (ICP-MS) upon cell digestion. To begin, time-dependent cellular uptake of PCN-224 nanoparticles was studied to obtain insight for kinetics of endocytosis. The cellular uptake showed a plateau around 12 h for each fraction (Figure 6.5b). Dose-dependent uptake of PCN-224, ranging from 0.5 to 40 μM (TCPP equiv), was also carried out. Interestingly, ICP results indicate that different amount of Zr entered into the cells, suggesting the different sizes of particles indeed resulted in different cellular responses (Figure 6.5c). Notably, 90 nm-PCN-224 showed the highest amount of Zr uptake in cells which also suggests the greatest uptake of TCPP by MOF structure, among other sizes (Figure 6.6a).

Table 6.6 Calculated numbers of PCN-224 nanoparticle uptake in each cell.

Samples	$Zr/_{particle}$ (mol)	$Zr/_{cell}$ (mol)	$TCPP/_{cell}$ (mol)	$N_{particle/cell}$
30 nm-PCN-224	$4.95\cdot10^{-21}$	$2.32\cdot10^{-14}$	$5.80\cdot10^{-15}$	$4.68\cdot10^{6}$
60 nm-PCN-224	$3.96\cdot10^{-20}$	$2.78\cdot10^{-14}$	$6.95\cdot10^{-15}$	$7.01\cdot10^{5}$
90 nm-PCN-224	$1.34\cdot10^{-19}$	$4.00\cdot10^{-14}$	$1.00\cdot10^{-14}$	$2.99\cdot10^{5}$
140 nm-PCN-224	$5.03\cdot10^{-19}$	$1.46\cdot10^{-14}$	$3.65\cdot10^{-15}$	$2.90\cdot10^{4}$
190 nm-PCN-224	$1.26\cdot10^{-18}$	$8.20\cdot10^{-15}$	$2.05\cdot10^{-15}$	$6.51\cdot10^{3}$

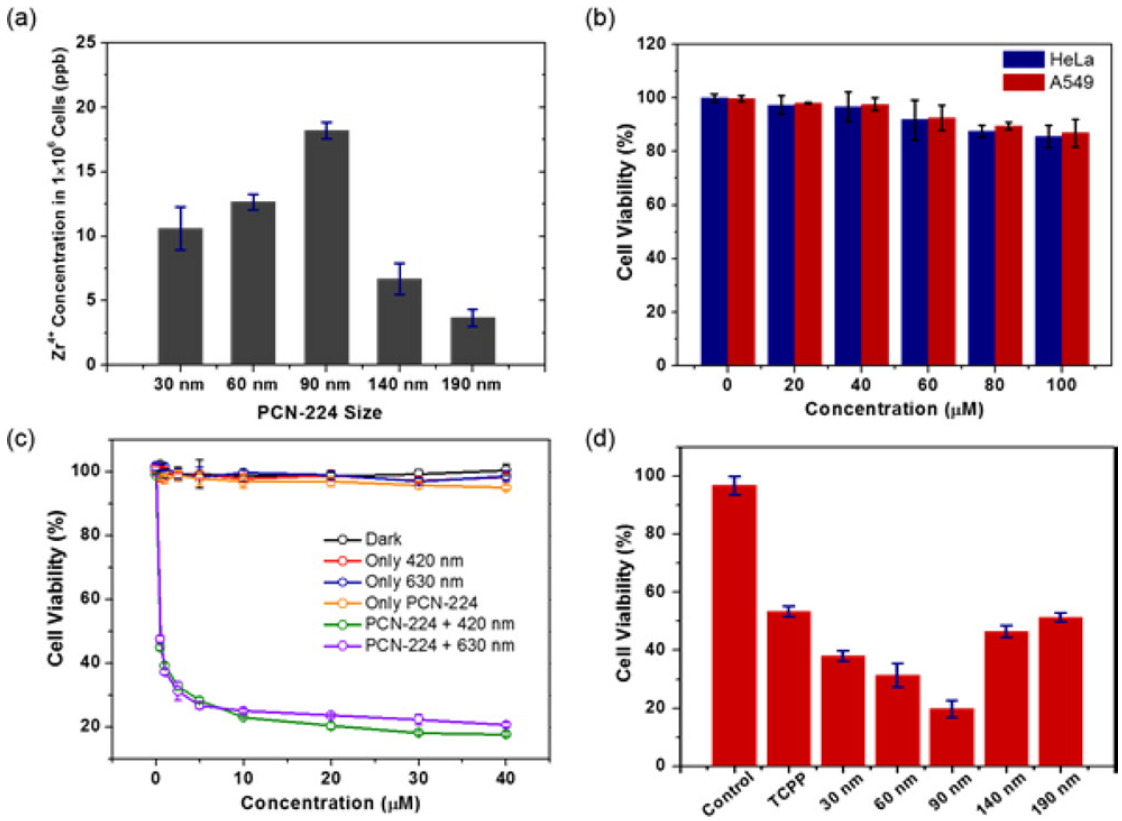

Figure 6.6 Cellular response and PDT efficacy of PCN-224 nanoparticles. (a) Size-dependent cellular uptake of PCN-224 nanoparticles. Incubation time = 24 h. (b) Cytotoxicity of 90 nm-PCN-224 in HeLa and A549 cells at various concentrations for 48 h. (c) Control experiments of cytotoxicity in HeLa cells upon light irradiation of 420 and 630 nm in the absence and presence of 90 nm-PCN-224. Irradiation time = 30 min. (d) Comparison of PDT efficacy between different sized PCN-224 nanoparticles and free TCPP molecules. Data are means ± s.d. (N = 3).

Having examined size-dependent cellular uptake of PCN-224 nanoparticles, PDT efficacy of the five size fractions, each at 20 μM, were tested for HeLa cells under irradiation at Soret band (420 nm). Among these five fractions, 90 nm-PCN-224 showed the best PDT efficacy of 81%, while 190 nm-PCN-224 gave the lowest efficacy of 49% in agreement with the results of cellular uptake (Figure 6.6d). Markedly, free photosensitizer (TCPP linker only) showed only 47% in PDT efficacy at the same

concentration, which further confirms our hypothesis that MOF nanoparticle formulation and the size screening can optimize the performance of the given photosensitizer. Interestingly, the PDT efficacy does not show much correlation with the number of nanoparticles inside the cells where we converted Zr content to the number of particles (Table 6.6). Rather, 90 nm-PCN-224 with a moderate number of particles internalized shows the greatest PDT efficacy as a result of the highest Zr/TCPP uptake (Figure 6.6d) while showing no evident toxicity of the material itself even at high concentration after 48 h incubation (viability of ~90% at 100 μM) (Figure 6.6b). These results clearly show a strong correlation between PDT efficacy and the TCPP concentration in the cells, rather than the number of particles. Such correlation, therefore, indicates that TCPP linkers in PCN-224 nanoparticles are fully utilized regardless of the particle size, as are small molecules, resulting from the 3D nanoporous structure of PCN-224 while preference for internalization was determined by the size of MOF nanoparticle. It is important to note that these results address the need for insights in the design/selection of MOFs, because the density of desired function in the framework is proportional to the size, while the size parameter is another determinant for optimizing the dynamics between materials and cells.

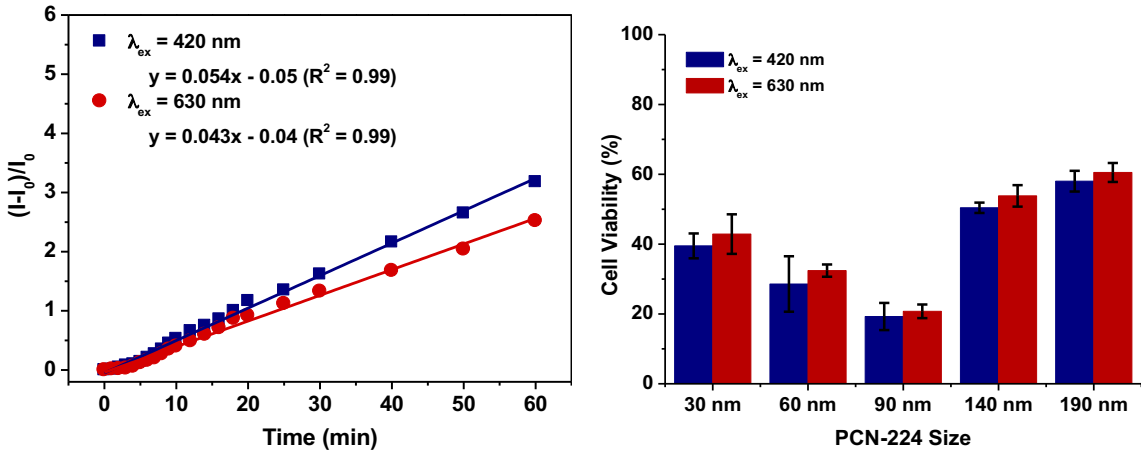

Figure 6.7 (left) Singlet oxygen generation of 90 nm-PCN-224 under 420 nm and 630 nm light irradiation. (right) Size-dependent *in vitro* PDT efficacy of PCN-224 nanoparticles in HeLa cells upon 420 nm (blue bars) and 630 nm (red bars) irradiation, respectively. Concentration = 20 μM. Incubation time = 24 h. Irradiation time = 30 min. (mean ± s.d., $N = 3$)

Because TCPP can absorb the light at Q bands other than its Soret band, we further investigated the PDT efficacy of the size optimized PCN-224 nanoparticles (90 nm) under irradiation at 630 nm, which would provide better tissue penetration in practice. Although the irradiation at 420 nm showed slightly better $^1O_2$ generation than at 630 nm due to the strong absorption of the Soret band in singlet oxygen generation study, PDT efficacy of 90 nm PCN-224 under 630 nm irradiation could reach as high as ~80%, which is almost the same as the efficacy under 420 nm irradiation (Figure 6.6c). Presumably due to the highly dense assembly of TCPP in PCN-224, while the framework prevents the aggregation of photosensitizers, O_2 molecules in cells might have sufficient contact with surrounding photosensitizers. Consequently, the weaker absorption of TCPP at 630 nm irradiation may be compensated by sufficient interaction between O_2 and photosensitizers inside of PCN-224 nanoparticles, resulting in similar efficacy (Figure 6.7). In addition, the

subcellular localization of PCN-224 in HeLa cells was confirmed with fluorescent staining. Notably, the red fluorescence of PCN-224 matches well with the green fluorescence from Lyso Tracker and Mito Tracker, while showing negligible overlap between PCN-224 and nucleus, indicating the PCN-224 nanoparticles are mostly localized in the cytoplasm (Figure 6.8).

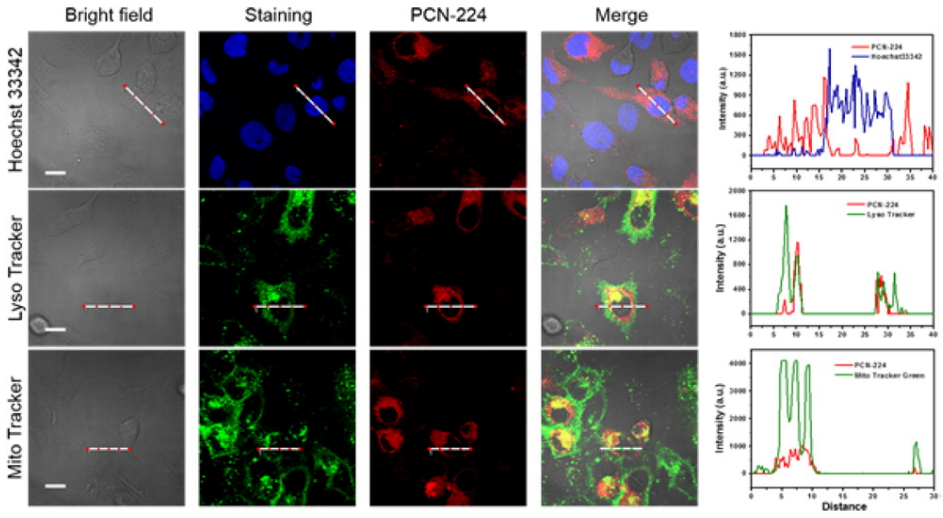

Figure 6.8 Subcellular localization of PCN-224 nanoparticles by staining with organelle markers, Hoechst 33342, Lyso Tracker, and Mito Tracker green.

Active targeting: folic acid modification on PCN-224 nanoparticles

Folate is a commonly used ligand for targeting folate receptor (FAR) abundant tumor cells, including ovarian tumors, to enhance the delivery of nanoparticles/drugs.[251,252] Therefore, we further sought to build an active targeting modality in our platform through postsynthetic folic acid (FA) modification on the surface of 90 nm-PCN-224. Because there are available binding sites on the Zr_6 cluster in PCN-224, the carboxylate end of folate could be attached to Zr_6 clusters by coordination (Figure

6.9a).[253] However, as previous results suggest that the size of nanoparticles will also affect the uptake, the degree of FA functionalization was designed to bear a minimal size expansion to prepare comparable sizes. A series of FA modified 90 nm-PCN-224 was prepared by reaction with different stoichiometries of 1/8, 1/4, and 1/2 equiv of FA to the available Zr binding sites. The size of samples was confirmed by TEM and DLS, which showed the modification extent, not involving drastic changes in size and surface charge (Table 6.7). Also, the characteristic absorption band of FA confirmed the different degree of FA functionalization as well as quantification of actual FA loading of each sample (Table 6.8). $^1O_2$ generating ability of PCN-224 nanoparticles after the FA modification remains almost the same as pristine PCN-224 nanoparticles, providing a good control to evaluate the influence of FA modification. In order to test the active targeting upon FA modification, the PDT efficacy of samples was tested with HeLa cells, known for FAR abundant cell line.[254] As a result, 1/4FA-PCN-224 showed the most potency: more than 90% of PDT efficacy, which is an enhancement from unmodified PCN-224 under the same condition (Figure 6.9b). Although any degree of FA modification provided an enhancement from the unmodified sample, the lesser enhancement from 1/8FA-PCN-224 may result from insufficient FA density than that of 1/4FA-PCN-224, whereas 1/2FA-PCN-224 showed the least enhancement perhaps due to the size expansion (Figure 6.9b). Overall, this improvement in PDT efficacy shows the great potential of this system of which the maximization of the desired function can be achieved through optimizations of both physical and chemical properties of the MOF nanoplatform.

Table 6.7 Physiochemical properties of FA modified PCN-224 nanoparticles with varying loading ratios.

FA/PCN-224	TEM (nm)	D_h (nm)	PDI	ζ potential (mV)
0	91 ± 8	137 ± 2	0.053	20.3±4.69
1/8FA	98 ± 8	143 ± 2	0.091	17.0±4.23
1/4FA	102 ± 10	156 ± 1	0.213	19.2±4.99
1/2FA	110 ± 11	175 ± 4	0.178	16.6±3.90

Table 6.8 Quantification of actual folate loadings on 90 nm-PCN-224 sample (10 μM). Based on the chemical formula of PCN-224, each TCPP linker corresponds to four Zr atoms. As the concentration of our material (C_{pcn}) is based on TCPP, the concentration of Zr will be $4xC_{pcn}$. Since each Zr_6 contains 6 available positions for the further coordination of carboxylate, ideally each Zr atom corresponds to one folic acid if full occupation of the available coordination sites on Zr_6 cluster were assumed.

FA/Zr stoichiometry	FA Concentration (μM)			Actual FA/Zr ratio (C_l /$4C_{pcn}$)
	Initial (C_i)	Supernatant (C_s)	Loaded ($C_l = C_i - C_s$)	
0	0	0	0	0
1/8	5	3.80	1.20	~3/100
1/4	10	7.61	2.39	~3/50
1/2	20	16.02	3.98	~1/10

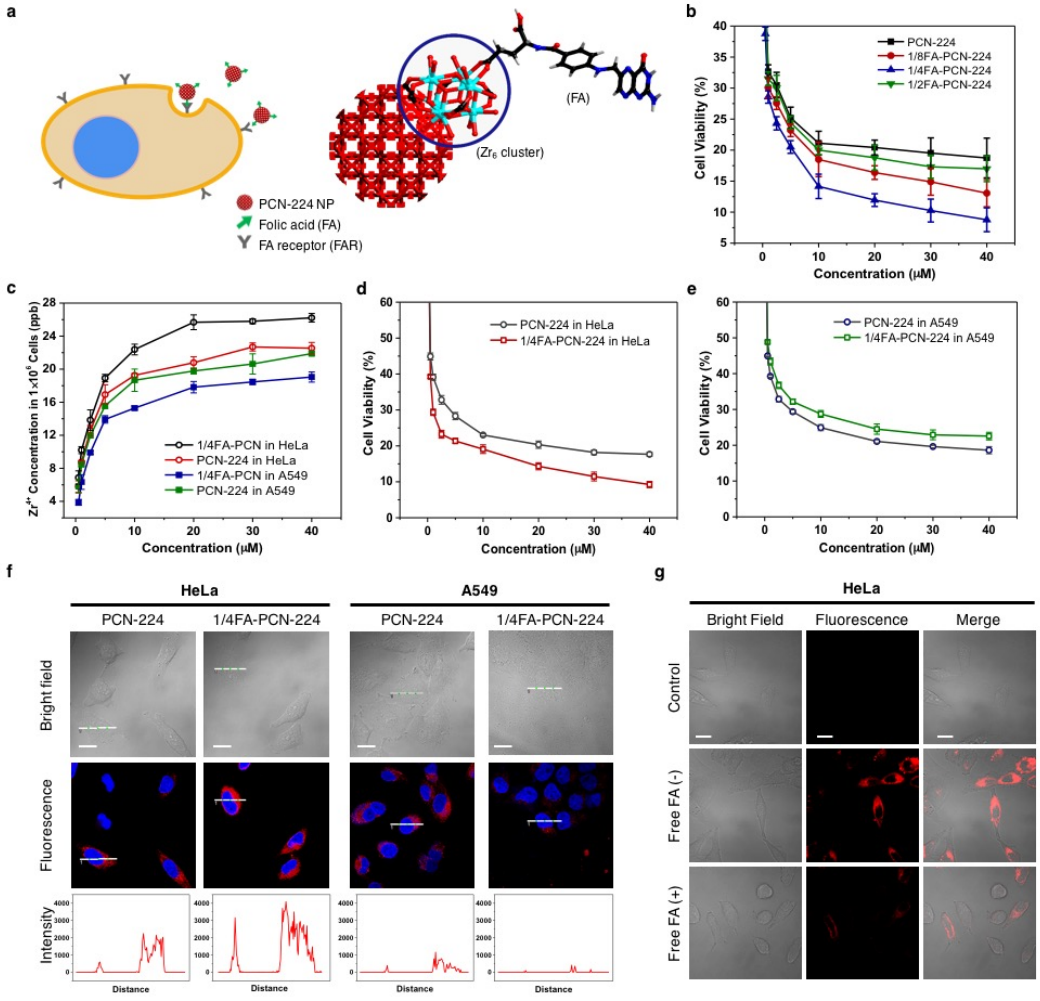

Figure 6.9 In vitro PDT study of FA functionalized 90 nm-PCN-224. (a) Scheme of FA functionalized PCN-224 nanoparticle and proposed internalization. (b) In vitro PDT efficacy of FA functionalized (FA equivalent of 0, 1/8, 1/4, 1/2) 90 nm-PCN-224 at various concentrations in HeLa cells. Irradiation at 420 nm for 30 min for PDT. (c) ICP analysis of cellular uptake of unfunctionalized and FA functionalized 90 nm-PCN-224 at various concentrations in HeLa and A549 cells. Incubation time =24 h. (d,e) Comparison of in vitro PDT efficacy of pristine PCN-224 and 1/4FA-PCN-224 in (d) HeLa cells and (e) A549 cells. (f) CLSM images of HeLa and A549 cells incubated with pristine PCN-224 and 1/4FA-PCN-224 samples. Red channel images were obtained from pristine or FA functionalized PCN-224. The blue channel images were obtained from Hoechst 33342 (nucleus). Concentration =20 μM. Incubation time =60 min. Scale bars =20 μm. (g) CLSM images of HeLa cells without any treatment (top row); treated with 1/4FA-PCN-224 (middle row); coincubated with excess amount of free FA (1 mM) and 1/4FA-PCN-224 (bottom row). Concentration =20 μM. Incubation time =60 min. Scale bars =20 μm. Data are means ± s.d. ($N = 3$).

To further confirm the effect of active targeting, both FA modified and unmodified 90 nm-PCN-224 were applied to FAR-negative cell line, A549 as a control experiment. Interestingly, FA functionalized PCN-224 showed no apparent advantages over unmodified nanoparticles both in uptake and ensuing PDT efficacy, rather it showed even less merit (Figure 6.9c,e). Likely due to different size preferences for permeability of the particles in A549 cells, a slight increase in size of PCN-224 upon FA modification showed rather negative impacts on the uptake in FAR negative A549 cells (Figure 6.9c–f). In parallel, a competition assay was implemented with 1/4FA-PCN-224 in the presence of an excess amount of free FA as a competing ligand for folate receptor.[255] Indeed, HeLa cells treated with the excess free FA (1 mM) showed much weaker fluorescence in confocal microscopy images, indicating functionalized FA on the MOF was involved in the uptake event through receptor-mediated endocytosis (Figure 6.9g).

6.4 Conclusions

Through thermodynamic analysis, the size of PCN-224 nanoparticles was successfully tuned to a range that is of interest to biological studies (30–190 nm). Our hypothesis is successfully proved by preferential cellular uptake of 90 nm-PCN-224 and its remarkable PDT efficacy over other sizes, including free TCPP linkers. These results clearly demonstrate the fabrication of photosensitizer as MOF nanoparticles followed by the optimization of their size parameter indeed play a critical role for improving cellular response. Together with our findings in size-controllable synthesis of MOF nanoparticles, the PCN-224 nanoplatform demonstrates active targeting modality for further enhancement of PDT efficacy, of which the enhancement was obtained by postsynthetic

FA modification onto Zr_6 cluster. Meanwhile, the potential of theranostic modality was demonstrated from the porphyrinic linker in the MOF in cancer cell model. Having confirmed the preserved molecular properties of the incorporated linker, invariable to MOF sizes, we envision that combination of the synthetic tunability of MOF on the molecular scale and its size controllability can create useful tools for specific needs in desired applications through chemical, physical, and structural design of MOF nanoplatform.

7. SUMMARY

To tackle some challenges that MOF materials face for broad application, this dissertation focused on synthetic methodologies to functionalization of stable MOFs. In sections 2 and 3, the strategies of designed functional linker exchange and/or dual exchange including metal metathesis successfully demonstrated the introduction of functionality and enhanced chemical stability in a mesoporous MOF platform. Possible rationales in regards to the observations have also been discussed from a thermodynamics and kinetics standpoint, providing a useful insight for these findings to be generalized for other MOF systems.

In section 4, a new 3D MOF consisting of 2D porphyrinic layers pillared by photochromic molecular switches was synthesized. This mixed linker MOF was demonstrated for the control of $^1O_2$ generation via energy transfer by taking advantage of the well-defined structure of the MOF in a periodic array. The features of MOFs guaranteed high accessibility for substrates, while preventing quenching of dyes, which is detrimental for energy transfer.

However, the classical Zn-based pillar-layer strategy often yields MOFs with weak chemical stability and limits adjusting molar ratios of component linkers due to the topological incompatibility. To address this issue, the *in situ* incorporation of multiple functionalities in a highly stable Zr-MOF was proposed for the fine-tuning of the energy transfer efficiency to control $^1O_2$ generation. This strategy shows great potential for the protected delivery of the integrated photosensitizing system as optimized, allowing enhanced *in vitro* PDT efficacy with superior $^1O_2$ controllability upon MOF formulation

compared to that of the homogeneous mixture of the dyad. In terms of PDT, however, excitation at longer wavelength of light is highly desired. Therefore, future works will be directed toward preparing upconversion MOF nanoplatform, where the photosensitizer in the MOF can be excited by near infrared irradiation allowing better practicality in cancer treatments.

In summary, the findings and discussion in this dissertation could provide useful tools for the rational design of MOFs for use in specific applications while also placing these materials at the forefront of interdisciplinary study.

REFERENCES

(1) Zhou, H.-C.; Long, J. R.; Yaghi, O. M. *Chem. Rev.* **2012**, *112*, 673.

(2) Chui, S. S. Y. *et al. Science* **1999**, *283*, 1148.

(3) Li, Z. *et al. Chem. Soc. Rev.* **2012**, *41*, 2590.

(4) Valtchev, V.; Tosheva, L. *Chem. Rev.* **2013**, *113*, 6734.

(5) Mahato, P. *et al. Nat. Mater.* **2015**, *14*, 924.

(6) Son, H.-J. *et al. J. Am. Chem. Soc.* **2012**, *135*, 862.

(7) Anderson, J. S.; Gallagher, A. T.; Mason, J. A.; Harris, T. D. *J. Am. Chem. Soc.* **2014**, *136*, 16489.

(8) Kurmoo, M. *Chem. Soc. Rev.* **2009**, *38*, 1353.

(9) Pearson, R. G. *J. Am. Chem. Soc.* **1963**, *85*, 3533.

(10) Férey, G. *et al. Science* **2005**, *309*, 2040.

(11) Zhang, J.-P.; Zhang, Y.-B.; Lin, J.-B.; Chen, X.-M. *Chem. Rev.* **2012**, *112*, 1001.

(12) Taube, H. *Chem. Rev.* **1952**, *50*, 69.

(13) He, C.; Liu, D.; Lin, W. *Chem. Rev.* **2015**, *115*, 11079.

(14) Vallet-Regi, M.; Balas, F.; Arcos, D. *Angew. Chem. Int. Ed.* **2007**, *46*, 7548.

(15) Hoffmann, F.; Cornelius, M.; Morell, J.; Froeba, M. *Angew. Chem. Int. Ed.* **2006**, *45*, 3216.

(16) Vivero-Escoto, J. L.; Slowing, I. I.; Trewyn, B. G.; Lin, V. S. Y. *Small* **2010**, *6*, 1952.

(17) Soler-Illia, G. J. d. A. A.; Sanchez, C.; Lebeau, B.; Patarin, J. *Chem. Rev.* **2002**, *102*, 4093.

(18) Hudson, S.; Cooney, J.; Magner, E. *Angew. Chem. Int. Ed.* **2008**, *47*, 8582.

(19) Hanefeld, U.; Gardossi, L.; Magner, E. *Chem. Soc. Rev.* **2009**, *38*, 453.

(20) Stein, A.; Wang, Z.; Fierke, M. A. *Adv. Mater.* **2009**, *21*, 265.

(21) Slowing, I. I.; Trewyn, B. G.; Giri, S.; Lin, V. S. Y. *Adv. Funct. Mater.* **2007**, *17*, 1225.

(22) Huh, S. *et al. Chem. Mater.* **2003**, *15*, 4247.

(23) Sumida, K. *et al. Chem. Rev.* **2012**, *112*, 724.

(24) Yoon, M.; Srirambalaji, R.; Kim, K. *Chem. Rev.* **2012**, *112*, 1196.

(25) Zhang, T.; Lin, W. *Chem. Soc. Rev.* **2014**, *43*, 5982.

(26) Song, L. *et al. Energy Environ. Sci.* **2012**, *5*, 7508.

(27) Deng, H. *et al. Science* **2012**, *336*, 1018.

(28) Hwang, Y. K. *et al. Angew. Chem. Int. Ed.* **2008**, *47*, 4144.

(29) Park, Y. K. *et al. Angew. Chem. Int. Ed.* **2007**, *46*, 8230.

(30) Koh, K.; Wong-Foy, A. G.; Matzger, A. J. *Angew. Chem. Int. Ed.* **2008**, *47*, 677.

(31) Furukawa, H. *et al. Science* **2010**, *329*, 424.

(32) Mondloch, J. E. *et al. J. Am. Chem. Soc.* **2013**, *135*, 10294.

(33) Feng, D. *et al. Angew. Chem. Int. Ed.* **2012**, *51*, 10307.

(34) Morris, W. *et al. Inorg. Chem.* **2012**, *51*, 6443.

(35) Horcajada, P. *et al. Chem. Commun.* **2014**, *50*, 6872.

(36) Chen, Y. *et al. J. Am. Chem. Soc.* **2012**, *134*, 13188.

(37) Senkovska, I.; Kaskel, S. *Chem. Commun.* **2014**, *50*, 7089.

(38) Wang, X.-S. *et al. J. Am. Chem. Soc.* **2006**, *128*, 16474.

(39) Wang, X.-J. *et al. Chem. Commun.* **2012**, *48*, 10286.

(40) Feng, D. *et al. Nat. Commun.* **2015**, *6*, 5979.

(41) Feng, D. *et al. Nat. Commun.* **2014**, *5*, 5723.

(42) Wang, Z.; Cohen, S. M. *Chem. Soc. Rev.* **2009**, *38*, 1315.

(43) Burnett, B. J.; Barron, P. M.; Hu, C.; Choe, W. *J. Am. Chem. Soc.* **2011**, *133*, 9984.

(44) Tanabe, K. K.; Cohen, S. M. *Chem. Soc. Rev.* **2011**, *40*, 498.

(45) Karagiaridi, O. *et al. Chem. Sci.* **2012**, *3*, 3256.

(46) Karagiaridi, O. *et al. J. Am. Chem. Soc.* **2012**, *134*, 18790.

(47) Kim, M. *et al. Chem. Sci.* **2012**, *3*, 126.

(48) Bury, W. *et al. Chem. Mater.* **2013**, *25*, 739.

(49) Fei, H.; Cahill, J. F.; Prather, K. A.; Cohen, S. M. *Inorg. Chem.* **2013**, *52*, 4011.

(50) Gross, A. F.; Sherman, E.; Mahoney, S. L.; Vajo, J. J. *J. Phys. Chem. A* **2013**, *117*, 3771.

(51) Hirai, K. *et al. Dalton Trans.* **2013**, *42*, 15868.

(52) Jeong, S. *et al. Chem. Mater.* **2013**, *25*, 1047.

(53) Karagiaridi, O. *et al. Chem. Mater.* **2013**, *25*, 3499.

(54) Kim, S. *et al. J. Am. Chem. Soc.* **2013**, *135*, 963.

(55) Li, T. *et al. J. Am. Chem. Soc.* **2013**, *135*, 11688.

(56) Valtchev, V.; Majano, G.; Mintova, S.; Perez-Ramirez, J. *Chem. Soc. Rev.* **2013**, *42*, 263.

(57) Deria, P. *et al. Chem. Soc. Rev.* **2014**, *43*, 5896.

(58) Takaishi, S. *et al. Chem. Sci.* **2013**, *4*, 1509.

(59) Han, Y.; Li, J.-R.; Xie, Y.; Guo, G. *Chem. Soc. Rev.* **2014**, *43*, 5952.

(60) Jeong, S. *et al. Chem. Mater.* **2014**, *26*, 1711.

(61) Karagiaridi, O. *et al. Angew. Chem. Int. Ed.* **2014**, *53*, 4530.

(62) Morabito, J. V. *et al. J. Am. Chem. Soc.* **2014**, *136*, 12540.

(63) Szilagyi, P. A. *et al. J. Phys. Chem. C* **2014**, *118*, 19572.

(64) Kim, M. *et al. J. Am. Chem. Soc.* **2012**, *134*, 18082.

(65) Liu, T.-F. *et al. J. Am. Chem. Soc.* **2014**, *136*, 7813.

(66) Brozek, C. K.; Dinca, M. *Chem. Soc. Rev.* **2014**, *43*, 5456.

(67) Savonnet, M. *et al. J. Am. Chem. Soc.* **2010**, *132*, 4518.

(68) Yu, C.-J.; Wu, S.-M.; Tseng, W.-L. *Anal. Chem.* **2013**, *85*, 8559.

(69) Taylor-Pashow, K. M. L. *et al. J. Am. Chem. Soc.* **2009**, *131*, 14261.

(70) Horcajada, P. *et al. Chem. Rev.* **2012**, *112*, 1232.

(71) Kreno, L. E. *et al. Chem. Rev.* **2012**, *112*, 1105.

(72) Li, J.-R.; Sculley, J.; Zhou, H.-C. *Chem. Rev.* **2012**, *112*, 869.

(73) Suh, M. P.; Park, H. J.; Prasad, T. K.; Lim, D.-W. *Chem. Rev.* **2012**, *112*, 782.

(74) Wang, C.; Zhang, T.; Lin, W. *Chem. Rev.* **2012**, *112*, 1084.

(75) Liu, J. *et al. Chem. Soc. Rev.* **2014**, *43*, 6011.

(76) Qiu, S.; Xue, M.; Zhu, G. *Chem. Soc. Rev.* **2014**, *43*, 6116.

(77) Li, H. *et al. ACS Catal.* **2011**, *1*, 1604.

(78) Lykourinou, V. *et al. J. Am. Chem. Soc.* **2011**, *133*, 10382.

(79) Canivet, J.; Aguado, S.; Schuurman, Y.; Farrusseng, D. *J. Am. Chem. Soc.* **2013**, *135*, 4195.

(80) Bauer, S. *et al. Inorg. Chem.* **2008**, *47*, 7568.

(81) Tanabe, K. K.; Cohen, S. M. *Angew. Chem. Int. Ed.* **2009**, *48*, 7424.

(82) Wang, Z.; Tanabe, K. K.; Cohen, S. M. *Inorg. Chem.* **2009**, *48*, 296.

(83) Tanabe, K. K.; Allen, C. A.; Cohen, S. M. *Angew. Chem. Int. Ed.* **2010**, *49*, 9730.

(84) Serra-Crespo, P.; Ramos-Fernandez, E. V.; Gascon, J.; Kapteijn, F. *Chem. Mater.* **2011**, *23*, 2565.

(85) Liu, C.; Li, T.; Rosi, N. L. *J. Am. Chem. Soc.* **2012**, *134*, 18886.

(86) Kim, M. *et al. Dalton Trans.* **2012**, *41*, 6277.

(87) Cohen, S. M. *Chem. Rev.* **2012**, *112*, 970.

(88) Kim, M. *et al. J. Am. Chem. Soc.* **2012**, *134*, 18082.

(89) Kim, M. *et al. Chem. Sci.* **2012**, *3*, 126.

(90) Hong, D. H.; Suh, M. P. *Chem. Eur. J.* **2014**, *20*, 426.

(91) Jeong, S. *et al. Chem. Mater.* **2014**, *26*, 1711.

(92) Fei, H. *et al. Chem. Commun.* **2015**, *51*, 66.

(93) Férey, G. *et al. Angew. Chem. Int. Ed.* **2004**, *43*, 6296.

(94) Park, K. S. *et al. Proc. Natl. Acad. Sci. U.S.A.* **2006**, *103*, 10186.

(95) Horcajada, P. *et al. Chem. Commun.* **2007**, 2820.

(96) Cavka, J. H. *et al. J. Am. Chem. Soc.* **2008**, *130*, 13850.

(97) Biswas, S. *et al. Dalton Trans.* **2009**, 6487.

(98) Dan-Hardi, M. *et al. J. Am. Chem. Soc.* **2009**, *131*, 10857.

(99) Colombo, V. *et al. Chem. Sci.* **2011**, *2*, 1311.

(100) Fateeva, A. *et al. Angew. Chem. Int. Ed.* **2012**, *51*, 7440.

(101) Herm, Z. R. *et al. Science* **2013**, *340*, 960.

(102) Devic, T.; Serre, C. *Chem. Soc. Rev.* **2014**, *43*, 6097.

(103) Furukawa, H. *et al. J. Am. Chem. Soc.* **2014**, *136*, 4369.

(104) DeCoste, J. B. *et al. J. Mater. Chem. A* **2013**, *1*, 5642.

(105) Yuan, D.; Zhao, D.; Sun, D.; Zhou, H.-C. *Angew. Chem. Int. Ed.* **2010**, *49*, 5357.

(106) Serre, C. *et al. J. Am. Chem. Soc.* **2002**, *124*, 13519.

(107) Kang, I. J.; Khan, N. A.; Haque, E.; Jhung, S. H. *Chem. Eur. J.* **2011**, *17*, 6437.

(108) Sonnauer, A. *et al. Angew. Chem. Int. Ed.* **2009**, *48*, 3791.

(109) Long, P. *et al. Microporous Mesoporous Mater.* **2011**, *142*, 489.

(110) Szilagyi, P. A. *et al. CrystEngComm* **2013**, *15*, 10175.

(111) Liao, J.-H.; Chen, W.-T.; Tsai, C.-S.; Wang, C.-C. *CrystEngComm* **2013**, *15*, 3377.

(112) Li, J. *et al. Chem. Sci.* **2013**, *4*, 3232.

(113) Prasad, T. K.; Hong, D. H.; Suh, M. P. *Chem. Eur. J.* **2010**, *16*, 14043.

(114) Zhang, Z. *et al. J. Am. Chem. Soc.* **2012**, *134*, 924.

(115) Yao, Q. *et al. Dalton Trans.* **2012**, *41*, 3953.

(116) Denysenko, D. *et al. Chem. Commun.* **2012**, *48*, 1236.

(117) Kim, M. *et al. J. Am. Chem. Soc.* **2012**, *134*, 18082.

(118) Lalonde, M. *et al. J. Mater. Chem. A* **2013**, *1*, 5453.

(119) Brozek, C. K.; Dinca, M. *Chem. Sci.* **2012**, *3*, 2110.

(120) Kim, Y. *et al. Chem. Eur. J.* **2012**, *18*, 16642.

(121) Das, S.; Kim, H.; Kim, K. *J. Am. Chem. Soc.* **2009**, *131*, 3814.

(122) Zhang, Z.-J. *et al. Chem. Commun.* **2011**, *47*, 6425.

(123) Wei, Z.; Lu, W.; Jiang, H.-L.; Zhou, H.-C. *Inorg. Chem.* **2013**, *52*, 1164.

(124) Song, X.; Jeong, S.; Kim, D.; Lah, M. S. *CrystEngComm* **2012**, *14*, 5753.

(125) Dincă, M.; Long, J. R. *J. Am. Chem. Soc.* **2007**, *129*, 11172.

(126) Fu, H.-R.; Xu, Z.-X.; Zhang, J. *Chem. Mater.* **2015**, *27*, 205.

(127) Liu, T.-F. *et al. J. Am. Chem. Soc.* **2014**, *136*, 7813.

(128) Lammert, M. *et al. Inorg. Chem.* **2013**, *52*, 8521.

(129) Park, J.; Feng, D.; Zhou, H.-C. *J. Am. Chem. Soc.* **2015**, *137*, 1663.

(130) Shannon, R. *Acta Crystallogr. A* **1976**, *32*, 751.

(131) Hocking, R. K.; Hambley, T. W. *Dalton Trans.* **2005**, 969.

(132) Nakamura, M.; Takahashi, M. In *Mössbauer Spectroscopy*; John Wiley & Sons, Inc.: 2013, p 177.

(133) Ogilby, P. R. *Chem. Soc. Rev.* **2010**, *39*, 3181.

(134) Apel, K.; Hirt, H. *Annu. Rev. Plant. Biol.* **2004**, *55*, 373.

(135) Greer, A. *Acc. Chem. Res.* **2006**, *39*, 797.

(136) Droge, W. *Physiol. Rev.* **2002**, *82*, 47.

(137) Dolmans, D. E.; Fukumura, D.; Jain, R. K. *Nat. Rev. Cancer* **2003**, *3*, 380.

(138) Wilson, B. C.; Patterson, M. S. *Phys. Med. Biol.* **2008**, *53*, R61.

(139) Schweitzer, C.; Schmidt, R. *Chem. Rev.* **2003**, *103*, 1685.

(140) DeRosa, M. C.; Crutchley, R. J. *Coord. Chem. Rev.* **2002**, *233–234*, 351.

(141) Legrini, O.; Oliveros, E.; Braun, A. M. *Chem. Rev.* **1993**, *93*, 671.

(142) Castano, A. P.; Mroz, P.; Hamblin, M. R. *Nat. Rev. Cancer* **2006**, *6*, 535.

(143) Clennan, E. L.; Pace, A. *Tetrahedron* **2005**, *61*, 6665.

(144) Castano, A. P.; Demidova, T. N.; Hamblin, M. R. *Photodiagn. and Photodyn. Ther.* **2004**, *1*, 279.

(145) Smirnoff, N. *New Phytol.* **1993**, *125*, 27.

(146) Esser, P.; Pohlmann, B.; Scharf, H. D. *Angew. Chem. Int. Ed.* **1994**, *33*, 2009.

(147) Lovell, J. F.; Liu, T. W. B.; Chen, J.; Zheng, G. *Chem. Rev.* **2010**, *110*, 2839.

(148) Cló, E.; Snyder, J. W.; Ogilby, P. R.; Gothelf, K. V. *Chembiochem* **2007**, *8*, 475.

(149) Zheng, G. *et al. Proc. Natl. Acad. Sci. USA* **2007**, *104*, 8989.

(150) Yogo, T. *et al. Proc. Natl. Acad. Sci. USA* **2008**, *105*, 28.

(151) Jang, B.; Choi, Y. *Theranostics* **2012**, *2*, 190.

(152) Erbas-Cakmak, S.; Akkaya, E. U. *Angew. Chem. Int. Ed.* **2013**, *52*, 11364.

(153) Majumdar, P.; Nomula, R.; Zhao, J. *J. Mater. Chem. C* **2014**, *2*, 5982.

(154) Irie, M. *Chem. Rev.* **2000**, *100*, 1685.

(155) Russew, M.-M.; Hecht, S. *Adv. Mater.* **2010**, *22*, 3348.

(156) Bouas-Laurent, H.; Durr, H. *Pure Appl. Chem.* **2001**, *73*, 639.

(157) Matsuda, K.; Irie, M. *J. Photochem. Photobiol. C* **2004**, *5*, 169.

(158) Tian, H.; Yang, S. J. *Chem. Soc. Rev.* **2004**, *33*, 85.

(159) Kronemeijer, A. J. *et al. Adv. Mater.* **2008**, *20*, 1467.

(160) Zhang, J.; Zou, Q.; Tian, H. *Adv. Mater.* **2013**, *25*, 378.

(161) Hou, L. *et al. J. Am. Chem. Soc.* **2014**, *136*, 910.

(162) Wight, A. P.; Davis, M. E. *Chem. Rev.* **2002**, *102*, 3589.

(163) Mallat, T.; Baiker, A. *Chem. Rev.* **2004**, *104*, 3037.

(164) Maldotti, A.; Molinari, A.; Amadelli, R. *Chem. Rev.* **2002**, *102*, 3811.

(165) Byrne, J. A. *et al. Appl. Catal. B-environ* **1998**, *17*, 25.

(166) Fox, M. A.; Dulay, M. T. *Chem. Rev.* **1993**, *93*, 341.

(167) Heitbaum, M.; Glorius, F.; Escher, I. *Angew. Chem. Int. Ed.* **2006**, *45*, 4732.

(168) Herrmann, J. M. *Top. Catal.* **2005**, *34*, 49.

(169) Kitano, M.; Matsuoka, M.; Ueshima, M.; Anpo, M. *Appl. Catal. A* **2007**, *325*, 1.

(170) Litter, M. I. *Appl. Catal. B-environ* **1999**, *23*, 89.

(171) Moller, K.; Bein, T. *Chem. Mater.* **1998**, *10*, 2950.

(172) Thomas, J. M. *Angew. Chem. Int. Ed.* **1994**, *33*, 913.

(173) Wang, Y.; Wang, X.; Antonietti, M. *Angew. Chem. Int. Ed.* **2012**, *51*, 68.

(174) Phan, N. T. S.; Van Der Sluys, M.; Jones, C. W. *Adv. Synth. Catal.* **2006**, *348*, 609.

(175) Jin, S. *et al. J. Am. Chem. Soc.* **2013**, *135*, 955.

(176) Kent, C. A. *et al. J. Am. Chem. Soc.* **2011**, *133*, 12940.

(177) Lee, C. Y. *et al. J. Am. Chem. Soc.* **2011**, *133*, 15858.

(178) Wang, C.; Xie, Z.; deKrafft, K. E.; Lin, W. *ACS Appl. Mater. Interfaces* **2012**, *4*, 2288.

(179) Wang, J.-L.; Wang, C.; Lin, W. *ACS Catal.* **2012**, *2*, 2630.

(180) Deng, H. *et al. Science* **2010**, *327*, 846.

(181) Gao, W.-Y.; Chrzanowski, M.; Ma, S. *Chem. Soc. Rev.* **2014**, *43*, 5841.

(182) Irie, M. *Photochem. Photobiol. Sci.* **2010**, *9*, 1535.

(183) Feng, D. *et al. J. Am. Chem. Soc.* **2013**, *135*, 17105.

(184) Fukaminato, T.; Doi, T.; Tanaka, M.; Irie, M. *J. Phys. Chem. C* **2009**, *113*, 11623.

(185) Indelli, M. T. *et al. J. Am. Chem. Soc.* **2008**, *130*, 7286.

(186) Williams, D. E. *et al. J. Am. Chem. Soc.* **2014**, *136*, 11886.

(187) Dolmans, D. E. J. G. J.; Fukumura, D.; Jain, R. K. *Nat. Rev. Cancer* **2003**, *3*, 380.

(188) Castano, A. P.; Mroz, P.; Hamblin, M. R. *Nat Rev Cancer* **2006**, *6*, 535.

(189) Lucky, S. S.; Soo, K. C.; Zhang, Y. *Chem. Rev.* **2015**, *115*, 1990.

(190) Ng, K. K.; Zheng, G. *Chem. Rev.* **2015**, *115*, 11012.

(191) Majumdar, P.; Nomula, R.; Zhao, J. Z. *J. Mater. Chem. C* **2014**, *2*, 5982.

(192) In *Molecular Switches*; Wiley-VCH Verlag GmbH & Co. KGaA: 2011, p I.

(193) Kobatake, S. *et al. Nature* **2007**, *446*, 778.

(194) Szymański, W. *et al. Chem. Rev.* **2013**, *113*, 6114.

(195) Konan, Y. N.; Gurny, R.; Allémann, E. *J. Photochem. Photobiol., B* **2002**, *66*, 89.

(196) Wang, A. Z.; Langer, R.; Farokhzad, O. C. *Annu. Rev. Med.* **2012**, *63*, 185.

(197) Horcajada, P. *et al. Chem. Rev.* **2012**, *112*, 1232.

(198) Lu, K.; He, C.; Lin, W. *J. Am. Chem. Soc.* **2014**, *136*, 16712.

(199) Kent, C. A. *et al. J. Am. Chem. Soc.* **2011**, *133*, 12940.

(200) Son, H.-J. *et al. J. Am. Chem. Soc.* **2013**, *135*, 862.

(201) Dolgopolova, E. A. *et al. Angew. Chem. Int. Ed.* **2015**, *54*, 13639.

(202) Park, J.; Feng, D.; Yuan, S.; Zhou, H. C. *Angew. Chem. Int. Ed.* **2015**, *54*, 430.

(203) Tan, K. *et al. Chem. Mater.* **2012**, *24*, 3153.

(204) Ma, B.-Q.; Mulfort, K. L.; Hupp, J. T. *Inorg. Chem.* **2005**, *44*, 4912.

(205) Liu, L.; Telfer, S. G. *J. Am. Chem. Soc.* **2015**, *137*, 3901.

(206) Morris, W. *et al. J. Am. Chem. Soc.* **2014**, *136*, 7261.

(207) Cliffe, M. J. *et al. Nat. Commun.* **2014**, *5*, 4176.

(208) Wu, H. *et al. J. Am. Chem. Soc.* **2013**, *135*, 10525.

(209) Trickett, C. A. *et al. Angew. Chem. Int. Ed.* **2015**, *54*, 11162.

(210) Taylor, J. M. *et al. J. Am. Chem. Soc.* **2015**, *137*, 11498.

(211) DeCoste, J. B. *et al. New J. Chem.* **2015**, *39*, 2396.

(212) Hu, Z.; Zhao, D. *Dalton Trans.* **2015**, *44*, 19018.

(213) Schaate, A. *et al. Chem. Eur. J.* **2011**, *17*, 6643.

(214) Feng, D. *et al. J. Am. Chem. Soc.* **2014**, *136*, 17714.

(215) Juan-Alcaniz, J.; Gascon, J.; Kapteijn, F. *J. Mater. Chem* **2012**, *22*, 10102.

(216) Luo, F. *et al. Angew. Chem. Int. Ed.* **2014**, *53*, 9298.

(217) Walton, I. M. *et al. New J. Chem.* **2016**, *40*, 101.

(218) Herder, M. *et al. J. Am. Chem. Soc.* **2015**, *137*, 2738.

(219) Ferrari, M. *Nat. Rev. Cancer* **2005**, *5*, 161.

(220) Barreto, J. A. *et al. Adv. Mater.* **2011**, *23*, H18.

(221) Lammers, T. *et al. Acc. Chem. Res.* **2011**, *44*, 1029.

(222) Schroeder, A. *et al. Nat. Rev. Cancer* **2012**, *12*, 39.

(223) Davis, M. E.; Chen, Z.; Shin, D. M. *Nat. Rev. Drug Discov.* **2008**, *7*, 771.

(224) Peer, D. *et al. Nat. Nanotechnol.* **2007**, *2*, 751.

(225) Jiang, W.; Kim, B. Y. S.; Rutka, J. T.; Chan, W. C. W. *Nat. Nanotechnol.* **2008**, *3*, 145.

(226) Jin, H.; Heller, D. A.; Sharma, R.; Strano, M. S. *ACS Nano* **2009**, *3*, 149.

(227) Lu, F.; Wu, S.-H.; Hung, Y.; Mou, C.-Y. *Small* **2009**, *5*, 1408.

(228) Nel, A. E. *et al. Nat. Mater.* **2009**, *8*, 543.

(229) Sykes, E. A.; Chen, J.; Zheng, G.; Chan, W. C. W. *ACS Nano* **2014**, *8*, 5696.

(230) Zhang, S. *et al. Adv. Mater.* **2009**, *21*, 419.

(231) Albanese, A.; Tang, P. S.; Chan, W. C. W. *Annu. Rev. Biomed. Eng.* **2012**, *14*, 1.

(232) Alkilany, A. M.; Murphy, C. J. *J. Nanopart. Res.* **2010**, *12*, 2313.

(233) Sailor, M. J.; Park, J.-H. *Adv. Mater.* **2012**, *24*, 3779.

(234) Chatterjee, D. K.; Fong, L. S.; Zhang, Y. *Adv. Drug Deliver. Rev.* **2008**, *60*, 1627.

(235) Alkilany, A. M. *et al. Small* **2009**, *5*, 701.

(236) Bechet, D. *et al. Trends Biotechnol.* **2008**, *26*, 612.

(237) Furukawa, H.; Cordova, K. E.; O'Keeffe, M.; Yaghi, O. M. *Science* **2013**, *341*, 1230444.

(238) Carné-Sánchez, A.; Imaz, I.; Cano-Sarabia, M.; Maspoch, D. *Nat. Chem.* **2013**, *5*, 203.

(239) Jhung, S. H. *et al. Adv. Mater.* **2007**, *19*, 121.

(240) Tsuruoka, T. *et al. Angew. Chem. Int. Ed.* **2009**, *48*, 4739.

(241) Allendorf, M. D.; Bauer, C. A.; Bhakta, R. K.; Houk, R. J. T. *Chem. Soc. Rev.* **2009**, *38*, 1330.

(242) Horcajada, P. *et al. Nat. Mater.* **2010**, *9*, 172.

(243) Matsuda, R. *et al. Nature* **2005**, *436*, 238.

(244) Moon, H. R.; Lim, D.-W.; Suh, M. P. *Chem. Soc. Rev.* **2013**, *42*, 1807.

(245) Sindoro, M.; Yanai, N.; Jee, A.-Y.; Granick, S. *Acc. Chem. Res.* **2014**, *47*, 459.

(246) Zhang, L. *et al. Chem. Commun.* **2015**, *51*, 10831.

(247) Huan, Z. G. *et al. J. Mater. Sci.: Mater. Med.* **2010**, *21*, 2623.

(248) Patterson, J. P. *et al. J. Am. Chem. Soc.* **2015**, *137*, 7322.

(249) Thanh, N. T. K.; Maclean, N.; Mahiddine, S. *Chem. Rev.* **2014**, *114*, 7610.

(250) Zahn, G. *et al. CrystEngComm* **2014**, *16*, 9198.

(251) Low, P. S.; Kularatne, S. A. *Curr. Opin. Chem. Biol.* **2009**, *13*, 256.

(252) Xia, W.; Low, P. S. *J. Med. Chem.* **2010**, *53*, 6811.

(253) Deria, P.; Bury, W.; Hupp, J. T.; Farha, O. K. *Chem. Commun.* **2014**, *50*, 1965.

(254) Masters, J. R. *Nat. Rev. Cancer* **2002**, *2*, 315.

(255) Kim, J.; Tung, C.-H.; Choi, Y. *Chem. Commun.* **2014**, *50*, 10600.